UNIVERSITÄT BONN
Physikalisches Institut

Charm Photoproduction using Electron Taggers with the Zeus Detector at HERA

von
Gayane Aghuzumtsyan

Charm production has been studied at a centre-of-mass energy of $\sqrt{s} = 318\,\mathbf{GeV}$ in the ZEUS experiment at the electron-proton collider HERA. The data from the years 1998 - 2000 are used. Photoproduction is identified by reconstructing the $D^*(2010)$ meson via the decay chain $D^{*+} \longrightarrow K^-\pi^+\pi^+(+c.c.)$ and by selecting the scattered electron in one of the dedicated electron taggers located 44m and 35m away from the interaction point.
The total visible cross section and differential cross sections as a function of $p_T(D^*)$, $\eta(D^*)$ and W were measured in the restricted phase space: $-1.0 < \eta D(^*) < 1.5$, $p_T(D^*) > 1.5\,\mathbf{GeV}$, $80\,\mathbf{GeV} < W < 120\,\mathbf{GeV}$ and $Q^2 < 0.015\,\mathbf{GeV}^2$ in case of the 44m tagger sample, and $-1.5 < D(^*) < 1.0$, $p_T(D^*) > 2.0\,\mathbf{GeV}$, $200\,\mathbf{GeV} < W < 260\,\mathbf{GeV}$ and $Q^2 < 0.02\,\mathbf{GeV}^2$ in case of the 35m tagger sample. Next-to-leading-order QCD predictions were calculated in the same kinematic region as the data. The comparison of the theoretical predictions with the data shows good agreement within the theoretical uncertainties. Total charm cross sections were calculated by extrapolating the visible cross sections in the limited $(p_T(D^*), \eta(D^*))$ phase space to the full kinematic region. The measurements with the 35m tagger overlap with previous untagged data while the 44m tagger data are used to study a new intermediate region $80\,\mathbf{GeV} < W_{44m} < 120\,\mathbf{GeV}$ between fixed target and and the other HERA measurements. The comparison of the NLO QCD predictions with the data shows good agreement.

Post address:
Nußallee 12
53115 Bonn
Germany

BONN-IR-2006-07
Bonn University
July 2006
ISSN-0172-8741

UNIVERSITÄT BONN
Physikalisches Institut

Charm Photoproduction using Electron Taggers with the Zeus Detector at HERA

von
Gayane Aghuzumtsyan
aus
Eriwan, Armenien

Angefertigt mit Genehmigung der Mathematisch-Naturwissenschaftlichen Fakultät der Rheinischen Friedrich-Wilhelms-Universität Bonn

1. Referent:	Prof. Dr. I. C. Brock
2. Referent:	Prof. E. von Törne
Tag der Promotion:	11.07.2006

Diese Dissertation ist auf dem Hochschulschriftenserver der ULB Bonn `http://hss.ulb.uni-bonn.de/diss_online` *elektronisch publiziert.*

Erscheiningsjahr: 2006

To My Family

Contents

Introduction **3**

1 Theory **5**
1.1 The Standard Model . . . 5
1.2 Kinematics of *ep* Scattering . . . 7
1.3 DIS Cross Sections and Structure Functions . . . 10
1.4 Photoproduction . . . 12
1.4.1 Direct Photoproduction . . . 12
1.4.2 Resolved Photoproduction . . . 13
1.4.3 Photoproduction Cross Section . . . 13
1.5 Photoproduction of Heavy Quarks . . . 14
1.6 Heavy Quark Production Models . . . 15
1.6.1 Massive Quark Model . . . 17
1.6.2 Massless Quark Model . . . 17
1.7 Charm Quark Production at HERA . . . 17

2 Experimental Setup **22**
2.1 HERA Collider . . . 22
2.2 ZEUS Detector . . . 24
2.3 Central Tracking Detector . . . 27
2.4 Uranium Calorimeter . . . 28
2.5 Electron Taggers . . . 30
2.5.1 44m Tagger . . . 30
2.5.2 35m Tagger . . . 32
2.5.3 Luminosity Monitor . . . 32
2.6 Trigger and Data Acquisition . . . 32

3 Monte Carlo Simulation **35**
3.1 Overview . . . 35
3.2 Event Generators . . . 35
3.2.1 HERWIG . . . 36
3.2.2 PYTHIA . . . 37
3.3 Next-to-Leading Order Program FMNR . . . 38
3.4 ZEUS Detector Simulation and Event Reconstruction Chain . . . 40

4 Event Reconstruction and Selection **42**
4.1 Event Reconstruction . . . 42
4.1.1 Reconstruction of Kinematic Variables . . . 42
4.1.2 Electron Method for the 35m Tagger . . . 42
4.1.3 Jacquet-Blondel method for the 44m Tagger . . . 43

4.1.4 Reconstruction of the Hadronic System - ZUFOs . . . 43
4.1.5 Track Reconstruction in the CTD . . . 45
4.2 Trigger Selection . . . 47
4.2.1 First Level Trigger . . . 47
4.2.2 Second Level Trigger . . . 48
4.2.3 Third Level Trigger . . . 49
4.2.4 Tagged Charm Trigger (DST92) . . . 49
4.2.5 Luminosity Calculation for the Different Triggers . . . 50
4.3 Offline Selection . . . 50
4.3.1 Selection of photoproduction events . . . 50
4.3.2 D* Reconstruction . . . 51
4.3.3 Cuts . . . 52
4.3.4 Signal Extraction . . . 56
4.4 Acceptance of the 44m Tagger . . . 58
4.5 Acceptance of the 35m Tagger . . . 61

5 Analysis 62
5.1 Comparison of Data and Monte Carlo . . . 62
5.1.1 CTD Water Correction . . . 62
5.1.2 Comparison of Kinematic Variables and Their Resolutions . . . 63
5.1.3 Binning the data . . . 69
5.1.4 Acceptance . . . 69
5.2 Cross Sections . . . 76
5.2.1 Total Cross Sections . . . 76
5.2.2 Differential Cross Sections . . . 76
5.2.3 Total Charm Cross Sections . . . 79
5.2.4 The Photon Flux . . . 79
5.3 Systematic uncertainties . . . 81

6 Results and Discussion 86
6.1 Comparison of Data Cross Sections with MC Cross Sections . . . 86
6.2 Comparison of Data Cross Sections with NLO Calculations . . . 86
6.3 Comparison of the 44m Tagger Results with Previous Analyses . . . 91
6.4 Comparison of the 35m Tagger Results with Previous Analyses . . . 93
6.5 Comparison of 35m and 44m Tagger Analysis. . . . 95
6.6 Comparison of the Total Charm Cross Sections with the NLO Predictions . . . 96

7 Summary and Conclusions 98

A Control Plots 100

B Tables 106

C Systematics 108

List of Figures 114

List of Tables 116

References 119

Introduction

The photon is one of the oldest known elementary particles with very well known (QED) properties. However, from the Heisenberg Uncertainty Principle, the photon can split by quantum mechanical fluctuations into $q\bar{q}$ pairs. For a low virtuality (real) photon these fluctuations can live for a relatively long time, and the $q\bar{q}$ state can then further develop a complex hadronic structure which cannot be described by perturbative physics alone.

Consequently, it is necessary for our understanding of the physics of the photon, its interactions with other particles and QCD in general, that we should attempt to understand such structure as fully as we are able at current and future accelerators.

High energy collisions at the HERA ep collider between quasi-real photons (radiated from the electron beam) and the proton provide an ideal testing ground for us to probe the structure of the photon in a kinematic region not available elsewhere.

Open heavy quark production in particular offers a novel way of testing both perturbative and non-perturbative aspects of quantum chromodynamics (QCD). The large mass of the c quark provides a "hard scale" needed for the QCD predictions to be calculable.

Additionally, heavy quark production is of particular interest because this process couples directly to the gluons of the colliding particles and so gives us an additional way to increase our understanding of the gluonic structure of both the photon and the proton and in particular, to study the role played by heavy quarks.

The work described in this thesis regards the study of charm production in photoproduction processes, where a quasi-real photon from the electron interacts with the incoming proton. The experimental signature of the process being analysed is:

$$ep \longrightarrow ec\bar{c}X \longrightarrow eD^*Y$$

Charm production is identified by reconstructing a D^* meson and the kinematics are evaluated by detecting the scattered lepton. Total charm cross sections were studied before at very low hadronic centre-of-mass system energies, $1 < W < 20\,\text{GeV}$ in fixed target experiments [1] and in the high W range, $130 < W < 260\,\text{GeV}$, at HERA [2, 3]. In this analysis special detector components (taggers) are used to measure the scattered lepton.

One of these taggers allows the study in a new, intermediate kinematic region, not studied before, where W covers the range $80 < W < 120$ GeV. The other tagger allows us to measure the cross section for charm production in a region overlapping that previously measured by the H1 collaboration, $171 < W < 256\,\text{GeV}$. The cross sections in the intermediate W region and in the overlapping region are compared to next-to-leading order QCD calculations.

In Chapter 1 the theoretical concepts of the *Standard Model* needed for the measurement of the charm quark photoproduction cross sections are introduced. Chapter 2 introduces the experimental setup of the ZEUS detector. The main components of the ZEUS detector relevant for this analysis: the central tracking detector, the uranium calorimeter and the electron taggers are presented. The trigger system, the data taking and the storage system are also covered. The simulation of the physics process and the detector response are described in

Chapter 3. In this chapter the calculation of the next-to-leading order (NLO) QCD predictions is explained as well. Chapter 4 gives a detailed description of the D^* meson reconstruction method used in the analysis. In this chapter one can also find information on the tracking reconstruction and electron tagging. In addition the details of the event selection and the acceptance calculation are covered. In Chapter 5 the data and the simulation are compared in order to check the quality of the modelling of both the physics process and the detector (Monte Carlo). The procedure of evaluating the photoproduction cross section from the electroproduction cross section is given and the systematic errors are discussed. Chapter 6 presents the results of this analysis including the total and differential cross sections and their comparison to the leading-order Monte Carlo cross sections and the NLO QCD calculations. The cross sections are also compared with the previous results from HERA. The summary of this analysis is presented in the last Chapter.

Chapter 1

Theory

1.1 The Standard Model

The goal of elementary particle physics is to identify the fundamental building blocks of nature, the interactions between them, and to provide a simple description of their dynamics. Many particles have been discovered, each of them having its own characteristics. The *Standard Model* (SM) [4] of particle physics is a theory, developed between the 1960s and 1970s by physicists which presents our current understanding of particle physics. It is a quantum field theory, which describes the strong, weak and electromagnetic fundamental forces, and the fundamental particles that make up all matter. According to the SM there are two kinds of elementary particles: fermions which have spin $\frac{1}{2}\hbar$ and obey the Pauli exclusion principle[1]; and bosons which have spin 0 or $1\hbar$, where $\hbar$ is the Planck constant $\hbar = h/2\pi = 1.05{\cdot}10^{-34}$ J s. The physics world in the SM is constructed from three generations of leptons and three generations of quarks, as shown in Table 1.1. The *charm* (c), *beauty* (b) and *top* (t) quarks are categorised as *heavy flavour quarks* whereas the *up* (u), *down* (d) and *strange* (s) quarks belong to the category of *light flavour quarks*. Each elementary particle has an antiparticle partner with the same mass, but oppositely signed quantum numbers.

	Quarks			Leptons		
		Mass	El. charge (e)		Mass	El. charge (e)
1	up (u) down (d)	$\sim$ 4 MeV $\sim$ 7 MeV	+2/3 −1/3	electron (e) electron neutrino (ν_e)	0.51 MeV $<$ 3 eV	-1 0
2	charm (c) strange (s)	$\sim$ 1.2 GeV $\sim$ 150 MeV	+2/3 −1/3	muon (μ) muon neutrino (ν_μ)	105.7 MeV $<$ 0.19 MeV	-1 0
3	top (t) bottom (b)	$\sim$ 175 GeV $\sim$ 4 GeV	+2/3 −1/3	tau (τ) tau neutrino (ν_τ)	1777 MeV $<$ 18.2 MeV	-1 0

Table 1.1: The three generations of quarks and leptons.

The fermions interact by the exchange of field quanta (bosons) which determine the properties of the interaction. The three fundamental interactions (forces) needed within the SM

[1]The Pauli exclusion principle states that no fermions can simultaneously share the same quantum state.

to explain the experimental results are listed in Table 1.2. The gravitational force is currently not incorporated in the SM. The theory of the electroweak interaction and the theory of strong interaction - quantum chromodynamics (QCD) - are both gauge theories, which means that they model the forces between fermions by coupling them to bosons which mediate the forces. The Lagrangian of each set of mediating bosons (*gauge boson*) is invariant under a transformation called a gauge transformation. These transformations can be exactly described using a unitary group called a "gauge group". The bosons in the SM are photons, which mediate the electromagnetic interaction, W and Z bosons, which mediate the weak force, and eight species of gluons, which mediate the strong force. There are also the Higgs bosons, which have not yet been observed experimentally and which induce spontaneous symmetry breaking of the gauge groups and are responsible for the existence of inertial mass.

The description of the strong interaction is based on the gauge group $SU(3)$. The gauge group of the weak and electromagnetic interactions is the $SU(2)$ group of weak isospin and $U(1)$ group of weak hypercharge. The Standard Model is often referred to us as $SU(3)_C \mathrm{x} SU(2)_L \mathrm{x} U(1)_Y$ [5, 6].

The predictions of the Standard Model for particle interactions can be expressed as a power series expansions in the coupling constants α_i, if $\alpha_i \ll 1$. A graphical representation of this perturbative calculation approach is given by *Feynmann diagrams* where the interacting, intermediate and produced particles are represented by lines. Each order of a coupling constant from the expansion is represented by a corresponding vertex.

Interaction	Theory	Boson	Charge (e)	Mass	Typical coupling strength [2]	Related group
Strong	Quantum Chromo-dynamics (QCD)	gluons g_i (i= 1...8)	0	0	~ 1	$SU(3)_C$
Weak	Electroweak	$W^{\pm}$	± 1	80.4 GeV	$\sim 10^{-6}$	$SU(2)_L$ x $U(1)_Y$
		Z	0	91.2 GeV		
Electromagnetic	Electroweak	γ	0	0	$\sim 10^{-2}$	$SU(2)_L$ x $U(1)_Y$

Table 1.2: The fundamental forces in the Standard Model.

Quarks are bound together into hadrons (groups of quarks) by the strong interaction and can not be observed as free particles as the force increases linearly with the distance between the quarks. This property of QCD is called *confinement*. Due to this property quarks form colourless hadrons which can be either *mesons* consisting of quark-antiquark pairs or *baryons* consisting of three quarks. Another property of QCD is *asymptotic freedom*, which states, that the interaction strength between two coloured objects decreases the shorter the distance between them or the higher the energy of their interaction.

Since quarks are not free particles, they can only be observed using scattering techniques. Such methods have been successfully used since 1909[3], and allow information about the internal structure of matter to be obtained. The idea of quarks was first introduced by Murray Gell-Mann [7] and George Zweig [8, 9] in 1964. They suggested that mesons and baryons are composites of quarks or antiquarks, called up, down or strange (u, d, s) with spin $\frac{1}{2}\hbar$ and electric charges 2/3e, -1/3e, -1/3e, respectively. Since quarks were not then observed, they were treated more as a mathematical explanation of the flavour pattern of particle masses

[2] Coupling is given at an energy scale of 1 GeV.

[3] A famous scattering experiment of alpha particles off gold nuclei performed by Ernest Rutherford

than as a postulate of actual physical objects. Later in 1968-1969, at the Stanford Linear Accelerator, in an experiment where electrons were scattering off protons, evidence of small hard cores, partons, inside the protons was found. Later partons were identified with the quarks. Up to now the scattering techniques have bee used successfully to obtain more information about the structure of the fundamental interaction and particles that make up matter. The ZEUS experiment is an *ep* scattering experiment at the HERA collider in DESY which has a high enough energy to achieve a resolution of $5 \cdot 10^{-19}$m.

1.2 Kinematics of *ep* Scattering

The process of electron-proton scattering can be described by the following diagram, Fig. 1.1:

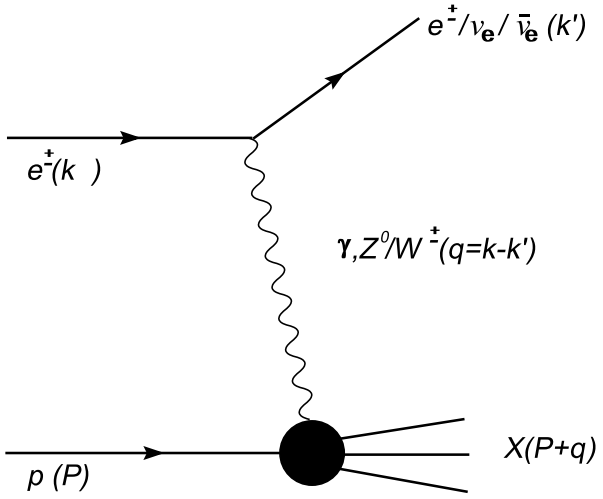

Figure 1.1: Schematic diagram of electron-proton scattering. The four vectors of the particles, or particle system, are given in parentheses.

The scattering process of a lepton ($e^{\pm}$) and a proton (p) proceeds via the exchange of an electroweak boson. In the *charged current* case (CC), a $W^{\pm}$ boson is exchanged and the incoming lepton is changed to a neutrino. In the case of *neutral current* (NC), the exchanged boson is a photon, γ, or a neutral Z boson. According to the Fig. 1.1 and assuming the proton is moving in the $+z$ direction and the charged lepton is moving in the $-z$ direction, the four-vectors of the initial and final states are given by

$$k = (E_{e^{\pm}}, \vec{k}) = (E_{e^{\pm}}, 0, 0, -p_{e^{\pm}}), \qquad P = (E_p, \vec{P}) = (E_p, 0, 0, p_p),$$
$$k' = (E'_{e^{\pm}}, \vec{k'}) = (E'_{e^{\pm}}, p'_e sin\theta_e, 0, p'_e cos\theta_e), \qquad P' = (E_X, \vec{P'}),$$

where $E_{e^{\pm}}$, $\vec{k}$ and E_p, $\vec{P}$ are the energy and momentum of the incoming lepton and proton respectively, and $E', \vec{k'}$ and $E_X, \vec{P'}$ are the energy and momentum of the outgoing lepton (or neutrino) and hadronic system respectively. The four vector of the exchanged boson is defined by $q = k - k'$. Since q is space-like, $q^2 < 0$, for convenience one defines the negative value of the exchanged boson virtuality by

$$q^2 = (k - k')^2 = -Q^2 \tag{1.1}$$

This variable, according to Heisenberg's uncertainty relation defines the transverse size in the proton $\Delta X \approx \hbar c/\sqrt{Q^2}$ which can be resolved by the boson. Events with $Q^2 \gg 1\,\mathrm{GeV}^2$ are

probing the structure of the proton. Such processes are called "deep inelastic scattering" (DIS). Processes with $Q^2 \ll 1\,\mathrm{GeV}^2$ are called "photoproduction" (PHP), since the low virtuality photon is longlived and so the interaction can be considered as an interaction with an "initial state" photon.

The square of the energy in the centre-of-mass (CMS) system of ep scattering is defined as

$$s = (k + P)^2 \approx 4E_e E_p, \tag{1.2}$$

where e denotes either an electron or a positron[4], and masses of the colliding particles are neglected. With the beam energies of the incoming electron of 27.5 GeV and proton of 920 GeV [5], the CMS energy at HERA is $\sqrt{s} = 318\,\mathrm{GeV}$. The kinematics of ep scattering can be described by the following Lorentz invariant variables:

$$W^2 = (q + P)^2, \tag{1.3}$$

$$x = \frac{Q^2}{2P \cdot q}, \tag{1.4}$$

$$y = \frac{q \cdot P}{k \cdot P}, \tag{1.5}$$

where the variable W^2 is the centre-of-mass energy of the boson-nucleon system. y is a measure of the fraction of the energy transfered from the electron to the interaction and is called the inelasticity; by definition $0 \leq y \leq 1$. In the naive quark parton model (QPM) [10] the variable x is the fraction of the proton momentum carried by the struck massless quark. The *Bjorken scaling variable* x, y and the virtuality of the exchanged boson, Q^2, are related to the square of the centre-of-mass energy, s, and W by the following equations[6]:

$$Q^2 = (s - m_p^2)xy \approx sxy. \tag{1.6}$$

$$W^2 = (s - m_p^2)y - Q^2 + m_p^2 \approx sy - Q^2 = Q^2\left(\frac{1}{x} - 1\right) + m_p^2, \tag{1.7}$$

where the indicated approximations means neglecting the mass of the proton, m_p.

As one can be seen from Eq. 1.6, the maximum possible Q^2 is s, The minimum kinematically allowed Q^2 depends on y and is given by

$$Q^2_{min} = \frac{m_e^2 y^2}{1 - y} = \mathcal{O}(10^{-12}\,\mathrm{GeV}^2). \tag{1.8}$$

In the process, where, $Q^2 \ll 1\,\mathrm{GeV}^2$, the photon is called "quasi-real". Such processes are called photoproduction, which is the subject of study in this thesis. In this case only the first term, sy, in Equation 1.7 is relevant:

$$W = \sqrt{sy}. \tag{1.9}$$

Due to the fact that the kinematic variables described above are not independent, once the centre-of-mass energy, $\sqrt{s}$, is given, it is enough to know just two variables to describe the event kinematics.

In Fig 1.2 the x, Q^2 kinematic region covered by the HERA experiments, ZEUS and H1, and other fixed target DIS experiments is shown. As can be seen from the plot, in the region corresponding to $y \leq 0.005$ at HERA, fixed target experiment measurements are dominant, whereas above this value the results from HERA dominate.

[4] In future, "electron" will be used to refer to either electron or positron.

[5] Since 1998, the energy of the protons is 920 GeV, before that it was 820 GeV.

[6] The electron mass is neglected in all equations.

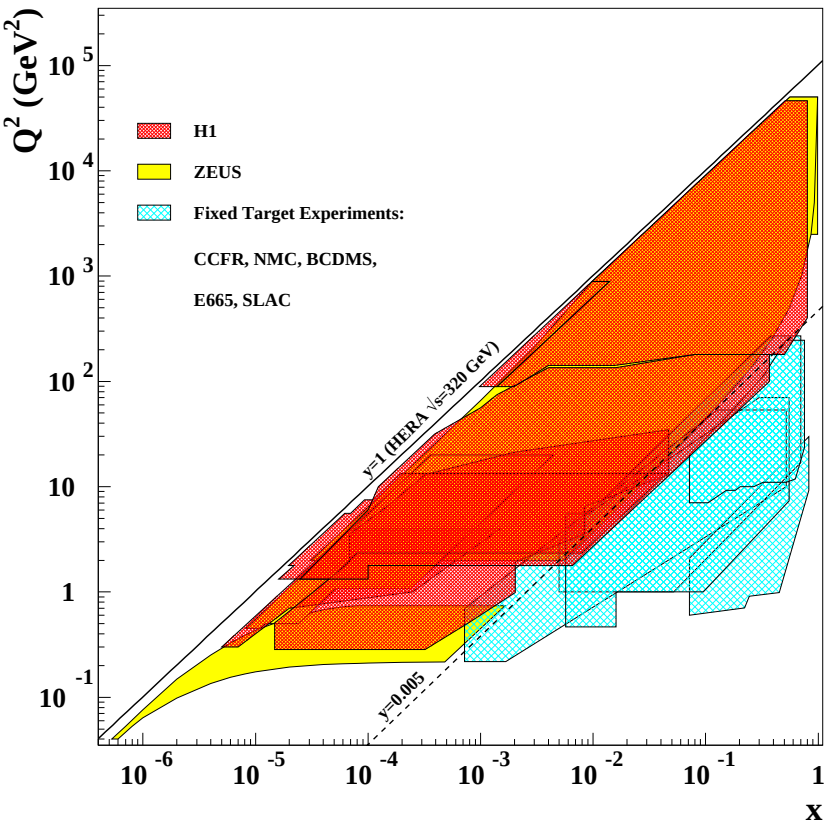

Figure 1.2: Kinematic (x, Q^2) region at HERA (H1, ZEUS) compared to fixed target experiment [11].

1.3 DIS Cross Sections and Structure Functions

The DIS cross section can be written as the product of a leptonic tensor $L_{\mu\nu}$ and a hadronic tensor $W^{\mu\nu}$ [6],

$$\frac{d^2\sigma}{dxdy} \propto L_{\mu\nu}W^{\mu\nu} \tag{1.10}$$

The leptonic vertex knows nothing about the hadronic interaction and for photon exchange can be completely calculated by *quantum electrodynamics* (QED) which gives,

$$L_{\mu\nu} = 4e^2(k_\mu k'_\nu + k_\nu k'_\mu - g_{\mu\nu}k \cdot k'). \tag{1.11}$$

The hadronic tensor depends on the structure of the proton. The most general form for it is

$$W^{\mu\nu} = W_1\left(-g_{\mu\nu} + \frac{q^\mu q^\nu}{q^2}\right) + W_2\frac{1}{M^2}\left(p_\mu - \frac{p\cdot q}{q^2}q^\mu\right)\left(p_\nu - \frac{p\cdot q}{q^2}q^\nu\right), \tag{1.12}$$

where $W_{1,2}(\nu, Q^2)$ are dimensionless functions of the Lorentz scalar variables, which can be constructed from the four-momenta at the hadronic vertex. For $W_{1,2}(\nu, Q^2)$ ν is the fraction of the energy given to the proton in its own rest frame and is defined as

$$\nu = \frac{p\cdot q}{M} \tag{1.13}$$

Thus, all information about the structure of the proton is contained in the functions W_1 and W_2. It is common to redefine these functions as

$$F_1(x, Q^2) = W_1(x, Q^2), \tag{1.14}$$

$$F_2(x, Q^2) = \nu W_2(x, Q^2). \tag{1.15}$$

In the *quark parton model* (QPM), the structure functions are related to the parton density functions (PDF), $f_q(x, Q^2)$, which describe the probability at a scale Q to find a parton, q with a fractional momentum x inside a proton. If the parton q has electric charge e_q then these are related by

$$F_2(x, Q^2) = \sum_i e_q^2 x f_q(x), \tag{1.16}$$

and

$$2xF_1(x, Q^2) = F_2(x, Q^2), \tag{1.17}$$

where the $F_{1,2}$ in the naïve QPM depend only on the scaling variable x and not on the momentum transfer Q^2 and is refered to as scaling. The differential cross section in terms of these structure functions is,

$$\frac{d^2\sigma}{dxdQ^2} = \frac{4\pi\alpha^2}{xQ^4}\left[(1-y)F_2(x) + \frac{1}{2}y^2 2xF_1(x)\right], \tag{1.18}$$

where α denotes the fine structure constant, $\alpha = \alpha_{em} = \frac{1}{137}$. The Q^2 dependence comes from the exchanged boson within the hard interaction.

At higher four-momentum transfer, it is seen that the cross section deviates from predictions, which assume scaling. To understand how this occurs the QPM needs to be modified to include the predictions of QCD. It is convenient to use used in Eq. 1.18 the *longitudinal* structure function for scattering via longitudinally polarised photons (Z bosons),

$$F_L = F_2 - 2xF_1, \tag{1.19}$$

and which is zero in the QPM.

Another structure function [12], $F_3(x,Q^2)$ is introduced to include the effect of parity violation in the exchange of an electroweak boson. Thus, the neutral current DIS cross sections can be written as

$$\frac{d^2\sigma_{NC}(e^{\pm})}{dxdQ^2} = \frac{4\pi\alpha^2}{xQ^4}\left[\left((1-y)+\frac{y^2}{2}\right)F_2(x,Q^2) - \frac{y^2}{2}F_L(x,Q^2) \mp \left(y-\frac{y^2}{2}\right)xF_3(x,Q^2)\right]. \quad (1.20)$$

Similar to the NC cross section the differential cross section for charge current scattering can be written in terms of the CC structure functions F_2^{CC}, F_L^{CC} and F_3^{CC}:

$$\frac{d^2\sigma_{CC}(e^{\pm})}{dxdQ^2} = \frac{G_F^2}{4\pi x}\left(\frac{M_W^2}{Q^2+M_W^2}\right)^2\left[Y_+(y)F_2^{CC}(x,Q^2) - y^2F_L^{CC}(x,Q^2) \mp Y_-(y)xF_3^{CC}(x,Q^2)\right], \quad (1.21)$$

where G_F is the Fermi constant and can be expressed as

$$G_F = \frac{\pi\alpha}{\sqrt{2}\sin^2\theta_W M_W^2} \quad (1.22)$$

and $Y_{\pm}(y)$ are defined by

$$Y_{\pm}(y) = 1 \pm (1-y)^2. \quad (1.23)$$

In Fig. 1.3 the differential NC and CC cross sections measured by ZEUS and H1 collaborations [13] as a function of Q^2 for $e^{\pm}p$ scattering are shown. The results are compared to the Standard Model expectations. As can be seen the CC cross section is suppressed with respect to the NC cross section until Q^2 reaches the value of the vector boson masses squared ($\approx 10^4\,\mathrm{GeV}^2$), as expected from electroweak unification.

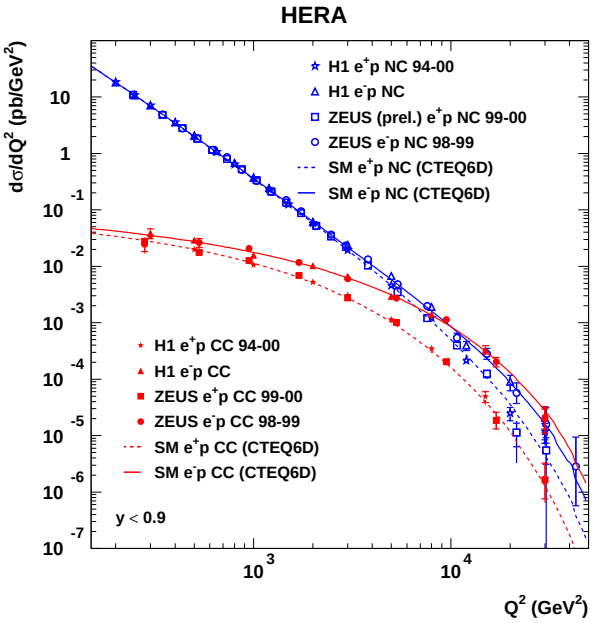

Figure 1.3: The differential NC and CC cross sections measured by ZEUS and H1 collaborations as a function of Q^2 for e^+p and e^-p scatterings.

1.4 Photoproduction

As was mentioned above, in Sec. 1.2, the variable Q^2 is used to distinguish between two kinematic regimes, Deep Inelastic Scattering (DIS) and Photoproduction (PHP). In the DIS regime the momentum transferred at the leptonic vertex, Q^2, is much larger than the proton mass. In the photoproduction regime Q^2 is small ($Q^2 \sim 0$) so the exchanged particle is an almost real photon. In this regime the electron beam can be considered as a source of approximately massless, collinear photons, so that we have a γp collider.

For $Q^2 > 0$, photons may have both transverse and longitudinal polarisation so that $\sigma_{tot}^{\gamma p} = \sigma_T + \sigma_L$. But, in the PHP regime, in the $Q^2 \longrightarrow 0$ limit, the photons can be only transversely polarised, so σ_L must vanish. In this case we can factorise the total ep cross section as:

$$\sigma^{e-p} = f^{\gamma,e} \times \sigma^{\gamma-p}, \tag{1.24}$$

where the electro-production cross section is connected with the photoproduction cross section through the factor $f^{\gamma,e}$, which is called the *photon flux*. This is discussed in more detail in Sec. 5.2.4.

In the case where the transverse energy of the final state is small, the cross section is not perturbatively calculable; this is known as "soft" photoproduction. However, when the partons in the final state have a large transverse energy, it is called "hard" phtotproduction, and the cross section is calculable perturbatively.

Hard photoproduction processes can be roughly split into two categories depending on how the photon interacts with the proton. The photon can either couple directly to a parton in the proton or fluctuate into partons before the interaction. The first process is called "direct" and the second "resolved" photoproduction.

1.4.1 Direct Photoproduction

In direct photoproduction the incoming photon interacts as a point-like object. In this case the whole energy of the photon participates in the hard subprocess. In Fig. 1.4 the dominant processes of direct hard photoproduction at HERA are shown, where the outgoing partons have large transverse energy, E_T. The left diagram is called Boson-Gluon Fusion (BGF),

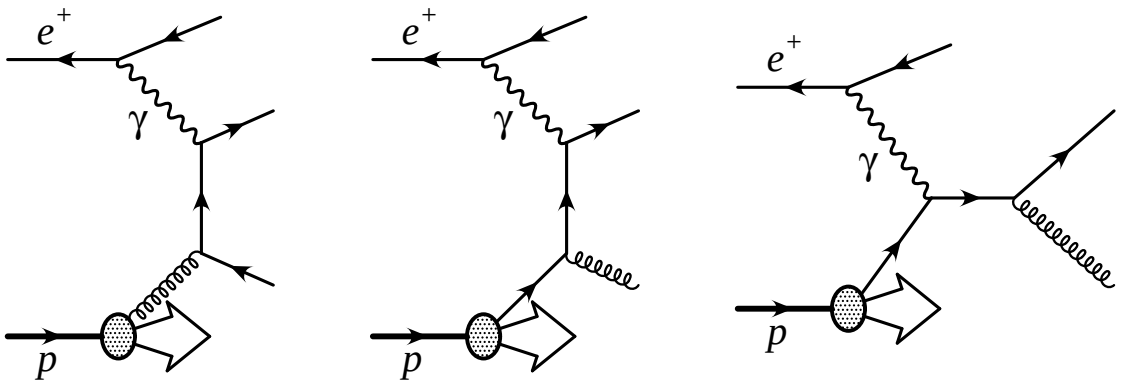

Figure 1.4: Leading order direct photoproduction; left, boson gluon fusion; middle, initial state radiation; right, QCD Compton scattering.

when a photon couples to a quark-antiquark pair, which also couples to a gluon radiated from the proton. The middle diagram is Initial State Radiation (ISR), when photon couples to a quark-antiquark pair, which couples to a parton from the proton. The right diagram is the QCD Compton process, when a photon couples to a quark from the proton. In all cases the

final state of the hard subprocess consist of two partons. Quarks and gluons fragment into jets of colourless hadrons. In the QCD Compton and ISR cases one jet is initiated by a quark and the other one by a gluon. In the BGF case both jets are initiated by quarks.

1.4.2 Resolved Photoproduction

In resolved photoproduction, because of the long lifetime of the photon, it can fluctuate into a hadronic state and act as a source of partons. In this case, one parton from the photon, which carries some fraction x_γ of the photon momentum, interacts with a parton from the proton in the hard subprocess. In this way, it is similar to hadron-hadron processes. Depending on the relative transverse momentum between the partons, the photon state can be a bound state (as in the Vector Dominance Model), *hadronic component*, or a perturbatively calculated state, *anomalous component*. In Fig. 1.5 a small selection of the resolved photoproduction processes are shown. For example, the left process shows gluon-gluon fusion. In this case both jets are quarks, while for the cases from the middle and right diagrams one is a quark jet and the other is a gluon jet. In resolved PHP processes the remaining partons from the photon give rise to a

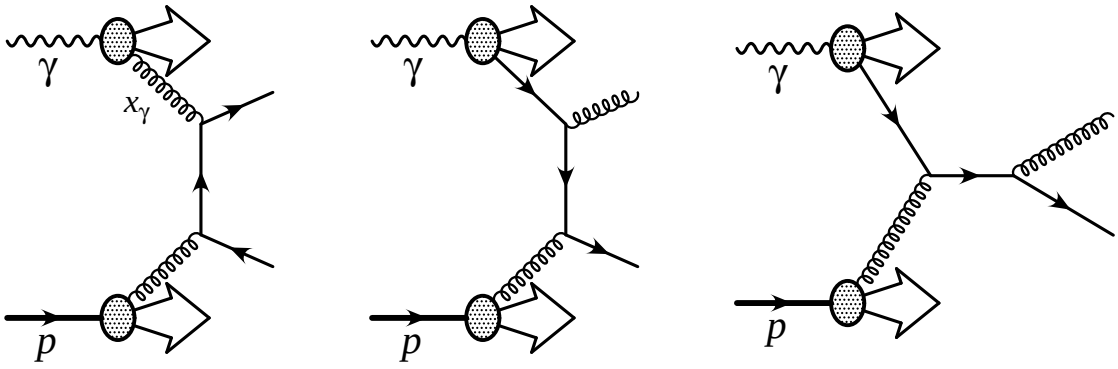

Figure 1.5: Leading order resolved photoproduction.

photon remnant. Such processes are sensitive to the parton densities in both the proton and the photon. The concept of parton densities within the photon is defined by a factorisation scale [7], μ_γ.

1.4.3 Photoproduction Cross Section

The total photoproduction cross section calculation in general consists of two parts, a perturbatively calculable (direct/point-like component) part, and a part with non-perturbatively calculable parton distribution functions with factorisation scales μ_p and μ_γ (resolved/hadronic component) [7], see Fig. 1.6,

$$d\sigma_{\gamma p\to cd} = d\sigma^{dir}_{\gamma p\to cd} + d\sigma^{res}_{\gamma p\to cd}, \tag{1.25}$$

with the direct component

$$d\sigma^{dir}_{\gamma p\to cd} = \sum_b \int_{x_p} dx_p f_{p\to b}(x_p,\mu_p^2) d\hat{\sigma}_{\gamma b\to cd} \tag{1.26}$$

[7] Boundary between direct and resolved PHP

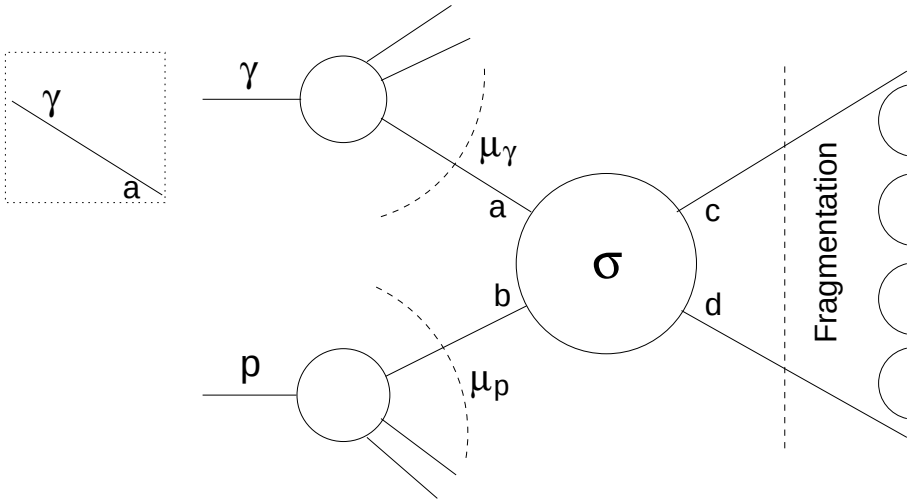

Figure 1.6: General sketch of a resolved PHP process. σ indicates the hard subprocess.μ_p and μ_γ denote the arbitrarily chosen factorisation scales. In direct PHP the photon enters the hard subprocess directly, the incoming photon is identical to a parton a, $a = \gamma$, as shown in the left top corner.

and the resolved component

$$d\sigma^{res}_{\gamma p \to cd} = \sum_{ab} \int_{x_p} dx_p \int_{x_\gamma} dx_\gamma f_{p\to b}(x_p, \mu_p^2) f_{\gamma\to a}(x_\gamma, \mu_\gamma^2) d\hat{\sigma}_{ab\to cd} \tag{1.27}$$

where the subprocess cross section, $d\hat{\sigma}$, is given by the perturbative matrix elements of the hard subprocess and the observed cross section is obtained by the convolution of the short distance subprocess cross sections with the long distance parton density functions $f_{p\to b}$ and $f_{\gamma\to a}$ [14].

The point-like and hadronic components of the photoproduction cross sections are correlated, and only their sum has a physical meaning. The distinction between direct and resolved processes is also only meaningful in leading order. For example, in Fig. 1.7 a PHP process can be seen either as a NLO direct ($\mu_\gamma < \mu_1$) or a LO resolved ($\mu_\gamma > \mu_1$) process. The ambiguity between next-to-leading (NLO) direct and leading order (LO) resolved depends on the choice of factorisation scale μ_γ. In next-to leading (NLO) QCD only the sum of the direct and resolved PHP processes is unambiguously defined.

Since the photon parton densities are soft, the contribution from the hadronic component becomes important for large centre-of-mass energy and small masses of the produced particles. For example, in heavy quark production, this can affect charm production more than beauty production.

1.5 Photoproduction of Heavy Quarks

Photoproduction processes where the virtuality of the photon $Q^2 < m_p^2$ are the dominant contribution to the HERA heavy quark production cross sections, Heavy quark production offers the possibility to probe the gluon distribution in the proton and photon either indirectly,

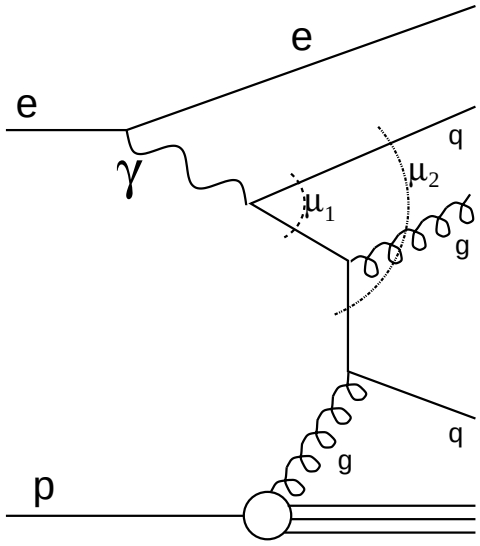

Figure 1.7: This photoproduction process can be seen as direct or as resolved photoproduction, depending on the choice of μ. The process with $\mu = \mu_1$ is accounted as NLO direct photoproduction and the process with $\mu = \mu_2$ as LO resolved photoproduction process.

by measuring the total photoproduction cross section and differential distributions, or directly, by explicit reconstruction of x_g, the momentum fraction of the proton carried by the gluon, see Eq. 1.27.

For perturbative QCD (pQCD) calculations to be valid a hard scale is needed. The scale at which the coupling strength of the strong interaction, α_s, gets too large in order to apply perturbative calculation techniques, Λ_{QCD}, is of order 200 MeV [15]. The mass of the heavy quarks are quite large compared to the Λ_{QCD}, for instance the mass of the charm quark ensures the presence of a hard scale. Therefore, photoproduction of heavy quarks is also a good testing ground for pQCD.

Heavy quark production was extensively studied in fixed target experiments [16–18] at a centre-of-mass energy of ~ 30 GeV. HERA with a centre-of-mass energy ~ 300 GeV opens a new kinematic region, where both beauty and charm production can be observed. In Fig. 1.8 the total charm cross-section in fixed target and HERA experiments is shown as a function of the centre-of-mass energy [2, 19]. The data are compared with the theoretical predictions for three different choices of the parametrisation of the photon parton densities. Each pair of the curves represents the change in the theoretical predictions due to the variations of the renormalisation and factorisation scales, which set the energy scale of the process. A single choice of the input parameters allows a good description of the data in the whole energy range considered: mass of the charm quark $m_c = 1.5\,\text{GeV}$, MRSG [20] for the proton and GRV-HO [23] for the photon parton densities.

1.6 Heavy Quark Production Models

Two types of NLO calculation have been developed for comparison with the measurements of heavy quark photoproduction at HERA, the "massive" charm approach [24, 25] and the "massless" charm approach [26–28]. S. Frixione et al. have developed a program that inte-

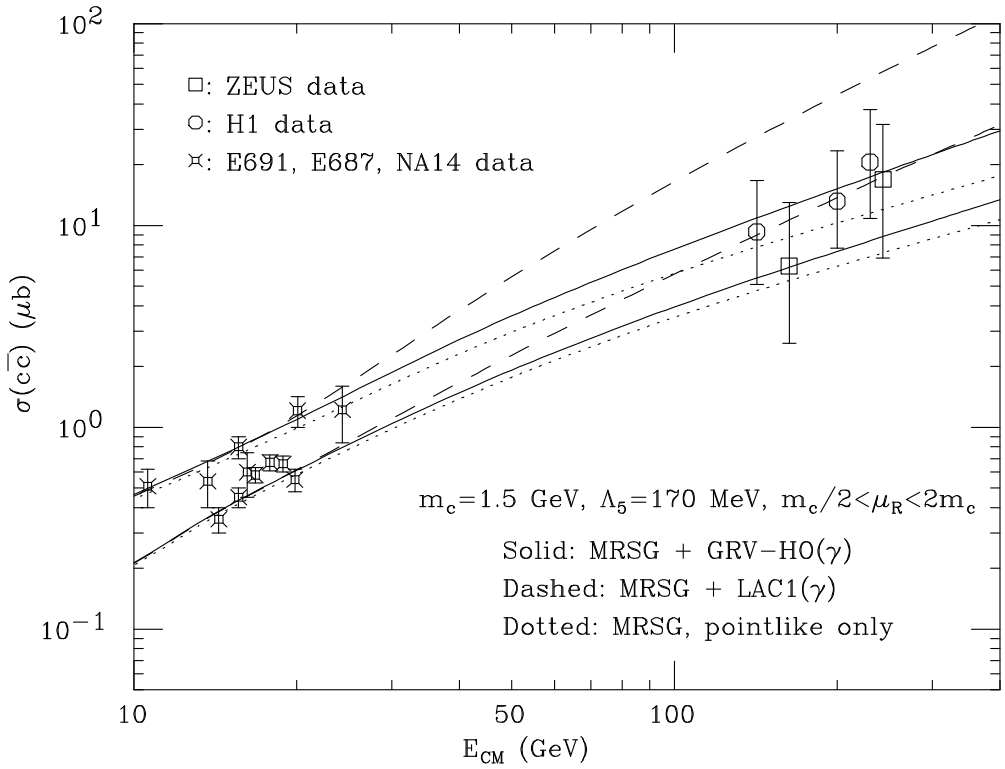

Figure 1.8: Total cross section for photoproduction of $c\bar{c}$ pairs as a function of the γp centre-of-mass energy. The comparison between the next-to-leading order QCD predictions and experimental results is shown. MRSG[20] is the proton and GRV-HO[21] and LAC1[22] is the photon parton densities. Λ_5 is the Λ_{QCD} of the process, μ_R is the renormalisation scale.

grates the NLO formulae and produces cross sections which can be compared with data (see Sec. 3.3).

1.6.1 Massive Quark Model

The *massive* model is based on the next-to-leading order QCD calculations of order α_s^2 in the coefficient functions in the so-called fixed-flavour number scheme (FFNS). In this scheme the number of active quark flavours is fixed, independent of Q^2. Only the three light quarks (u, d, s) and gluons contribute to the photon and proton structure function. In this case charm quarks are produced dynamically in the hard subprocess and do not contribute to the evolution of the running coupling constant or of the structure function. Therefore subprocesses initiated by an intrinsic heavy flavour generated by the structure function (so-called *excitation processes*) are not present and only two leading order resolved processes are possible:

$$gg \longrightarrow cc \quad and \quad q\bar{q} \longrightarrow c\bar{c} \tag{1.28}$$

The massive calculations for photoproduction of heavy quarks are based on hadroproduction [29, 30]. The presence of two large scales, Q^2 and m_c^2, makes this scheme unreliable in the region $Q^2, p_T^2 \gg m_c^2$, where p_T is the transverse momentum of charm quark, because the neglected terms of orders higher than α_s^2 contain $\log(p_T^2/m_c^2)$ factors that become large and spoil the convergence of the perturbation series. The massive scheme is therefore reliable in the region $p_T^2 \lesssim m_c^2$.

1.6.2 Massless Quark Model

In the *massless* charm production model the heavy quarks contribute to the parton density function. Above a certain threshold charm is treated as an additional active flavour with zero mass. Below this threshold the heavy quarks revert to inactive flavours, and the light quarks and gluons are the only active partons, as in massive scheme. This scheme is also called the zero-mass variable-flavour number scheme (ZM-VFNS). Because of that, in addition to the processes $gg \longrightarrow cc, q\bar{q} \longrightarrow c\bar{c}$, additional charm-excitation leading order processes are present in this scheme:

$$qc \longrightarrow qc \quad and \quad gc \longrightarrow gc. \tag{1.29}$$

The massless scheme allows the re-summation of the terms $\log(p_T^2/m_c^2)$ in the perturbative fragmentation function (PFF) for a heavy quark. This fragmentation function approach is based on the assumption that the heavy quarks act as if they were massless when their momenta are much larger than their mass. The PFF also includes the logarithmic terms, so that their re-summation is possible. Nevertheless the massless method is not reliable at $p_T^2 \sim m_c^2$ [31] and can only be expected to produce reasonable predictions for $p_T^2 \gg m_c^2$.

A comparison of the two methods can be found in [32]. Fig. 1.9 shows that both methods give different results for the direct and resolved components. But for the sum of direct and resolved, the physical observable, they are in better agreement.

The cross sections obtained in this analysis will be compared with a massive calculation.

1.7 Charm Quark Production at HERA

At HERA, with the centre-of-mass energy of $\sim 300\,\text{GeV}$, the study of heavy quarks is a subject of great interest. At this energy the $c\bar{c}$ production cross section is of the order of $1\mu b$, while the beauty cross section is $\mathcal{O}$ 10 nb. There is a large statistics sample available at HERA for

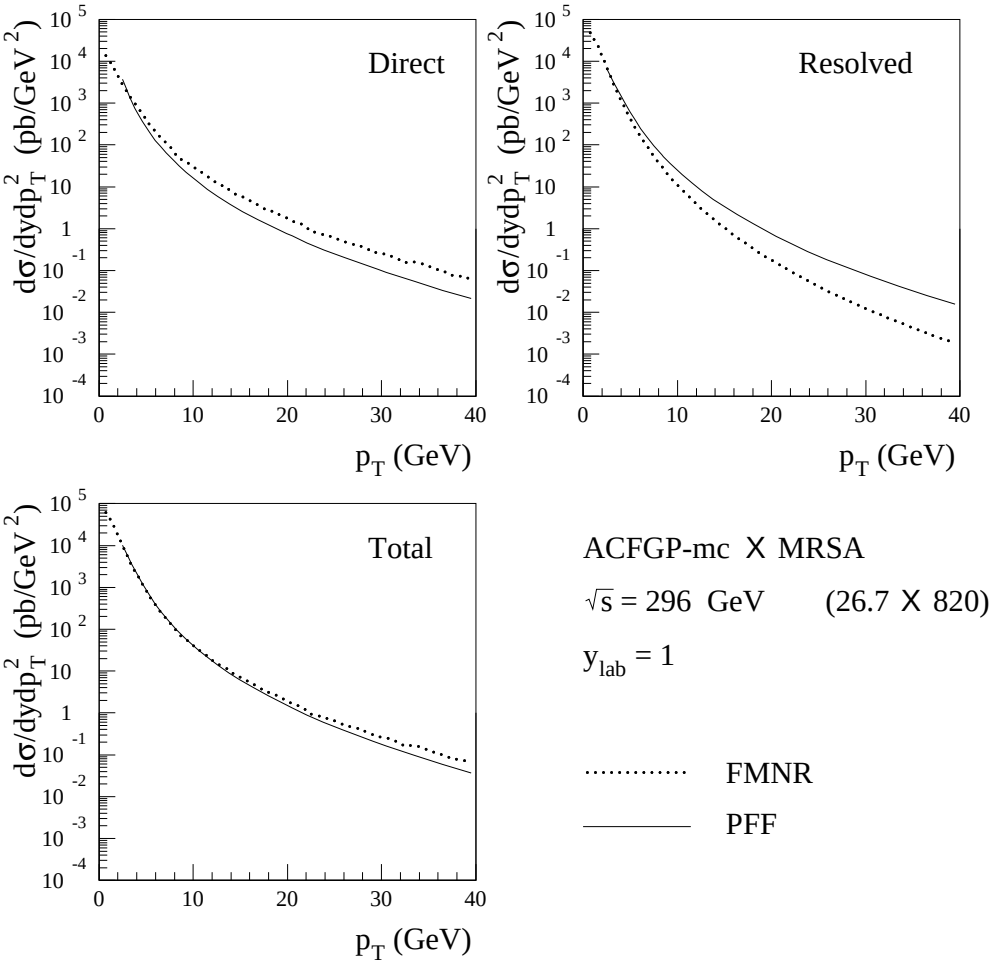

Figure 1.9: Comparison of massive (FMNR) and massless (PFF) calculations[31]. The total cross section $d\sigma_{\gamma p \to eX}/dydp_T^2$ is plotted as a function of the transverse momentum of the charm quark at rapidity $y_{lab} = 1$. The upper plots show comparisons between the massless and massive calculations for direct (upper left plot) and resolved (upper right plot) processes.Here a disagreement can be seen. The sum of direct and resolved processes for massive and massless calculation is compared in the lower plot. The agreement is better here than that for each component separately.

analysing charm events. Previous results of open charm production, that proceeds via the search for D^* mesons, are discussed here.

One of the most interesting for the analysis in this thesis is the analysis made by the H1 Collaboration [3], in which charm was tagged by identifying $D^{*\pm}(2010)$ mesons in the final state via their charged decay products:

$$D^{*+} \longrightarrow D^0\pi_s^+ \longrightarrow (K^-\pi^+)\pi_s^+ \tag{1.30}$$

and the charge conjugated (c.c.) processes. The analysis is carried out independently for the case where the positron is detected in the electron tagger ("tagged" case) and for the case where it is not required to be seen ("untagged" case). The tagged photoproduction analysis is restricted to the kinematical range $0.028 < y = 1 - E_{e'}/E_e < 0.65$, consequently with the γp centre-of-mass energy in the range of $159 < W_{\gamma p} < 242\,\text{GeV}$, with a mean of $W_{\gamma p} \approx 200\,\text{GeV}$, and $Q^2 < 10^{-2}\,\text{GeV}^2$. The acceptance of the electron tagger is above 20%. The untagged sample covers the kinematical region $0.1 < y < 0.8$, consequently with $95 < W < 268\,\text{GeV}$ with a mean of $W \approx 180\,\text{GeV}$, and $Q^2 < 4\,\text{GeV}$. The visible ep cross section, σ_{ep}, is calculated from the observed number of D^* mesons in the kinematic region of $p_T(D^*) > 2.5\,\text{GeV}$ and pseudorapidity $-1.5 < \eta(D^*) < 1$. The electroproduction cross sections were transfered to the photoproduction cross sections and extrapolated to the full $(\eta(D^*), p_T(D^*))$ phase space in order to obtain the total charm cross sections.

In Fig. 1.10 the results are compared with the previous ZEUS measurements [2] and fixed target experiments at lower energies [1]. The data are also compared with the predictions from a NLO QCD calculation [24]. The cross section measured at HERA is about one order of magnitude higher than the low energy measurements. It is interesting to know how the cross section behaves in the intermediate region between the fixed-target and the HERA measurements.

The analysis in this thesis with the 44m tagger extends the measurement of the total charm cross section into the new intermediate kinematic region, $80 < W < 120\,\text{GeV}$, not studied before, and allows the differential D^* cross section to be studied with 5 times more statistics than a previous analysis [33]. The analysis with the 35m tagger allows a comparison with the previous H1 tagged (33m tagger) results in an overlapping region: $200 < W_{35m} < 260\,\text{GeV}$, $171 < W_{H1} < 256\,\text{GeV}$.

Previous ZEUS measurements of D^* photoproduction found evidence for an excess in the forward $\eta(D^*)$ region (Sec. 4.3.3) compared to the NLO QCD predictions [8], see for example Fig 1.11 [34]. The points show the measured cross sections, while the solid lines are the massless (lower line) and massive (upper line) NLO QCD calculations. The analysis in the new kinematic region allows an investigation of the angular distribution as a function of W and will help us to understand how well the theoretical models describe the data.

[8] Some ZEUS and H1 results are discussed in Sections 6.3 and 6.4.

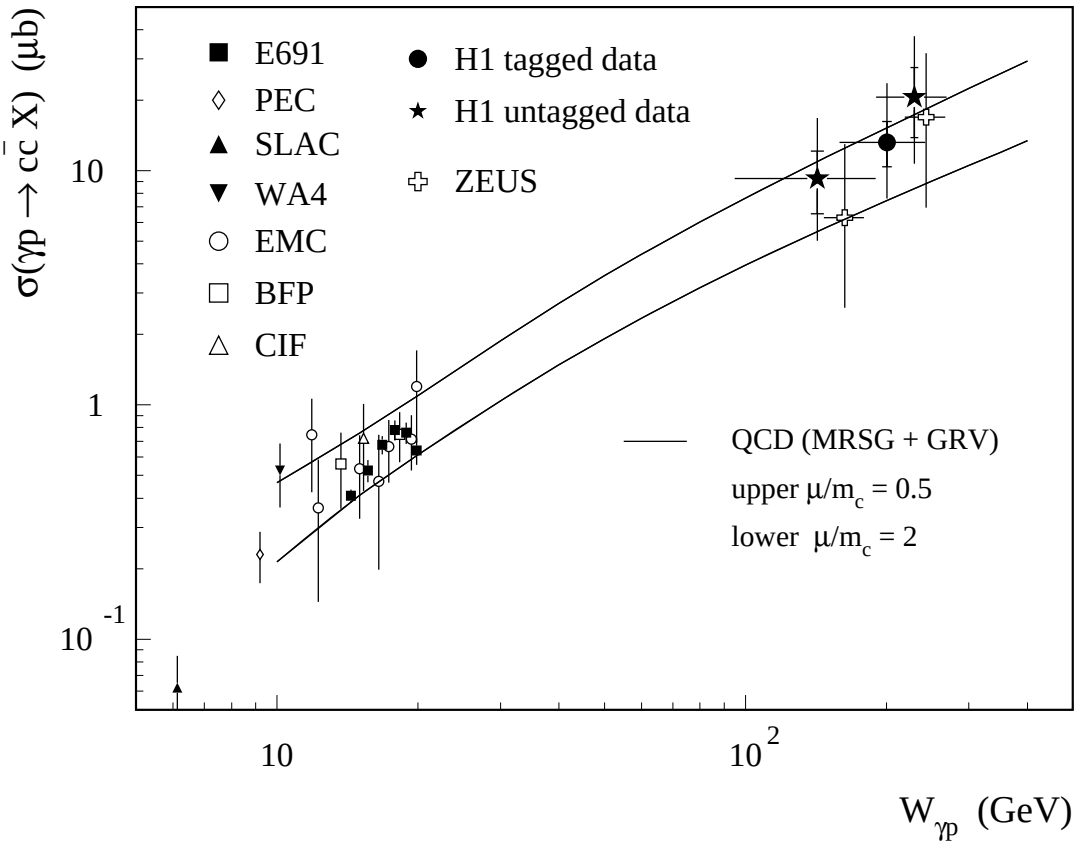

Figure 1.10: Total charm photoproduction cross section as a function of $W_{\gamma p}$. The solid dots and stars represent the analyses done by H1 collaboration. The crosses refer to the results of the ZEUS collaboration. The other symbols indicate earlier measurements at fixed-target experiments. The solid line represents the prediction of a NLO QCD calculation using the MRSG and GRV-G HO parametrisations of the proton and photon parton densities, respectively. The upper and lower lines delimit the range of values expected from varying the renormalisation scale within $0.5 < \mu/m_c < 2$.

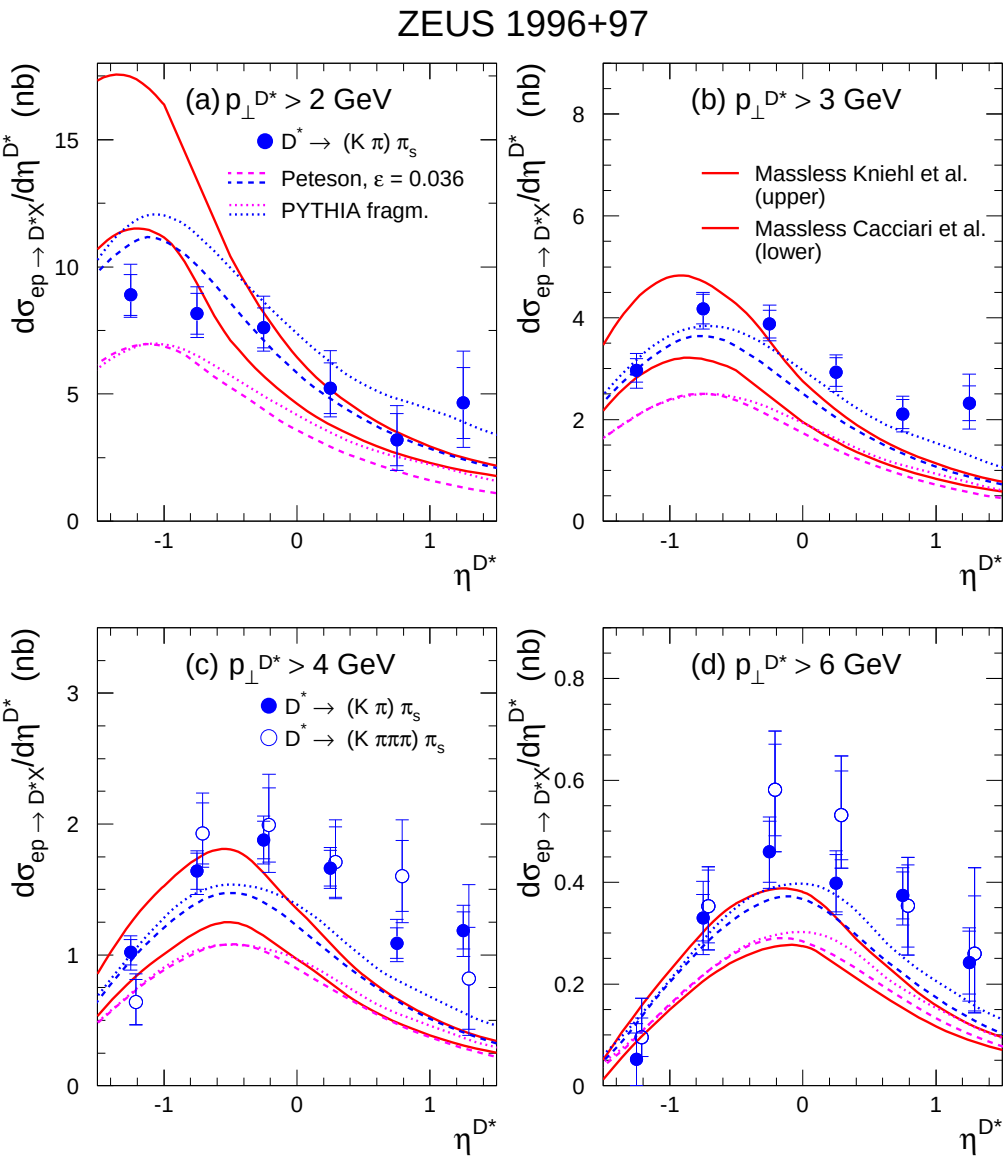

Figure 1.11: Differential cross sections $d\sigma/d\eta(D^*)$ for untagged photoproduction[34].

Chapter 2

Experimental Setup

HERA (Hadron-Electron Ring Accelerator) is the first lepton-proton collider in the world and is located at DESY (Deutsches Elektronen Synchrotron), Hamburg, Germany. It was built during the years 1984-1991 and started luminosity running in 1992.

2.1 HERA Collider

The HERA machine collides electrons or positrons accelerated to an energy of 27.56 GeVwith 920 (820) GeV protons[1].

The HERA collider consists of separate proton and electron rings which are located in a tunnel between 10 and 25 m below ground level. The circumference of the rings is 6.3 km. A schematic view of the HERA collider and its pre-accelerator complex is shown in Figure 2.1. The main HERA parameters are given in the Table 2.1.

HERA parameters	Design Values		Achieved in 1998–2000	
	$e^{\pm}$	p	$e^{\pm}$	p
Circumference [m]	6336			
Energy [GeV]	30	820	27.56	920
Centre-of-mass energy [GeV]	314		318	
Injection energy [GeV]	14	40	12	40
Maximum current [mA]	58	160	37	99
Number of bunches	210	210	174+15 [2]	174+6 [2]
Time between bunch crossings [ns]	96			
Horizontal beam size [mm]	0.301	0.276	0.200	0.200
Vertical beam size [mm]	0.067	0.087	0.054	0.054
Longitudinal beam size [mm]	8	110	8	170
Max. specific luminosity $[\mathrm{cm}^{-2}\mathrm{s}^{-1}\,\mathrm{mA}^{-2}]$	$3.6 \cdot 10^{29}$		$9.9 \cdot 10^{29}$	
Max. inst. luminosity $[\mathrm{cm}^{-2}\mathrm{s}^{-1}]$	$1.5 \cdot 10^{31}$		$1.8 \cdot 10^{31}$	
Integrated luminosity per year $[\mathrm{pb}^{-1}\mathrm{a}^{-1}]$	35		83	

Table 2.1: HERA design parameters and the values achieved in the 1999–2000 running period.

Electrons or positrons are injected into the linear accelerator LINAC, then after accumulation in a small storage ring, with a current of up to 60 mA, they are injected into DESY II

[1] The proton beam energy was changed at the beginning of 1998 from 820 to 920 GeV.

[2] 15 and 6 are the numbers of non-colliding ("pilot") bunches.

before being accelerated up to 7 GeV and transferred to PETRA II (Proton-Electron Tandem Ring Anlage). This procedure is repeated until PETRA is filled with 42 electron bunches with a spacing of 96 ns. There the electrons are accelerated up to 11 GeV and transfered to HERA, where they are accelerated up to 27.56 GeV and have a typical lifetime of 8-15 hours.

Protons are accelerated up to 50 MeV in the LINAC. The stripped ions of hydrogen are injected into the DESY III ring and accelerated up to 7.5 GeV, then transferred to PETRA II, where they are accumulated in 60 bunches and accelerated up to 40 GeV. After that the protons are injected into the superconducting HERA proton ring, where they are accelerated to their final energy 920 GeV.

HERA operates with 210 e and p bunches separated by 96 ns. 174 bunches collide and produce luminosity during the normal operation time, while some of the remaining buckets are used for non-paired ("pilot") e and p bunches, which are used for estimation of background originated from electron or proton beam interactions with residual gas in the beam pipe, trigger rate investigations, etc.

There are four experiments located in the four experimental halls along the HERA ring. For two of them H1, located in the north hall, and ZEUS, located in the south hall, the beams are brought into collision at zero crossing angle. These experiments are designed to analyse data produced in ep collisions and differ mainly in the choices for the design of the calorimetry.

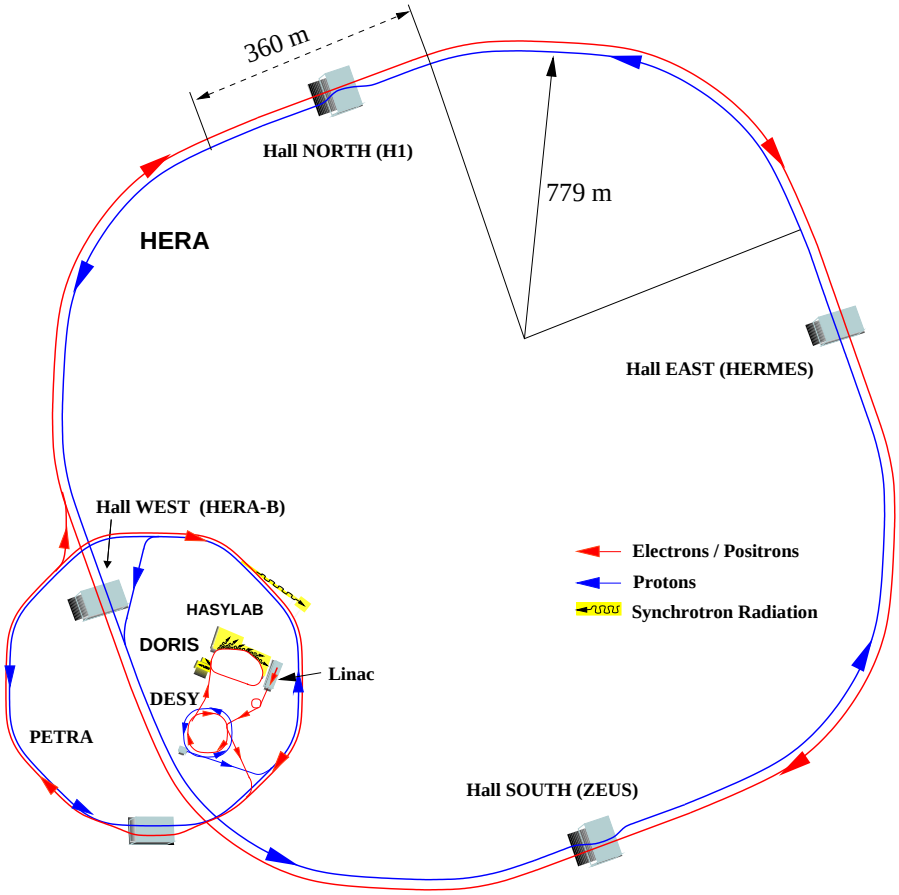

Figure 2.1: The HERA collider. Four circular 90°-arcs are connected with straight sections. In the middle of each straight section there is one experiment. The pre-accelerators Linac, DESY and PETRA are shown as well.

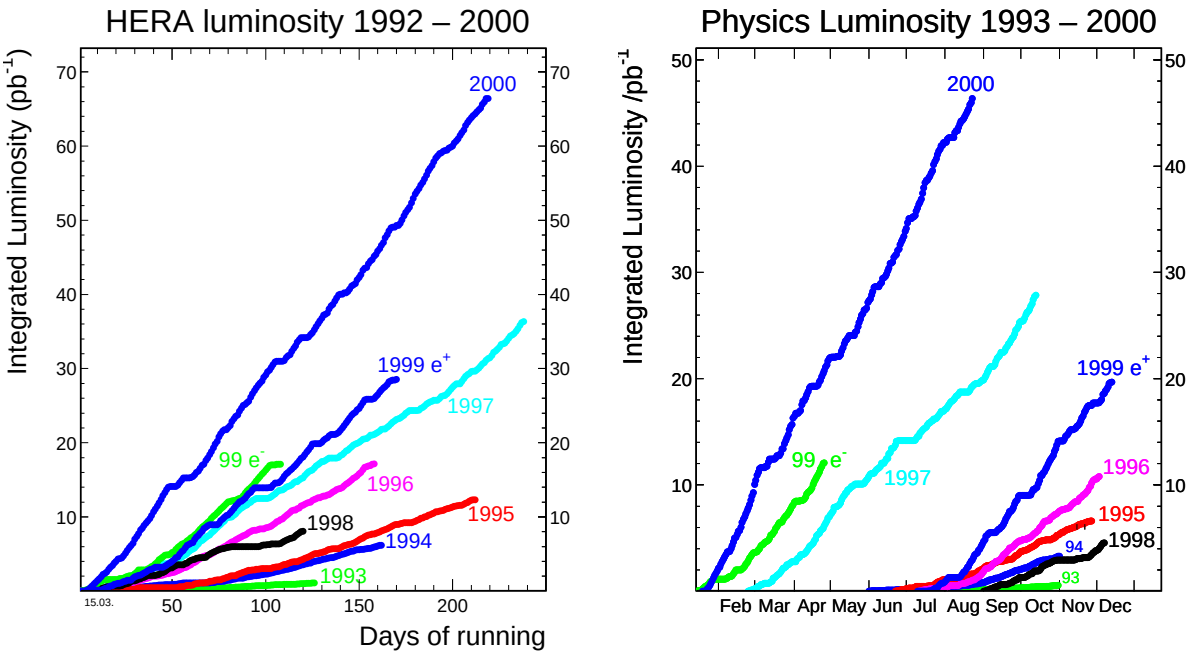

Figure 2.2: Integrated luminosity delivered by HERA in years 1992-2000 (left plot) and integrated luminosity recorded by the ZEUS in the years 1993-2000 (right plot).

A third experiment HERMES uses the polarised electron beam, colliding with a polarised proton (deuterium) gas jet. The fourth experiment HERA-B uses the proton beam only. The left plot in Figure 2.2 shows the integrated luminosity delivered by HERA as a function of days of the run, whereas the right plot shows integrated luminosity recorded by the ZEUS experiment in the years 1993-2000 [35].

2.2 ZEUS Detector

The ZEUS collaboration consists of about 400 physicists from 50 institutes all over the world.

The ZEUS detector is a multipurpose detector [36] designed to study physical processes coming from lepton-proton interactions at HERA. It hermetically covers almost the entire 4π solid angle with the exception of small region around the beam pipe. Due to the large difference between the beam energies the final state particles tend to be boosted in the forward direction which influenced the design of the detector. It is more highly instrumented in the forward (proton direction) region with respect to the interaction point (IP).

The ZEUS coordinate system (see Figure 2.3) is a right-handed orthogonal system with origin at the nominal IP. The z-axis points in the proton (forward) direction, the x-axis points toward the centre of HERA collider and the y-axis points upward. For analysis a polar coordinate system (ρ, θ, ϕ) is usually used, where ρ is a radial distance to the nominal IP, θ is a polar angle measured with respect to the z-axis and ϕ is a azimuthal angle measured with respect to the x-axis. Instead of the polar angle θ the pseudorapidity η[3] is usually used in the analysis. The forward region has positive and the backward region has negative pseudorapidity.

In Figures 2.4 and 2.5 the cross-sectional views of the ZEUS detector are presented. Starting from IP and moving radially outwards one can see the vertex detector (VXD), the

[3]Pseudorapidity is defined as $\eta = -\log(\tan\frac{\theta}{2})$

innermost component in the ZEUS detector, which was removed during 1995 - 1996 shutdown

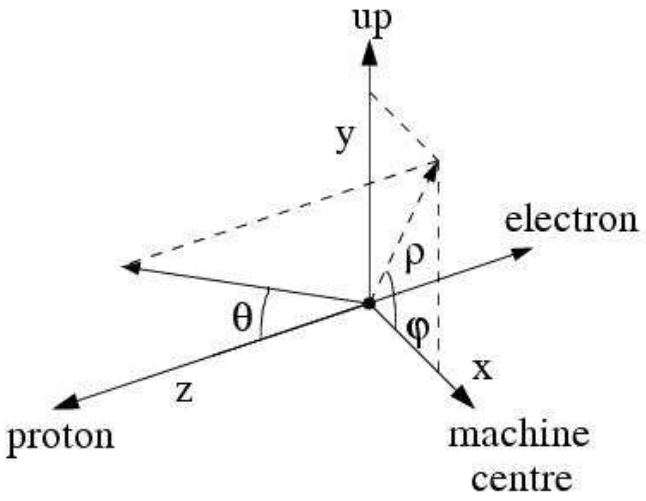

Figure 2.3: The ZEUS coordinate system.

and replaced by the silicon microvertex detector (MVD [37]) in 2001. Then comes the central tracking detector (CTD, see Section 2.3), which is complemented by forward and rear tracking detectors (FDET, RTD). There were 4 modules of the transition radiation detector (TRD) in between the FTDs. During the 2001 shutdown the TRD was replaced by the straw-tube tracking detector (STT), which should improve the efficiency and reliability and the coverage of rapidity of forward tracking. During years 1996 - 2000 CTD was the nearest component to the IP. For charge particle momentum measurement the central tracking detectors are surrounded by a super-conducting solenoid which provides a magnetic field of 1.43 T.

Outside the superconducting magnet comes the ZEUS calorimeter system, which is used for energy measurements of electrons and hadrons. It is consists of the forward (FCAL), the barrel (BCAL) and the rear uranium calorimeter (RCAL), see Section 2.4. To improve the hadron-electron separation for the low energy particles ($< 5\,\mathrm{GeV}$), silicon diodes have been installed near the shower maximum in FCAL and RCAL (so-called the hadron-electron separator, HES). Between RTD and RCAL there is a small tracking detector (SRTD), which covers a radius of about 34 cm around the beampipe. For covering even smaller angles the beam pipe calorimeter (BPC) was installed in front of the RCAL in 1995. In 1998 the forward plug calorimeter (FPC) was installed between beampipe and FCAL, which increased the acceptance of the FCAL by 1 unit in η.

The UCAL system is surrounded by a iron yoke, which provides the return path for the soleniod magnetic field and serves as an absorber for the backing calorimeter (BAC). BAC measures the energy leakage from the main calorimeter. For muon identification limited streamer tubes mounted inside (FMUI, BMUI, RMUI) and outside (FMUON, BMUON, RMUON) the iron yoke. There are special purpose detectors, such as the Veto Wall (VETO) and C5 counter (C5), which installed to veto the backgrounds from non-physics events. For measuring scatterred electrons at angles less then a few mrad and bremsstrahlung photons, 8m, 35m, 44m taggers and photon calorimeter (LUMIG) were installed in the electron beam direction at z

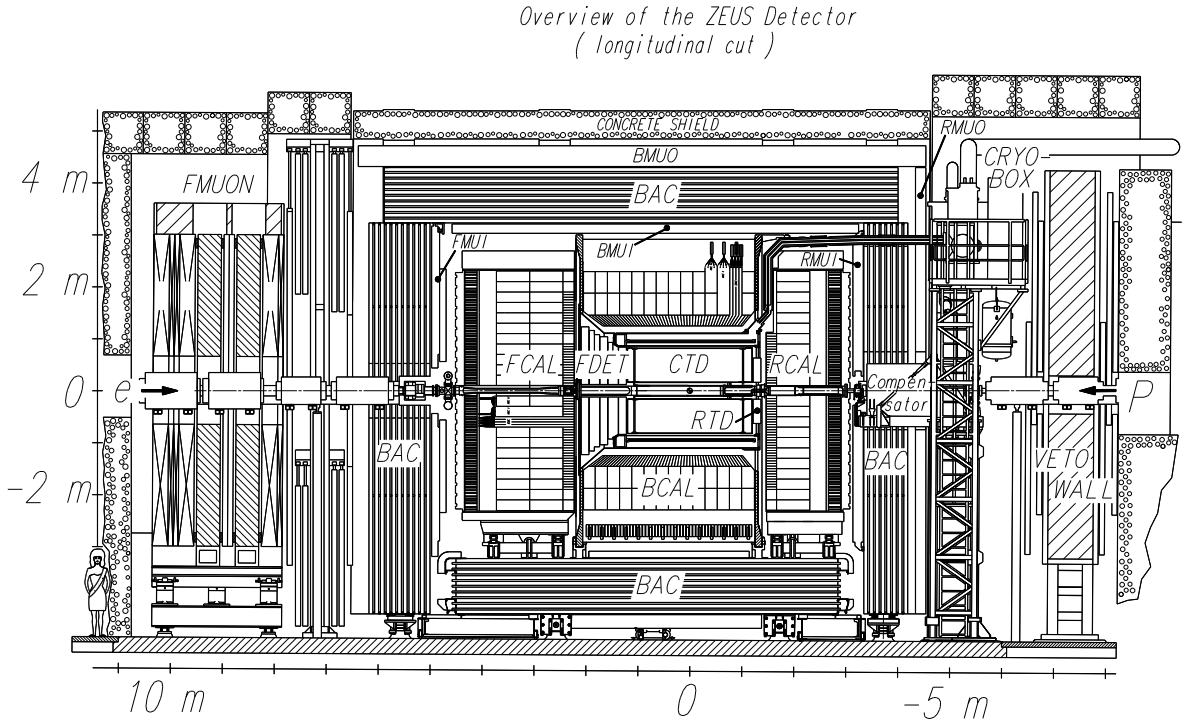

Figure 2.4: Longitudinal cross-sectional view of the ZEUS detector along the beam direction.

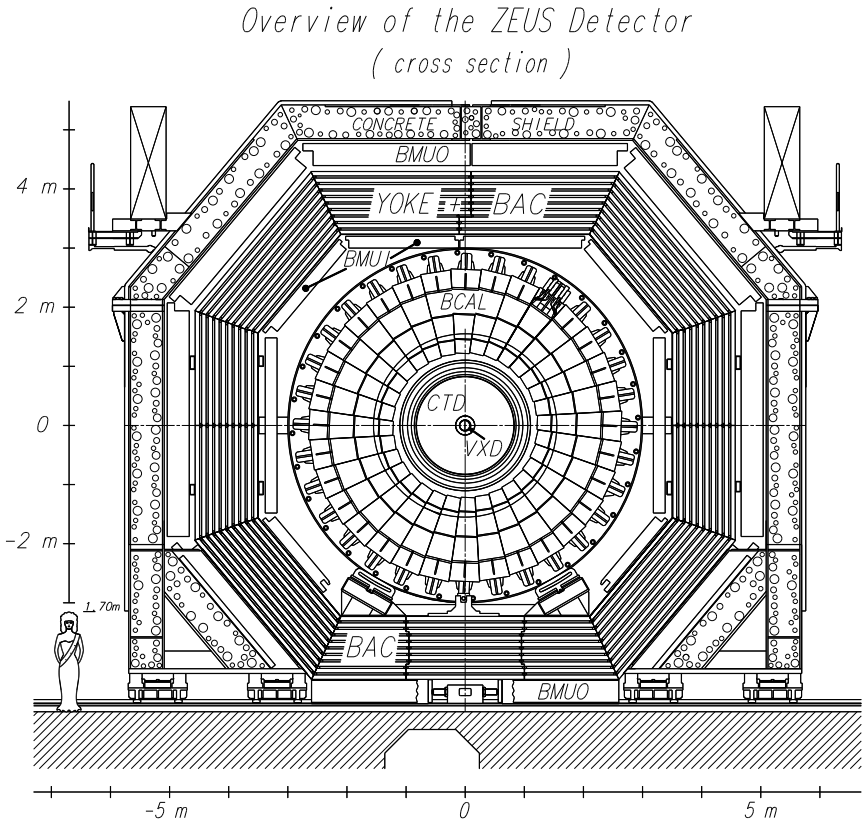

Figure 2.5: Transverse cross-sectional view of the ZEUS detector perpendicular to the beam direction.

values from -8 to -107 m (see Section 2.5).

The most important components for this analysis: the CTD, CAL, taggers and luminosity monitoring systems are described in more detail in the following sections.

2.3 Central Tracking Detector

The Central Tracking Detector (CTD) [38] is a cylindrical drift chamber, which is located in the centre of the ZEUS detector and is used for direction and momentum measurements of charged particles and for particle identification via estimation of the energy loss, dE/dx, information.

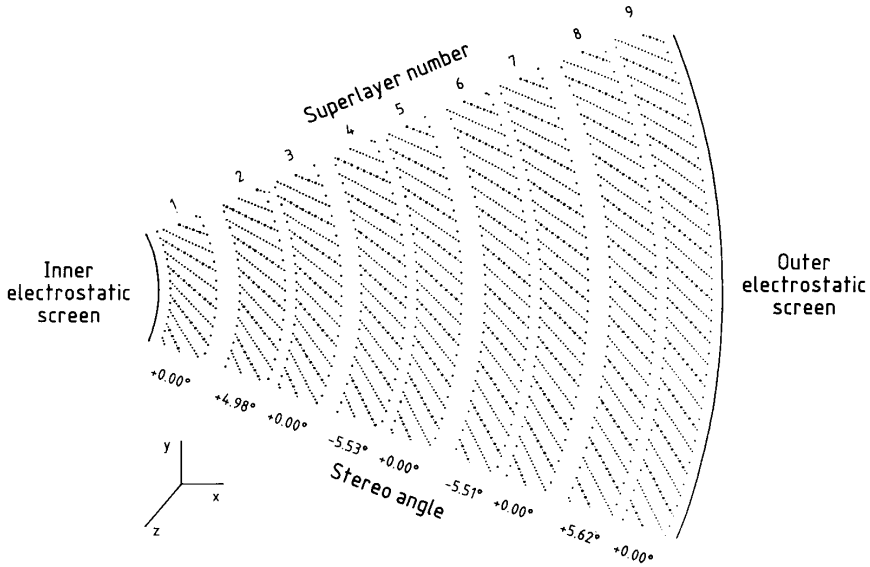

Figure 2.6: Layout of a CTD octant. The stereo angle of each superlayer is indicated.

The detector has an overall length of 2.4 m, an outer radius of 85 cm and an inner radius of 16 cm. Its active region covers the longitudinal interval from z= -100 cm to z= 105 cm with inner and outer radii of 18.2 cm and 79.4 cm, the whole azimuthal angle, ϕ, and the polar angle $15^o < \theta < 164^o$. The CTD is filled with a mixture of argon (Ar), carbon dioxide (CO_2) and ethane (C_2H_6) in the proportions 83 : 5 : 12. It consists of 4608 sense wires ordered in 72 concentric layers, which are arranged in 9 superlayers (SL). Each SL is divided into cells with 8 sense wires in each. The number of cells per SL increases from the inner most to outer most layer. Figure 2.6 shows the layout of the one CTD octant. Sense wires in the odd numbered SL are oriented parallel to the beampipe, while the wires in the even numbered SL are tilted by $\approx \pm 5^o$. The reconstructed z-position is estimated by combining the the signal from odd and even superlayers and is about 1.5 mm for the reconstructed tracks. This method is called z-by-stereo. There is also the so-called z-by-timing method of determination of z position of the hit. For that purpose, the three inner axial SLs (SL1, SL3 and SL5) are equipped with a system, which determines the z position using the information on the arrival time of the signal at each end of the sense wire. The z-resolution measured by this method is about 4 cm. The CTD has a transverse momentum resolution [39] of

$$\sigma(p_T)/p_T = (0.58 p_T[\,\mathrm{GeV}] \oplus 0.65 \oplus 0.14/p_T[\,\mathrm{GeV}])\%. \qquad (2.1)$$

2.4 Uranium Calorimeter

The ZEUS calorimeter [40] is a sandwich uranium-scintillator calorimeter (UCAL), which completely surrounds the tracking devices and the solenoid, and covers 99.7% of the 4π solid angle. It consists of 3.3 mm thick depleted uranium plates alternated with 2.6 mm thick plastic scintillator plates. This design have been chosen in order to have the same respone for electromagnetic and hadronic particles ($e/h = 1$). Hence it is a compensating calorimeter. It is divided into 3 parts, the forward (FCAL), barrel (BCAL) and rear (RCAL) calorimeters. The FCAL covers polar angles from 2.2^o to 39.9^o. The BCAL covers from 36.7^o to 129.1^o and the RCAL from 128.1^o to 178.4^o. In Figure 2.7 an example of the FCAL module is shown. FCAL module consists of one electromagnetic (EMC) section (first 25 uranium-scintillator layers) and two hadronic (HAC) sections (remaining 160 uranium-scintillator layers). The electromagnetic section has a depth of 26 X_0, while each hadronic section is 3.1 λ deep. The EMC and HAC cells are superimposed to form a rectangular tower. BCAL consists of one EMC (first 21 uranium-scintillator layers) and two HAC (remaining 98 layers) sections. The resulting depth is 21 X_0 for EMC section and 2.0 λ for each hadronic section. The RCAL is made up of 23 modules similar to those in the FCAL, and has only one HAC section with a depth of 3.1 λ and a depth of 26 X_0 for the EMC part. The main parameters of the CAL are given in Table 2.2. The light produced in the scintillators is absorved and rertransmitted by 2mm thick wavelength shifter (WLS) bars at both sides of the module, and brought to one of the 11386 photomultiplier tubes (PMT) where it is converted into an electrical signal.

	FCAL	BCAL	RCAL
Theta range $[^o]$	$2.2 < \theta < 39.9$	$36.7 < \theta < 129.1$	$128.1 < \theta < 176.5$
η	$4.0 > \eta > 1.0$	$1.1 > \eta > -0.74$	$-0.72 > \eta > -3.49$
Number of modules	23	32	23
Number of towers per module	11-23	14	11-23
Number of cells	2172	2592	1152
Length $[cm]$	152.5	105.9	87.0
Radiation length $[X_0]$	25.9	24.6	24.3
Absorption lengths $[\lambda]$	7.1	4.9	4.0

Table 2.2: Parameters of the uranium calorimeter.

The calorimeter resolution measured in test-beam for electrons is

$$\frac{\sigma(E)}{E} = \frac{18\%}{\sqrt{E}} \oplus 2\%, \tag{2.2}$$

and for hadrons is

$$\frac{\sigma_h(E)}{E} = \frac{35\%}{\sqrt{E}} \oplus 1\%, \tag{2.3}$$

where E is the particle energy in GeV.

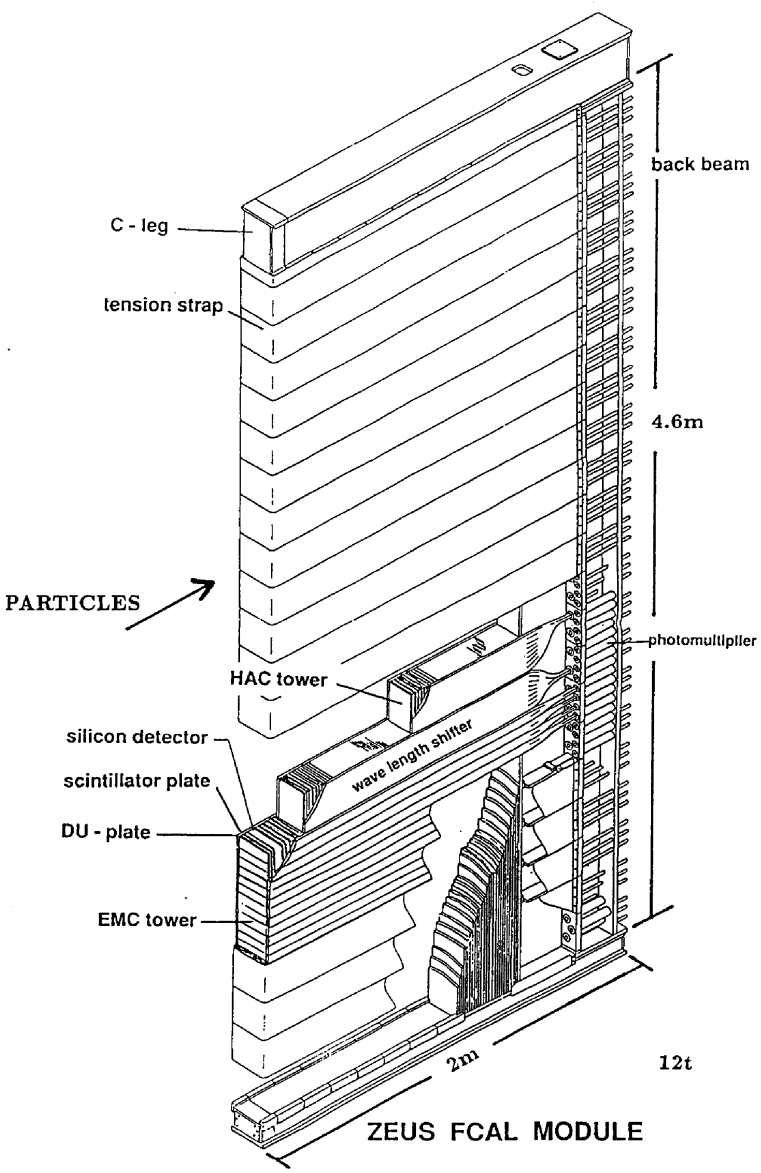

Figure 2.7: Layout of a FCAL module. The FCAL modules are subdivided into one EMC and two HAC sections, which in turn are divided into towers.

2.5 Electron Taggers

The scattered electron coming from the photoproduction events at ZEUS can be measured by three electron calorimeters (taggers), which are placed near the beamline at $Z = -8, -35, -44m$ (see Figure 2.8). Due to the geometry, taggers detect electrons scattered under angles smaller than a few mrad and accept different regions of the electron energy spectrum. The 8m tagger measures electrons in the energy range $1.37 < E < 6.2$ GeV, which corresponds to a W range $280 < W < 310$ GeV. The 35 and 44m taggers cover lower W ranges (see Figure 2.9).

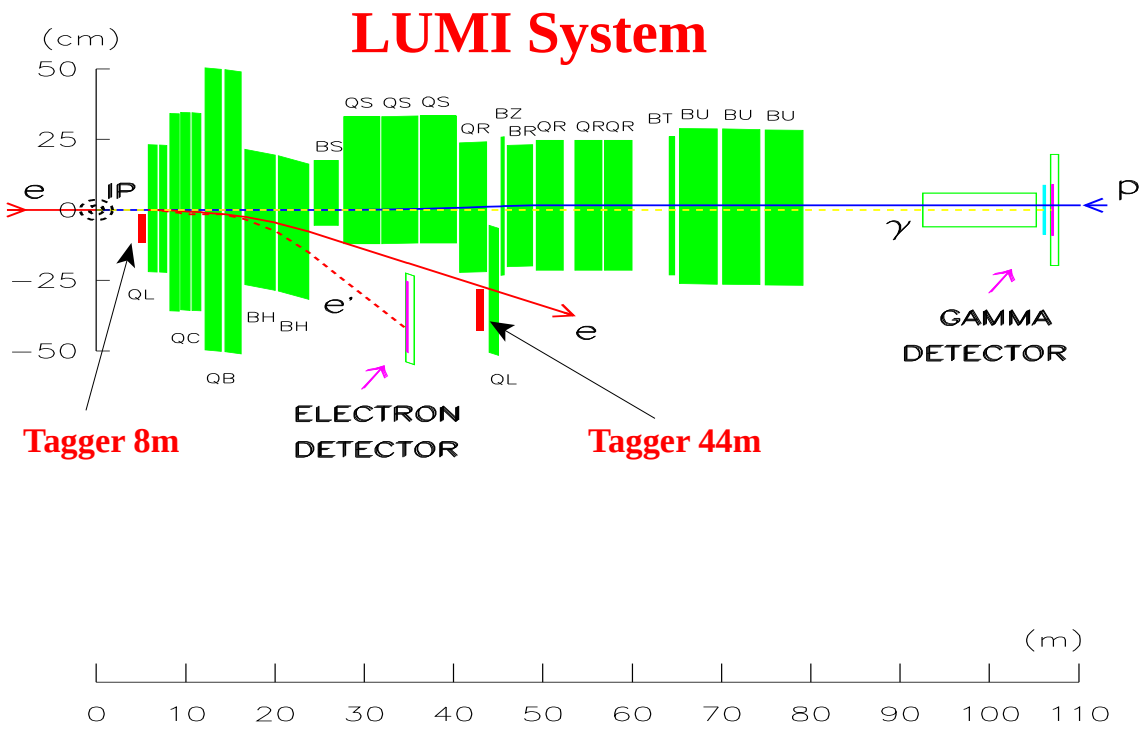

Figure 2.8: The luminosity monitor system, 8m and 44m taggers position. The longitudinal axis is highly compressed. The 35m tagger is part of the luminosity system (electron detector). The shaded boxes are thebeam magnets.

2.5.1 44m Tagger

The 44m tagger is placed 44 m away from the interaction point and measures scattered electrons in the energy range $21 < E_e < 26$ GeV, which corresponds to the photoproduction events with a W range $70 < W_{\gamma p} < 140$ GeV. The tagger is located very near to the beampipe, which makes the precise energy measurement of the scattered electron difficult. The acceptance of the tagger is mainly determined by its geometrical location and calculated with the help of the photon calorimeter called gamma detector in Fig. 2.8 (see Section 4.4).

The 44m tagger is a small $24X_0$ deep tungsten-scintillator sandwich calorimeter located about 10 cm behind the electron exit window [41]. It consists of 12 layers of tungsten plates of size $70 \times 90 \times 7\text{mm}^3$ and 3 mm thick scintillators (see figure 2.10). The scattered electron position in the detector is measured by sets of three 8mm wide scintillator strips inserted after 4, 6, and $8X_0$ along the z-axis. The strips are connected at the top end to plastic light guides,

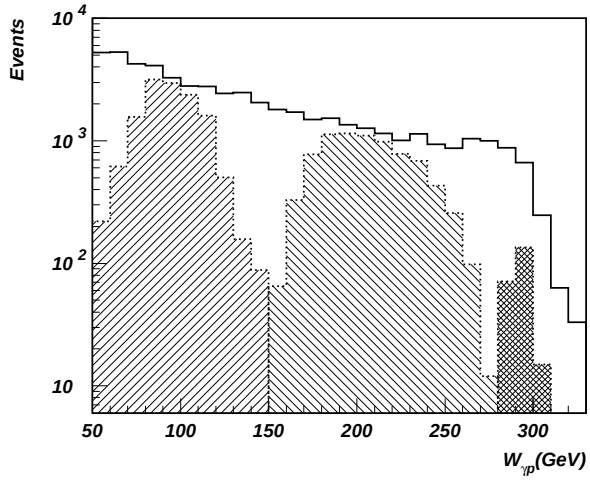

Figure 2.9: The W range of the tagged photoproduction events at ZEUS measured by different electron calorimeters located along the beamline. The 8m tagger covers the large W range, the 35m tagger covers the intermediate W range, and the 44m tagger covers the low W range. The open histogram shows the W distribution of all photoproduction events.

from where the signal goes to three photomultipliers. The detector is sensitive to electrons with scattering angle θ such that $Q^2 < 0.015\,\mathrm{GeV}^2$. Test beam measurements with electrons hitting the tagger with energies 1-5 GeV gave a relative energy resolution of $0.25/\sqrt{E(\,\mathrm{GeV})}$, and a calorimeter linearity better then 1%. In the experiment the resolution is much worse and therefore the energy information is not used for data analysis.

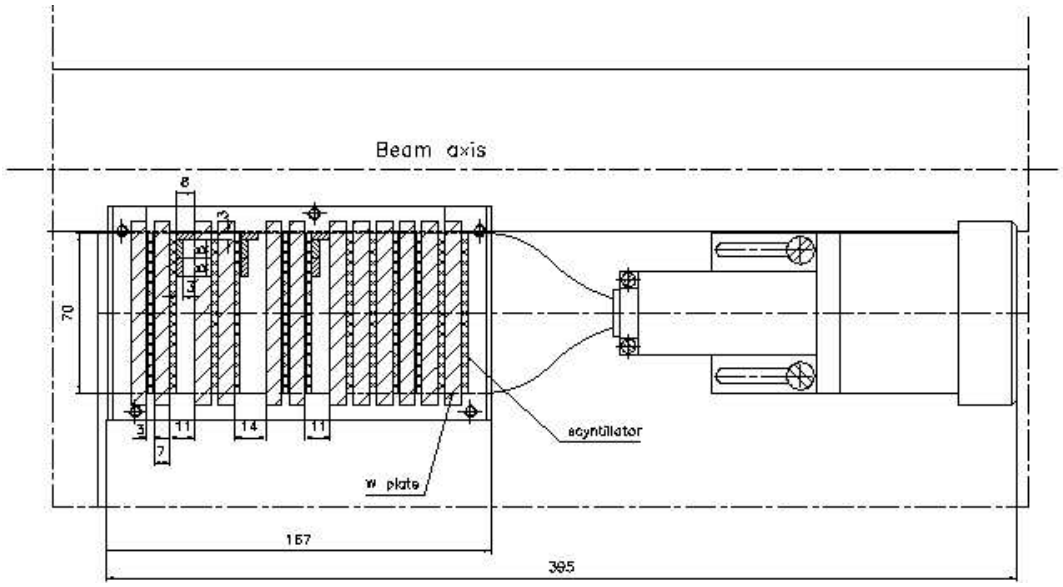

Figure 2.10: Horizontal cross-section of the 44m electron calorimeter with position.

2.5.2 35m Tagger

The 35m tagger (LUMI-e calorimeter, see Figures 2.8) is placed 35 m away from the interaction point and measures scattered electrons in the energy range $5 < E_e < 18$ GeV, which corresponds to photoproduction events with a W range $140 < W_{\gamma p} < 250\,\mathrm{GeV}$. The scattered electrons are deflected by the beam magnets and leave the electron beampipe through a 1.5 mm thick exit window at a distance of 27.3 m from the interaction point and hit the tagger at Z=-35 m. The tagger consists of a $21X_0$ deep lead-scintillator calorimeter with a position detector installed at a depth of $7X_0$. For calibration purposes there is scintillator finger in front of the calorimeter. The tagger is installed on a movable and remotely controlled table, which allows the shift crew to move the calorimeter into a parking position during injection and tests of the electron beam. The detector is sensitive to the electrons with scattering angle $\theta < 5$mrad and $Q^2 < 0.02\,\mathrm{GeV}^2$.

2.5.3 Luminosity Monitor

An important part of cross-section calculations is the measurement of the luminosity, which is defined as

$$L = \frac{N}{A\,\sigma}, \tag{2.4}$$

where N is the number of events of a process, A is the acceptance and σ its cross section. Hence luminosity can be calculated if the cross-section of a process is well known and if the rate of a process can be measured very well. For the ZEUS luminosity measurements [42] the bremsstrahlung process $ep \to e'\gamma p$ was chosen, for which the cross section is large and precisely known from QED with an accuracy of 0.5%.

The luminosity monitor at the ZEUS is located in the tunnel in the direction of outgoing electron beam and consists of two parts, the photon and electron "branches" which measure the energy and position of the bremsstrahlung photon and electron respectively. The scattered electrons are deflected by the HERA magnet system from nominal orbit and leave the vacuum pipe through a thin window and hit the LUMI-e calorimeter (35m tagger, see 2.5.2), while the bremsstrahlung photons are not deflected by the magnetic fields and leave the vacuum pipe at Z=-92 m through a 1.5 mm thick exit window and hit the LUMI-γ calorimeter at Z=-107 m (see Figure 2.8). LUMI-γ is a lead-scintillator calorimeter with a position detector inserted at a depth of $7X_0$ and a resolution of about 2mm. In front of the calorimeter there is a carbon filter which reduces the flux of synchrotron photons. The bremmstrahlung process can be measured by the coincidence of an electron in the LUMI-e detector and a photon in the LUMI-γ detector. ZEUS, however, decided to use only LUMI-γ detector, using just the photon flux ($E_\gamma > 5\,\mathrm{GeV}$), to reduce the systematic errors in the luminosity measurement. The coincidence rate was used only for a cross check. For estimation of the background coming from the interaction of beam electrons with atoms of residual gas in the beam-pipe the electron pilot bunches were used.

2.6 Trigger and Data Acquisition

The HERA collider produces bunch crossings every 96 ns, which is equivalent to a rate of ≈ 10 MHz. Besides the real ep events, there is an enormous number of background events, whose rate is higher than the rate of physics events by several orders of magnitude. This background comes from interactions of leptons or protons with the residual gas in the beam-pipe, from interactions in the beam-pipe halo with the collimators and from cosmic ray muons. In order to select efficiently interesting events and suppress the background rate from its initial value

to a few Hz[4] the ZEUS trigger system has a three level architecture [36], which is shown in Figure 2.11.

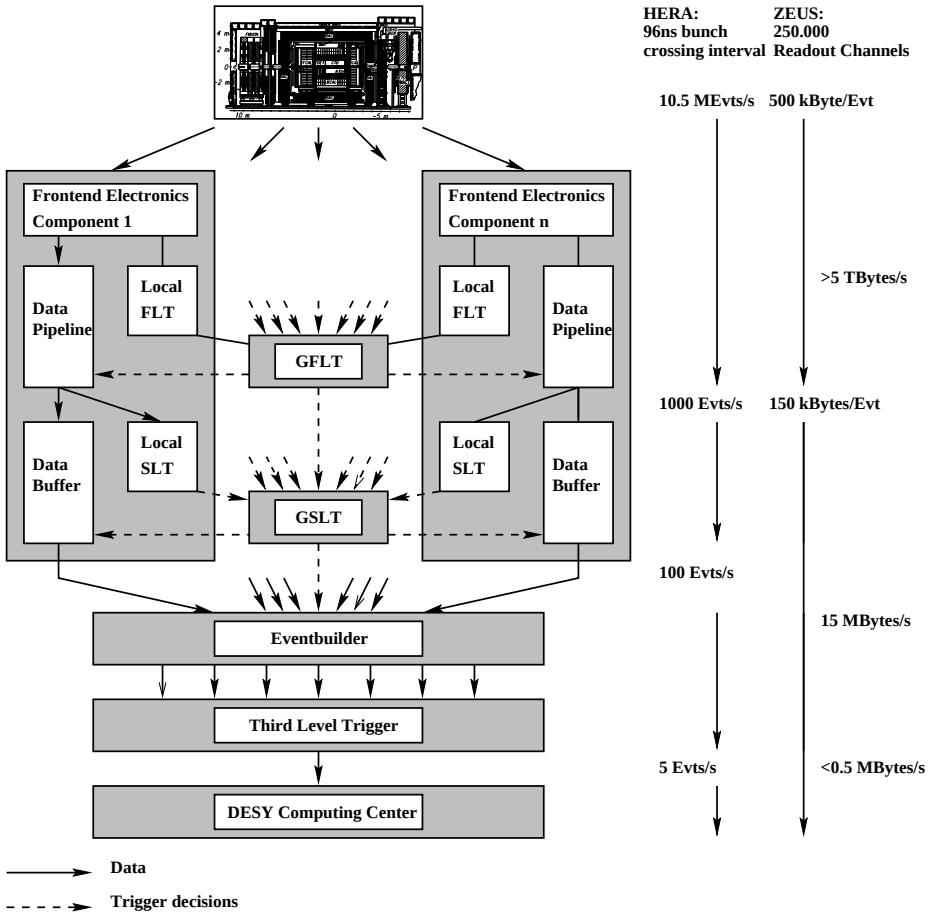

Figure 2.11: Schematic layout of the trigger and readout system of ZEUS.

The First Level Trigger (FLT) is a hardware trigger which suppresses most of the beam-gas and beam-halo background and has an output rate below 1 kHz. Every component has its own FLT interface, which stores the data in analogue[5] or digital pipelines and makes the decision within 2 μs. Then, the decisions of local FLTs go to the global first level trigger (GFLT), which is a logical OR of 64 sub-trigger slots. The GFLT gives the decision to accept/reject event after 46 bunch crossings, which is 4.4 μs.

After passing the GFLT, the data are digitized and transfered to the Second Level Trigger (GSLT), which is software-based and based on more global event information. The GSLT reduce the GFLT rate from 1 kHz to 100 Hz. The GSLT decision is also based on local SLT information from the components and calculated within 10 ms. After a GSLT trigger the remaining data are transfered to the event builder (EVB).

The EVB combines the accepted data from all components, writes them in a standard (ADAMO) format and transfers them to the third level trigger (TLT). The TLT is a software-based trigger, which runs a reduced version of the offline reconstruction code. The output rate of TLT is about 5 Hz. The data accepted by the TLT are written on tape.

[4]Few Hz of output trigger rate comes from maximum rate with which data can be written to tape.
[5]Ror example for the calorimeter the pipeline is an analogue device, which stores charge.

-

Chapter 3

Monte Carlo Simulation

3.1 Overview

The ZEUS detector is a highly complex and complicated system. Therefore the measurements need corrections which take into account the effects of detector resolution, efficiency and acceptance.

A better understanding of the data and of the detector behavior can be achieved by simulating the detector response to physics events. In addition, the different theoretical models implemented in the simulations can be tested by comparing them with the data.

In the first section the event generators used for this analysis are described. The next section the NLO theoretical calculation (FMNR) for charm production in PHP is explained. In the last section the detector and trigger simulation programs are discussed. More detailed information about the offline analysis and the reconstruction can be found in [43].

3.2 Event Generators

An "Event generator" is a program which simulates the physics processes. QCD Monte Carlo (MC) event generators divide the simulation of scattering process into different phases, corresponding to increasing scales of distance and time. It makes use of the factorization theorem [44], see Fig. 3.1.

The *ep* scattering process generally can be split (factorised) into the following separate components:

Hard sub-scatter. It describes the process of the interaction between incoming beam particles. In our case it is the parton extracted from the proton, and the photon or a photon component in resolved photon events. The computation of the pair interaction is based on leading order (LO) QCD matrix elements. The flavour and momentum of the incoming parton are chosen according to the selected parton density function (PDF) [45]. The hard momentum transfer scale μ sets the boundary condition for the initial state and final state parton showers.

Initial state and final state radiation (Parton shower). It simulates the higher order QCD initial state and final state radiation. The common model is the so-called *parton shower method*, where the radiation is simulated by a random number of branchings of one to two partons, like: $e \rightarrow e\gamma$, $q \rightarrow qg$, $q \rightarrow q\gamma$, $g \rightarrow q\overline{q}$. A parton, constituent of the incident hadron (photon) and having low space-like virtuality, can radiate time-like partons via *initial state radiation*. In the process it increases its space-like virtuality ($m^2 < 0$ and $m^2 = E^2 - \overrightarrow{p^2}$) and decreases the parton energy to a fraction x of that of the beam. On the other hand, an outgoing virtual parton, with large time-like mass ($m^2 > 0$), can generate a

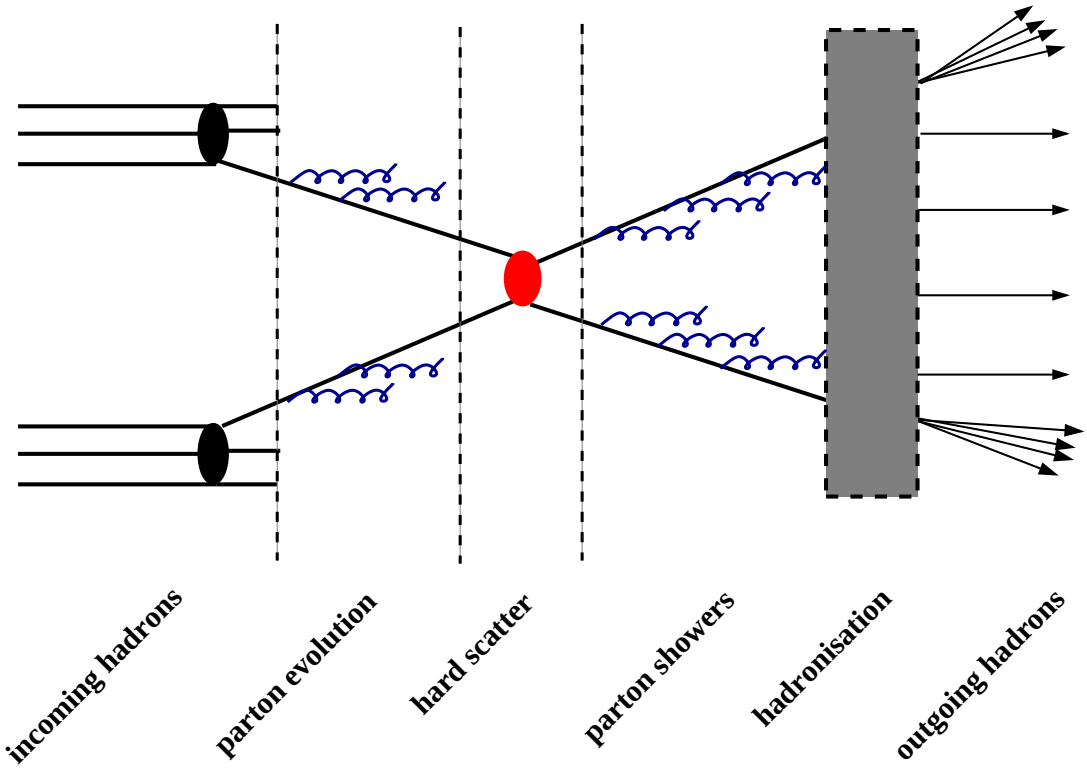

Figure 3.1: Schematic view of the processes in a generator.

shower of partons via *final state radiation*, having lower virtuality. This cascade stops at some fixed scale μ_0 smaller than ~ 1 GeV, below which a perturbative approach is no longer valid, since α_s is large.

Hadronisation or fragmentation. It is the process in which the coloured partons are combined to form the colourless hadrons after the parton shower. It is a non-perturbative process due to its low momentum transfer scale (the strong coupling α_s is large). Such processes are still not well understood and are therefore described by phenomenological models. The main hadronization models available now are the cluster model, which is implemented in the HERWIG MC program (see 3.2.1), and the string model, which is implemented in PYTHIA MC program(see 3.2.2).

Resonance decay. In this process the unstable hadrons formed during the hadronisation process decay according to their branching ratios.

For this analysis the HERWIG and PYTHIA generators can in principle be used to simulate charm photoproduction. In the next two subsections the main features of these generators are discussed. For more comparison between them see [46].

3.2.1 HERWIG

The HERWIG (Hadron Emission Reactions With Interfering Gluons) [47] MC generator is a general purpose event generator for high energy processes, which provides a full simulation of lepton-lepton, lepton-hadron and hadron-hadron interactions. It is characterized by a small

number of free parameters and is as independent as possible of non-perturbative parameters.

HERWIG has a large library of QCD, electroweak and supersymmetric elementary sub-processes. These sub-processes play an important role in defining the phase space of the initial and final state partons which then undergo parton showers according to the DGLAP (Gribov-Lipatov-Altarelly-Parisi) splitting functions. The available phase space for the parton showers is restricted to an angular-ordered region, and the leading infrared singularities are correctly taken into account.

In the case of final state radiation, at each branching, the angle between the two emitted partons is smaller than that of the previous one, the scale of α_s is the relative transverse momentum of two daughter partons. In the case of heavy flavour production the mass of the quark modifies the angular-ordered phase space and the soft radiation in the direction of the heavy quark is depleted. Emission within a cone with an opening angle m_Q/E_Q, where m_Q and E_Q are the mass and the energy of the heavy quark, is suppressed. This is known as the "dead cone".

In the case of initial state radiation, the properties which characterize this process include all those discussed for final state emission. However, the angular ordering restriction on the phase space applies to the angle θ_i between the incoming hadron and the emitted partons i.

The entire parton structure is generated based on the hard sub-process. The factorization scale for the hard sub-process, μ^2, is given by,

$$\mu^2 = \frac{2\hat{s}\hat{t}\hat{u}}{\hat{s}^2 + \hat{t}^2 + \hat{u}^2}, \tag{3.1}$$

where, $\hat{s}$, $\hat{t}$ and $\hat{u}$ are the Mandelstam variables. The resulting cross-section for light flavour production is divergent in the limit $p_T \to 0$, therefore a cut on the minimum transverse momentum of the produced partons is introduced.

HERWIG direct photoproduction is calculated based upon the exact LO matrix elements. For the resolved process the equivalent photon approximation (EPA) [48] is used. The backward evolution in HERWIG allows the possibility for a $\gamma \to q\overline{q}$ vertex at each stage in resolved events.

The hadronisation process is described by a non-perturbative model called the *cluster* model, Fig. 3.2, which groups the partons into colour neutral objects. The gluons are split into light (u or d) quark-antiquark or diquark-antidiquark pairs. The splitting into diquarks is suppressed with respect to that into quarks. These are subsequently clustered into colourless objects via colour connections generated in the parton shower. Then each cluster is fragmented into two hadrons or the lightest hadron for its flavor if the cluster is not massive enough. Finally the decay of unstable particles is simulated.

For this analysis HERWIG version 6.301 is used.

3.2.2 PYTHIA

The PYTHIA MC [49] is a general purpose generator, which shares many common features with HERWIG. However, there are significant differences, in particular in the treatment of non-perturbative processes. PYTHIA describes the hadronization processes in as much detail as possible. There are also two significant differences in the perturbative phases. In PYTHIA the photon spectrum for photoproduction events is generated using the Weizsäcker and Williams (WWA) approximation [50, 51] for both direct and resolved processes. Another difference is the factorization scale, μ^2, used is the transverse mass of the two outgoing partons, ${m_T}^2$, given by,

$$\mu^2 = {m_T}^2 = \frac{1}{2}({m_1}^2 + {p_{T1}}^2 + {m_2}^2 + {p_{T2}}^2) = \frac{1}{2}({m_1}^2 + {m_2}^2) + \frac{\hat{t}\hat{u} - {m_1}^2 + {m_2}^2}{\hat{s}}, \tag{3.2}$$

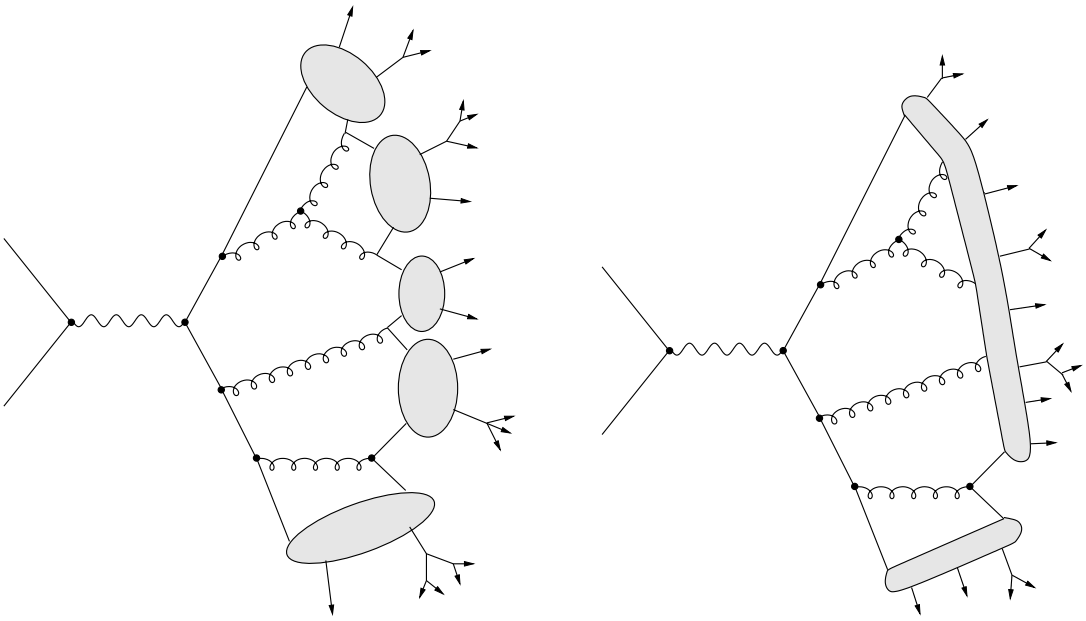

Figure 3.2: Hadronisation models, (a) shows a sketch of the cluster hadronization model as used in HERWIG while the string fragmentation model as used in PYTHIA is shown in (b).

whereas the scale used by HERWIG is given by the Formula 3.1.

The parton shower evolution is conceptually the same in both generators, but in PYTHIA the parton emissions are ordered only according to the virtuality of the radiated partons. The parton radiation stops at some cutoff scale Q_0^2 of the order of 1 GeV^2.

In PYTHIA the partons are hadronized using the *Lund String Fragmentation* model [52]. The string model is based on the starting assumption of a linear confinement picture. According to this model, the energy stored in the colour dipole field between a colour charge and an anticharge increases linearly with the separation between the charges. In this model the partons are connected with *strings* the strength of which is about 1 GeV/fm, see Figure 3.2 (b). As the partons move apart the potential energy stored in the string increases, and the string may break producing $q\overline{q}$ pair. When the energy of a string is too small to enable further separation of the partons, hadrons are formed. Then the unstable hadrons are decayed as in HERWIG.

3.3 Next-to-Leading Order Program FMNR

Next-to-leading order (NLO) corrections are required to improve the knowledge of the heavy-quark production cross-section mainly by reducing the uncertainties related to the renormalization and factorization scale dependence. The corrections come from real and virtual parton emissions.

The NLO QCD calculation of charm photoproduction and electroproduction used in this analysis was developed by Frixione et al [24, 25, 53]. The calculation is based on the massive scheme, which assumes that the charm quark is massive, while the light quarks (u, d, s) are considered massless. The FORTRAN code implementing this calculation was developed by the authors (S. Frixione, M. Mangano, P. Nason, G. Ridolfi). We call this program FMNR by taking the initial letters of the authors. The calculation includes the parton level processes summarized in Table 3.1.

In the FMNR photon-proton cross sections are written as a sum of two contributions. The first is the point-like component, where the photon directly interacts with the parton from the

Direct Process		
LO	NLO	
$\gamma g \to c\overline{c}$	virtual correction	$\gamma g \to c\overline{c}$
	real correction	$\gamma g \to c\overline{c}g$
		$\gamma q \to c\overline{c}q$
Resolved Process		
LO	NLO	
$gg \to c\overline{c}$	virtual correction	$gg \to c\overline{c}$
$q\overline{q} \to c\overline{c}$		$q\overline{q} \to c\overline{c}$
	real correction	$gg \to c\overline{c}g$
		$q\overline{q} \to c\overline{c}g$
		$qg \to c\overline{c}q$
		$\overline{q}g \to c\overline{c}\,\overline{q}$

Table 3.1: Parton level processes included in FMNR.

proton. The second one is the hadronic (or resolved) photon component, where the photon splits into partons that eventually collide with proton. Electroproduction cross-sections can be obtained from photoproduction cross-sections via convolution with the Weizsäcker-Williams function.

Figure 3.3 shows some examples of leading-order (LO) diagrams calculated in FMNR. Figure 3.4 shows some examples of diagrams at NLO, involved in the direct process. Figure 3.4 (a) shows an example of the virtual correction, which involves a loop integral. Figure 3.4 (b) - (d) show examples of real corrections. Although FMNR does not explicitly consider the charm PDF in the photon, diagram like in Figure 3.4(c) partially include this effect since the

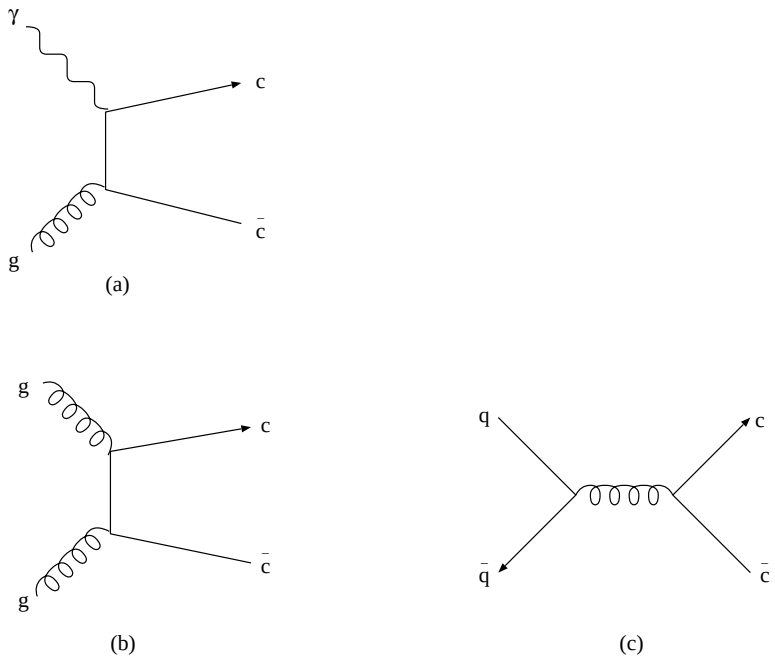

Figure 3.3: Examples of LO diagrams for charm production.

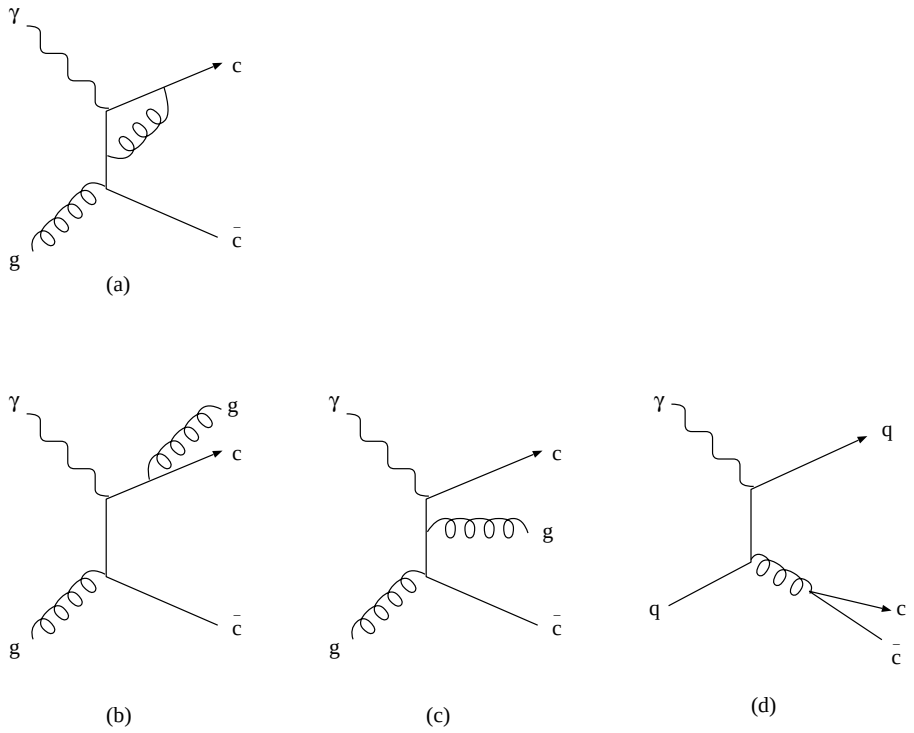

Figure 3.4: Examples of diagrams involving in NLO correction for direct photon process. Virtual correction to BGF diagram (a), and real corrections (b), (c) and (d) are shown.

photon couples to the $c\bar{c}$ and so if the virtuality of the charm propagator between the photon and top gluon vertex were less than the photon factorisation scale, then this diagram would be included in the resolved photon component if an explicit charm contribution to the photon PDF were considered. The definition of direct and resolved process depends order-by-order in perturbative calculation.

FMNR is implemented as a "parton" event generator available in FORTRAN code [53, 54]. The calculation is performed in such a way that the cancellation of soft and collinear singularities takes place under the integral sign. This enables us to apply various cuts performed in the experiment.

In FMNR the default value of the charm quark is set to $m_c = 1.5\,\text{GeV}$. The renormalization scale is taken $\mu_R = \mu_0$ and the factorization scale for the proton and for the photon is taken as $\mu_F = \mu_\gamma = 2\mu_0$, where $\mu_0 = \sqrt{p_T^2 + m_c^2}$. Charm fragmentation to a D^* is carried out using the Peterson fragmentation function, the Peterson parameter is set to $\epsilon = 0.035$. For more details see Sec. 6.2.

3.4 ZEUS Detector Simulation and Event Reconstruction Chain

All event generators (like HERWIG, PYTHIA), which create a list of particles produced in an *ep* interaction and their four-momenta with the all relevant kinematic variables, are gathered in the software program AMADEUS (Zeus Interface to Monte Carlo Generator). For simulating the detector response, the events are processed by the MOZART (Monte Carlo for ZEUS Analysis, Reconstruction and Trigger) [55] program. MOZART is based on the GEANT [56] package, which contains a description of all the detector components, such as the material they are made of, their exact geometry and position. It also simulates the passage of particles through the whole detector taking into account physics processes such as energy loss, multiple

scattering, decay of particles, etc.

The output of the simulation then is fed into a CZAR (Complete Zgana Analysis Routines) [57] package, which contains the First and Second Level Trigger simulations in ZGANA and the Third Level Trigger simulation in TLT-ZGANA. CZAR simulates the logic of the triggers as implemented during the data-taking.

After passing the trigger simulation, the events are fed into the reconstruction program ZEPHYR (ZEUS Physics Reconstruction), which produces reconstructed objects and writes them in MDST (mini data storage tape) files and which contain calibrated detector quantities such as calorimeter energy, tracks, vertices, lumi[1] information, etc. ZEPHYR reconstructs the event variables for both the data and the Monte Carlo in the same way.

The MDST files, like all ZEUS data, are written in ADAMO (Aleph Data Model) [58] format and described in the Data Definition Language(DDL). The ADAMO system is used in the ZEUS reconstruction for the data storage in memory or on external media and for their documentation.

The user can access the data using the EAZE or ORANGE [59] programs. Fig.3.4 shows

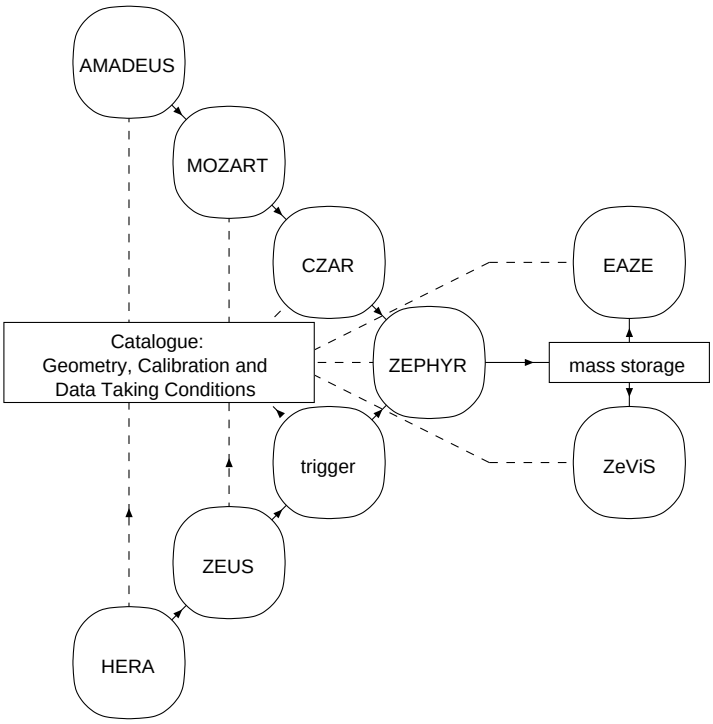

Figure 3.5: A schematic diagram of the ZEUS Data and Monte Carlo reconstruction chain; full lines with arrows indicate the data flow; dashed lines indicate the communication with the catalogue.

a diagram of the ZEUS reconstruction scheme for data and MC.

After processing ZEUS events can be accessed with the ZeViS (ZEUS Visualization) software package. This program allow individual ZEUS events in 2-D and 3-D views of the ZEUS detector to be displayed and also provides some reconstruction information.

[1]For example the data from calorimeters and the position detector as well as the photon and electron bunch currents

Chapter 4

Event Reconstruction and Selection

4.1 Event Reconstruction

For the analysis presented here two sets of data and MC samples were used; one for 35m tagger and the other for 44m tagger. The event reconstruction procedure is almost the same for MC and data except for 44m tagger, where the acceptance of the tagger was calculated separately and added to MC after its simulation. Events collected with the ZEUS detector during 1998 - 2000 were used. The integrated luminosity for the two data samples is discussed in Section 4.2.5.

The aim of this analysis is to measure c-quark production in photoproduction using the open charm channel:

$$e\ p \longrightarrow e\ c\ \bar{c}\ X \tag{4.1}$$

where at least one of the c-quarks decays into a D^* via the reaction:

$$c \longrightarrow D^*\ X \tag{4.2}$$

Each event is hence characterised by the presence of an electron scattered in the dedicated tagger and the decay products of the c-quark.

In this section the reconstruction of the physical quantities needed to characterise a PHP event with heavy quarks in the final state is discussed.

4.1.1 Reconstruction of Kinematic Variables

The kinematics of PHP events are defined by two independent variables, see Chapter 1.2, once the energies of incoming lepton, E_e, and proton, E_p, are known. Usually it is any two from (x, y, Q^2, W). Untagged PHP requires no scattered electron in the main detector. For tagged PHP, which is our case, the electron is measured in a dedicated tagger, for which due to the acceptance and the geometry of the tagger $Q^2 \sim 0$ GeV^2. The other main variable is the hadronic centre-of-mass energy, W. There are several methods of reconstructing the variable W, two of which are discussed below.

4.1.2 Electron Method for the 35m Tagger

The physical quantities measured in the taggers and the ZEUS detector are the energy and the polar angle of the scattered lepton $(E_e^{'}, \theta_e)$ and the four-momentum of the particles belonging to the hadronic final state $(E_h, p_{h,x}, p_{h,y}, p_{h,z})$. The electron taggers (44m and 35m) are able detect electrons within a certain energy range, see Chapter 2.5. The angle of the electron calculated from the geometry of the tagger and the beam magnets. For a given initial lepton energy, E_e, one can write:

$$y_e = 1 - \frac{E_e^{'}}{2E_e}(1 - cos\theta_e), \tag{4.3}$$

$$Q_e^2 = 2E_e E_e^{'}(1 + cos\theta_e). \tag{4.4}$$

The angle of outgoing electron is measured with respect to the proton direction. For this analysis we can use so-called collinear approximation: $Q^2 \longrightarrow 0\,\mathrm{GeV}^2$, $q \longrightarrow yk$ therefore for the PHP region we have:

$$y_e \approx 1 - \frac{E_e^{'}}{E_e}, \tag{4.5}$$

Hence using Equation 1.9 the centre-of-mass energy, W, in tagged PHP can be calculated from the energy of the scattered electron:

$$W^2 \approx sy \approx s(1 - \frac{E_e^{'}}{E_e}). \tag{4.6}$$

This method is called *the electron method*. It is an easy method as it requires the measurement of only one particle. This method is used to calculate the kinematics of events measured with the 35m tagger.

4.1.3 Jacquet-Blondel method for the 44m Tagger

Unfortunately, the 44m tagger provides only information on whether an electron was detected or not. Therefore for the calculation of the kinematics of events tagged with the 44m tagger *the hadron method* is used. This method relies on the hadronic system and does not require information about the scattered electron. In this method, also known as *the Jacquet and Blondel* method [60], y and W can be approximated by

$$\delta_h = \sum_{i=1}^{N_{had}} E_i(1 - cos\theta_i), \tag{4.7}$$

$$y_{JB} = \frac{\sum_h E_i - p_{z,i}}{2E_e}, \tag{4.8}$$

$$W_{JB} = \sqrt{y_{JB}\ s}. \tag{4.9}$$

The sum, δ_h, runs over all final state hadrons. In practice all hadrons can not be reconstructed due to the detector resolution and geometry. However they deposit all their energy in the calorimeter. That is why in practice the sum runs over all calorimeter cells or over all reconstructed objects in the calorimeter.

This method is insensitive to the particles leaving the detector undetected in the forward direction since they contribute very little to δ_h. Particles in the backward direction contribute more to the sum. This method is also sensitive to calorimeter noise at very small y. For the *Jacquet and Blondel* method it is important to measure very accurately the hadronic state information using CAL cells.

4.1.4 Reconstruction of the Hadronic System - ZUFOs

In the case of PHP (both tagged and untagged), all energy deposits in the calorimeter are assumed to belong to the hadronic system. However a better reconstruction of the calorimeter variables can be made by merging calorimeter and tracking system information. For low energy charged particles or when charged particles have to cross a large thickness of dead material

before being detected in the calorimeter, the reconstruction of the particle energy is done better by tracking devices than by calorimeter. Moreover the angular resolution of the CTD for charged particles is better than in the calorimeter, for low energy particles the momentum measurement of the CTD is better than the energy measurement of the calorimeter. There is also the complication concerning the design of the ZEUS calorimeter, which is divided into three parts, FCAL, BCAL and RCAL. This spatial separation is a serious complication for a local clustering algorithm, when a single particle energy is not deposited in a single part of the UCAL. Thus the new technique of merging information from the CTD and the UCAL for the best estimation of the inelasticity, y, and jet has been introduced in ZEUS. The objects calculated by this technique are called *ZUFOs* (Zeus Unidentified Flow Objects) [61].

For ZUFOs the clustering algorithm is done in two steps: first a *cell island* is formed and then based on global clustering a *cone island* is created. The cell island algorithm starts by considering each cell and its local neighbourhood. If the cell has enough energy, it can be connected with one of its neighbours, chosen between the highest energy nearest neighbour and the highest energy next-to-nearest neighbour. The procedure is repeated for each cell so that

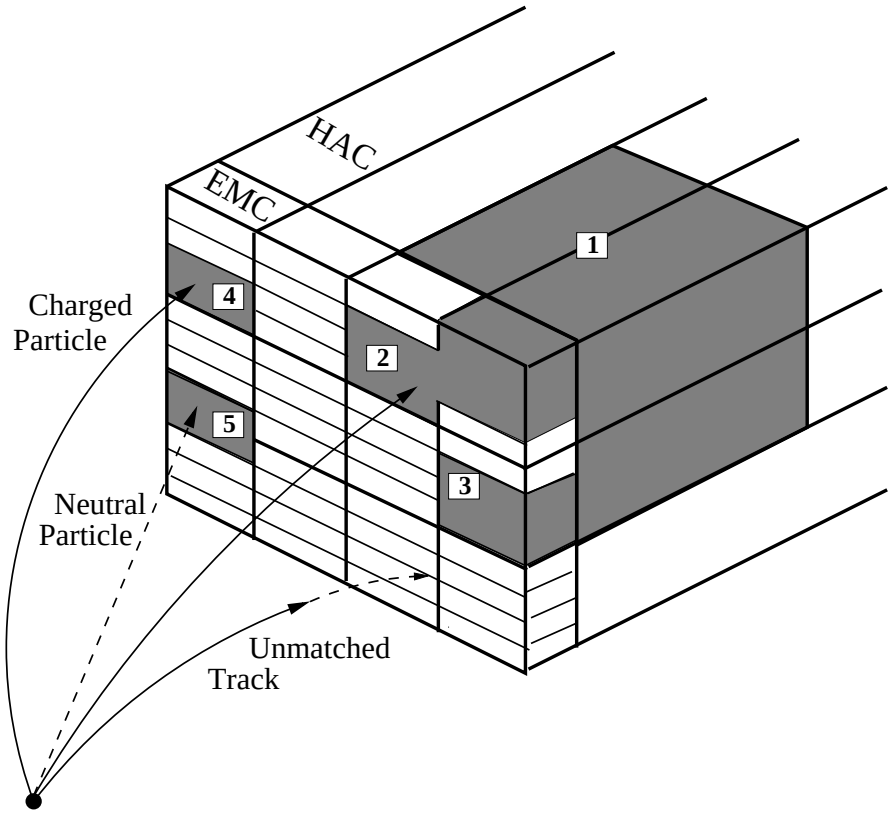

Figure 4.1: Schematic view of the reconstruction procedure with ZUFOs. Neighbouring calorimeter cells are clustered into cell islands. This picture shows four EMC cell islands and one HAC cell island. EMC cell islands 2 and 3 are joined with HAC cell island 1 to form a cone island. Then the cone island is matched to tracks.

at the end each cell is uniquely assigned to an island. The program looks for each cell island in each layer of the calorimeter separately (FEMC, FHAC1, FHAC2, BEMC, BHAC1, BHAC2, REMC, RHAC). Then the cone island algorithm collects the cell islands, which belong to a shower of a single particle or a jet of particles, into cone islands. The matching of cell islands starts from the outermost hadronic layer of the calorimeter and proceeds inward (HAC2 -

HAC1 - EMC). The angular separation between cell islands of different layers is calculated in $\theta - \phi$ space and translated to a probability according to a distribution determined from a single pion MC. The links with highest probability are accepted. After the linking procedure is done, the cone islands are generated by combining all calorimeter cells which point to the same cone island in the electromagnetic layer, for more detail see [61].

After island reconstruction the ZUFOs looks for good charged tracks [62], which are fitted to the primary vertex. These tracks have to pass at least 4 CTD superlayers and have transverse momentum p_T in the range $0.1 < p_T < 20\,\text{GeV}$ (maximum p_T is raised to 25 GeV for tracks passing more than 7 superlayers). The good tracks are extrapolated to the inner surface of the calorimeter and associated to cone islands. They are matched if the distance between the extrapolated track and the island, r_{min}, is less than 20 cm, or if it is less than maximum radius of the island, r_{island} in a plane perpendicular to a ray drawn from the vertex to the island:

$$d \leq max(r_{min}, r_{island}). \tag{4.10}$$

The parameter r_{min} is extracted from a MC simulation by maximising the track-island matching efficiency for single-particle calorimeter clusters. In Fig. 4.1 a schematic view of the whole procedure is shown.

The hadronic centre-of-mass energy, W, for events selected with the 44m tagger is calculated using ZUFOs. In Fig. 4.2 the distributions of $E - P_z$ for the CAL and ZUFOs reconstruction algorithms for the 44m tagger are shown. Comparison of reconstructed and *true* W variable shows that the ZUFOs algorithm has less bias and better resolution than the CAL algorithm.

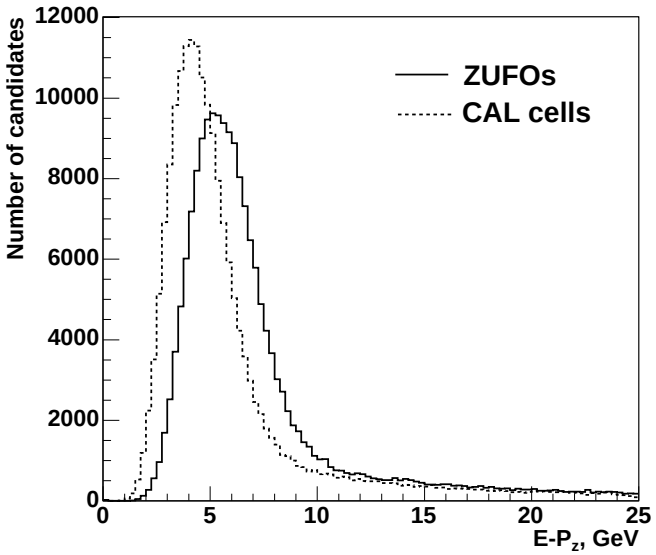

Figure 4.2: Hadronic system information, $E - P_z$, is extracted using different algorithms for the 44m data sample. The line represent the reconstructed by ZUFOs algorithm, while the dashed line represent the reconstructed by CAL.

4.1.5 Track Reconstruction in the CTD

ZEUS uses the VCTRACK package [63, 64] for charged particle track reconstruction. This package runs during the offline data reconstruction phase and also participates in an optimised

form in the TLT (Third Level Trigger). It uses the hit information from CTD, FTD, RTD and SRTD.

There are two different modes in the reconstruction package, *regular* tracking and $CTD-only$ tracking. In first case during reconstruction information from all the detectors is used, whereas $CTD-only$ tracking considers hit information only from the CTD. In this analysis for charged track reconstruction the $CTD-only$ tracking is used.

The CTD is able to measure hits (space points) along the path of a charged particle, where their X and Y components are reconstructed from the signal on the wires induced by a passing particle. Using the timing information of hits in the CTD the distance from sense wire can be found. For those wires read out at both ends, see Sec. 2.3, the two different times at the front, t_{front}, and the rear,t_{rear} , end are given by:

$$t_{front} = t_0 + t_{flight} + t_{drift} + t_{wire,front} \tag{4.11}$$

$$t_{rear} = t_0 + t_{flight} + t_{drift} + t_{wire,rear}, \tag{4.12}$$

where t_0 is the interaction time of the event and is given by the HERA machine, t_{flight} is the flight time of the particle from the IP to the point when the electron avalanche is started in CTD due to the interaction of particle with the gas, t_{drift} is the drift time of the electrons to the sense wire and $t_{wire,front}$ ($t_{wire,rear}$) is the time which an induced signal needs to reach the front (rear) end. The velocity of the electron avalanche produced by a charged particle in the gas mixture is known. The velocity of the signal along the wires is also known. Thus, using the timing information of a hit one can calculate the point where the electron cascade was started by the particle, that is the distance from the sense wire, but not the direction. Therefore each hit has a $ghost-hit$, which has the same z component, but is located on the other side of the sense wire, see Fig. 4.3.

The hits from CTD are combined into tracks starting from the outermost superlayer, superlayer number nine. A minimum of three hits in the same cell are combined into *a track seed*, which is linked to the IP $X = Y = 0$. Then tracks are extrapolated towards the vertex. This

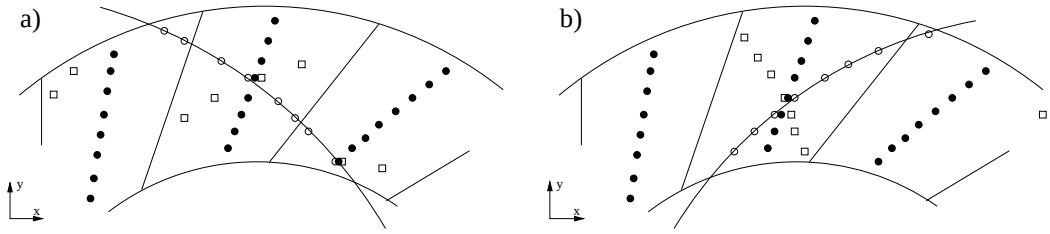

Figure 4.3: The CTD cells with a track of a charged particle and the calculated positions of the hits. The solid circles represent the sense wires in a CTD cell. The open circles and the open squares are possible hit positions of a track. Open circles indicate the selected positions after the combination of track fragments in different cells. The track shown in plot *a*) is produced by a particle with negative charge, the one on the *b*) is produced by a particle with positive charge.

procedure continues for tracks originating in each axial superlayer in turn. The z component is reconstructed using hits in the stereo layers and the z by timing information (see Section 2.3). Hits from stereo layers used to improve the track resolution.

The VCTRACK package tries also to reconstruct a vertex for the event. For that each track which is assigned to the vertex is recalculated including information about the vertex

position (VCTPAR tracks). The most compatible vertex is the one which has the lowest χ^2. Unfortunately for 1998-2000 data the resolution of the ZEUS tracking and vertex finding is not sufficient to enable the identification of secondary vertices arising from the decay of D^* mesons. That is why only primary vertexed tracks are used for this analysis.

4.2 Trigger Selection

All events have to pass a three level trigger selection in order to cut background and non-interesting events. A sketch of the ZEUS HFL tagged photoproduction trigger is shown on Fig. 4.4.

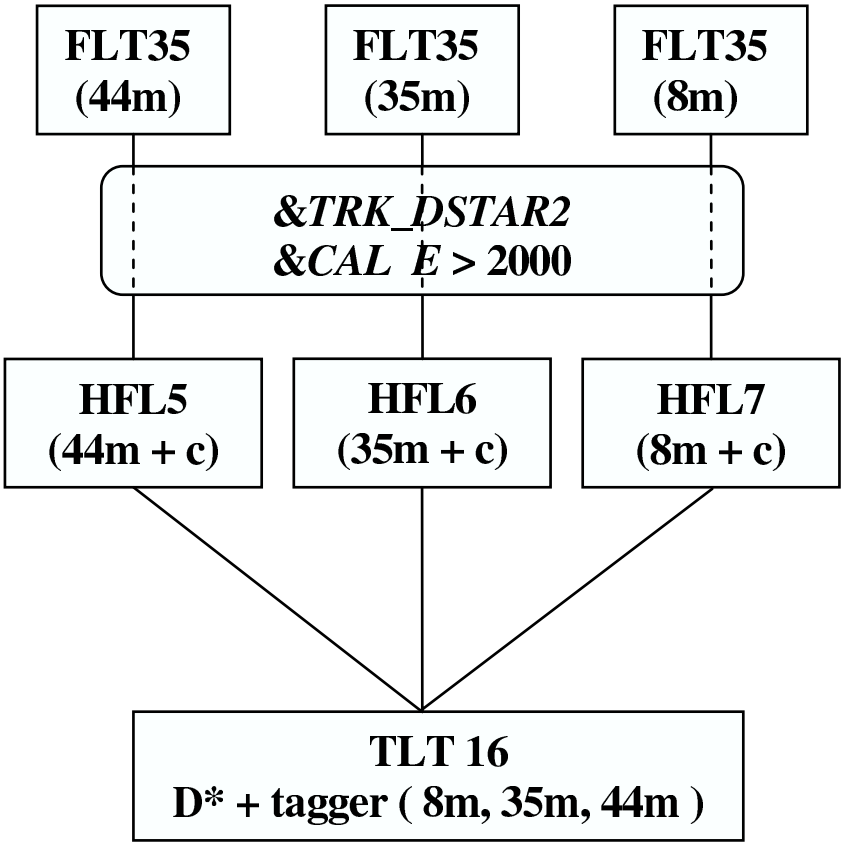

Figure 4.4: An overview of the ZEUS HFL triggers for the 8m, 35m and 44m taggers as implemented in the 1998 - 2000 running period.

Each event has to fulfil a positive trigger decision at each trigger level, which means that at least one of the 50 - 250 boolean variables, which are also called "trigger bits", per trigger level is "true". The trigger chain consists of FLT (First Level Trigger), SLT (Second Level Trigger) and TLT (Third Level Trigger). The FLT and SLT are different for the 35m and 44m taggers, but the TLT is the same.

4.2.1 First Level Trigger

The first level trigger requires some activity in the tracking system and an electron detected in the tagger. Tracking just takes into account the hits in the axial superlayers of the CTD. There must also be some energy deposited in the CAL cells.

44m tagger - HFL-FLT 35. For the 44m tagger FLT slot 35 was used. This requires the following conditions:

- an electron detected in the 44m tagger (by LUMI_Cherenkov_veto);
- at least one good FLT track which comes from the nominal interaction point;
- an energy deposit in the CAL (flt_cal_e) and/or energy in RCAL EMC section (flt_remc_e), two different thresholds for CAL energy were used, for more information see Section 4.2.5.
- E_{LUMI_γ}, which is the energy deposited in the photon calorimeter less than a threshold, which still allows ISR events to be kept. ISR events are those in which the electron radiates a photon before interacting;
- $E_{LUMI_e} < 5\,\text{GeV}$, which is the energy deposited in the lumi detector (35m tagger);
- the event timing has to be consistent with the timing for a physics event. Events where the timing information, measured by VETO, C5 counter and SRTD, is consistent with the reaction having taken place outside of the ZEUS interaction region are vetoed.

35m tagger - HFL-FLT36. For the 35m tagger FLT slot 36 was used. Like FLT 35 this trigger also requires some activity in the tracking system and the CAL.

- an energy detected in the 35m tagger, $E_{LUMI_e} > 5\,\text{GeV}$;
- at least one good FLT track which comes from the nominal interaction point;
- an energy deposit in the CAL (flt_cal_e) and energy in RCAL EMC section (flt_remc_e);
- E_{LUMI_γ}, which is the energy deposited in the photon calorimeter less than a threshold, which still allows ISR events to be kept. ISR events are those in which the electron radiates a photon before interacting;
- the event timing has to be consistent with the timing for a physics event.

4.2.2 Second Level Trigger

The requirements on SLT include the FLT bit described above. Simple tracking is done. The selection cuts are similar to those in the offline selection but with looser thresholds. The quantity $\delta_i = E - P_z$ is introduced, defined as the difference between the total energy and longitudinal component of the momentum. For the incoming particles $\delta_i = \delta_{proton} + \delta_{electron} = 920\,\text{GeV} + 27.5\,\text{GeV} - (920\,\text{GeV} - 27.5\,\text{GeV}) = 55\,\text{GeV}$. The value measured for the particles detected in the event, δ_f, is defined as $\delta_f = \sum_{i=1}^{N} E_i(1 - cos\theta_i)$, where the index i runs over all CAL cells, each one characterised by a measured energy, E_i, and polar angle, θ_i. This $E - p_z$ definition neglects the particle's masses. Relatively soft cuts for $p_T(K)$, $p_T(\pi)$ and $p_T(D^*)$ are used. The cuts are chosen in a way which allows more than 60% of the D^* events, which can be reconstructed in the offline reconstruction, to pass this level while keeping the trigger rate at a tolerable level. At this level the interesting events have to fulfil the following conditions:

44m tagger - SLT-HFL5. For the 44m tagger HFL5 is used which includes following conditions:

- HFL-FLT35.

- An *ep*-vertex reconstruction.
- $E - P_z < 25\,\text{GeV}$.
- The transverse calorimeter energy $E_T > 4\,\text{GeV}$, excluding the inner two rings of FCAL.
- Number of vertex tracks $\geq$2 and number of found tracks $\geq$5.
- Number of found tracks $\geq$ 16 or the sum of two highest p_t tracks $> 1.2\,\text{GeV}$.

35m tagger - SLT-HFL6. For the 35m tagger HFL6 is used which includes the following conditions:

- HFL-FLT36.
- An *ep*-vertex reconstruction.
- $E - P_z > 6\,\text{GeV}$.
- $E_T > 6$, excluding the inner two rings of FCAL
- Number of vertex tracks $\geq$3 and number of found tracks $\geq$5.
- Number of found tracks $\geq$ 16 or the sum of two highest p_t tracks $> 1.2\,\text{GeV}$.

The different cuts on $E - p_z$ are due to the different event topologies. The hadronic system in the 44m tagger events tends to go forward, while the one in the 35m events tends to go backwards (see Fig. 5.2 and 5.1).

4.2.3 Third Level Trigger

This level requires one of the SLT bits described above and TLT-HFL16, which consists of HFL-TLT10 ($D^* \longrightarrow K\pi\pi$), HFL-TLT11 ($D^* \longrightarrow K\pi\pi\pi\pi$), HFL-TLT12 ($D^0 \longrightarrow K\pi$). Here the kinematics of the events is fully determined and the reconstructed tracks are close to the final ones. Based upon on those tracks a complete D^* reconstruction is performed. The event has to fulfil following conditions for HFL-TLT10 ($D^* \longrightarrow K\pi\pi$):

- The CTD vertex -50 cm $< Z_{vtx} <$ 50 cm and 2 $<$ number of CTD tracks $<$100.
- $p_T(\pi_s) > 0.1\,\text{GeV}$ and $p_T(D^*) > 1.5\,\text{GeV}$.
- $p_T(K, \pi \text{ of } D^0) > 0.35\,\text{GeV}$.
- The tracks must traverse at least the first 3 superleyers of the CTD.
- $1.4 < M(D^0) < 2.2\,\text{GeV}$
- $\Delta M < 0.170\,\text{GeV}$, where $\Delta M = M_{K\pi\pi_s} - M_{K\pi}$
- The charge of the tracks is not taken into account in the selection.

4.2.4 Tagged Charm Trigger (DST92)

The preselection of the data was done using DST bit 92 which merely selects events passing TLT bit 16. After this preselection a total 5877954 events for the 44m, 339680 events for the 35m, 387114 events for the 8m tagger respectively were accepted and written to ntuples.

4.2.5 Luminosity Calculation for the Different Triggers

The luminosity has been measured by a detector placed 107 m downstream from the interaction point using the process $ep \longrightarrow ep\gamma$, see Section 2.5.3. During the 1998 - 2000 running period there were mainly two different trigger types for the data, so-called low-lumi and high-lumi configurations. They differ by the cut on the energy deposited in the CAL cells, flt_cal_e. For the high-lumi configuration $flt\_cal\_e > 3992$ and for low-lumi - $flt\_cal\_e > 2032$. For 44m tagger triggers both triggers thresholds were used. The MC is generated only with the low-lumi configuration. Therefore the effect of the different trigger configurations is implemented in the MC by introducing a new variable

$$\text{weight}_{lumi} = \frac{\sum \text{lumi}_{low}}{\sum \text{lumi}_{low} + \sum \text{lumi}_{high}} = 0.412, \tag{4.13}$$

Events with $flt\_cal\_e \leq 3992$ are given a weight $weight_{lumi}$. For 35m tagger triggers only the high-lumi threshold was used, so there is no need to do a reweighting for the 35m MC sample. The luminosity used for 44m tagger data sample is 81.5 pb^{-1}, and for 35m tagger 80.7 pb^{-1}. A complete list of the luminosity is shown in Table 4.1. At the end of 2000 the 35m tagger was not operational for a few runs.

Run Range	Running Period	lumi_{low} (44m tagger)	lumi_{high} (44m tagger)	Integrated Luminosity (35m tagger)	Integrated Luminosity (44m tagger)
30764 - 31752	1998e^-	0.9 pb^{-1}	2.635 pb^{-1}	3.548 pb^{-1}	3.548 pb^{-1}
31784 - 32906	1999e^-	6.7 pb^{-1}	5.423 pb^{-1}	12.078 pb^{-1}	12.078 pb^{-1}
33125 - 34486	1999e^+	8.4 pb^{-1}	11245 pb^{-1}	19.657 pb^{-1}	19.657 pb^{-1}
35031 - 37715	2000e^+	17.6 pb^{-1}	28.620 pb^{-1}	45.405 pb^{-1}	46.220 pb^{-1}
Total	1998-2000	33.6 pb^{-1}	47.902 pb^{-1}	80.689 pb^{-1}	81.505 pb^{-1}

Table 4.1: Luminosities and run ranges used in D* production analysis with the 44m and 35m taggers.

4.3 Offline Selection

The ORANGE (Overlying Routine for Analysis Ntuple GEneration) software package [59] is used to preselect the events and to create ntuples with the variables needed for this analysis. In this package the preselection of events is done with control cards, where the user can switch on the option of interesting reconstruction variables. One can also put there limits for those variables.

4.3.1 Selection of photoproduction events

As was discussed earlier (see Section 4.1), photoproduction is characterised by very small Q^2. Selection of such events has been performed by tagging an electron in the dedicated taggers, whose location already specifies the PHP kinematics. The following cuts were used to select PHP events:

- -50 cm $< z_{vtx} <$ 50 cm

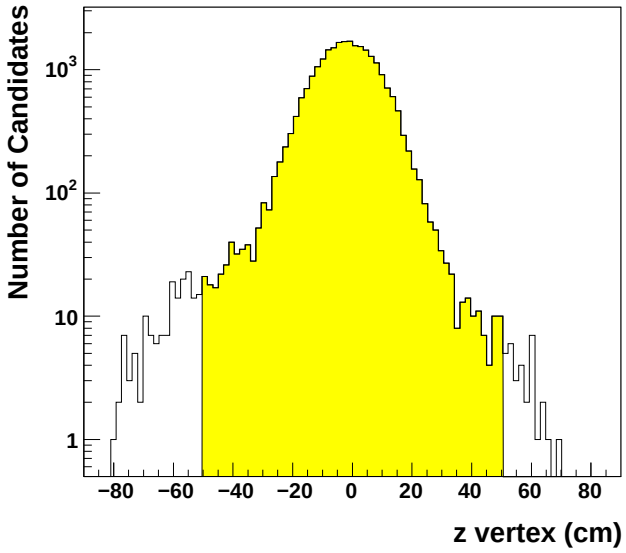

Figure 4.5: $Z-$vertex distribution of data. All analysis cuts except z_{vtx} cut are applied.

This cut on the Z-vertex is made in order to reject non-physics background such as proton beam-gas interactions or cosmic events. The Z_{vtx} distribution for the data sample using the 44m tagger is shown in Fig. 4.5.

- The geometry, position and acceptance of the taggers give the accessible kinematic region. Due to them and the magnetic field only the electrons scattered with $E_e^{'} > 21$ GeV (5 GeV) can be measured in the 44m (35m) tagger, see Fig. 4.6. The procedure to extract the acceptances for the 44m and 35m taggers is explained in Sections. 4.4 and Section 4.5. According to formulae 4.6 and 4.9 we have the following W ranges, where the efficiency is more than 80%:

  80 GeV $< W <$ 120 GeV for the 44m tagger, reconstructed using the Jacquet-Blondel method,

  200 GeV $< W <$ 260 GeV for the 35m tagger, reconstructed using the electron method,

4.3.2 D* Reconstruction

In this analysis charm events are identified by reconstructing $D^{*\pm}$ mesons in the final state. D^* mesons are reconstructed using the following decay mode, which is called the *golden channel* in ZEUS:

$$D^{*+} \longrightarrow D^0\pi_s^+ \longrightarrow K^-\pi^+\pi_s^+ + c.c. \tag{4.14}$$

According to the Particle Data Group [65], the branching ratios of these decay modes are:

$$BR(D^{*+} \longrightarrow D^0\pi_s^+) = 67.7 \pm 0.5\%, \tag{4.15}$$

$$BR(D^0 \longrightarrow K^-\pi^+\pi_s^+) = 3.80 \pm 0.09\%, \tag{4.16}$$

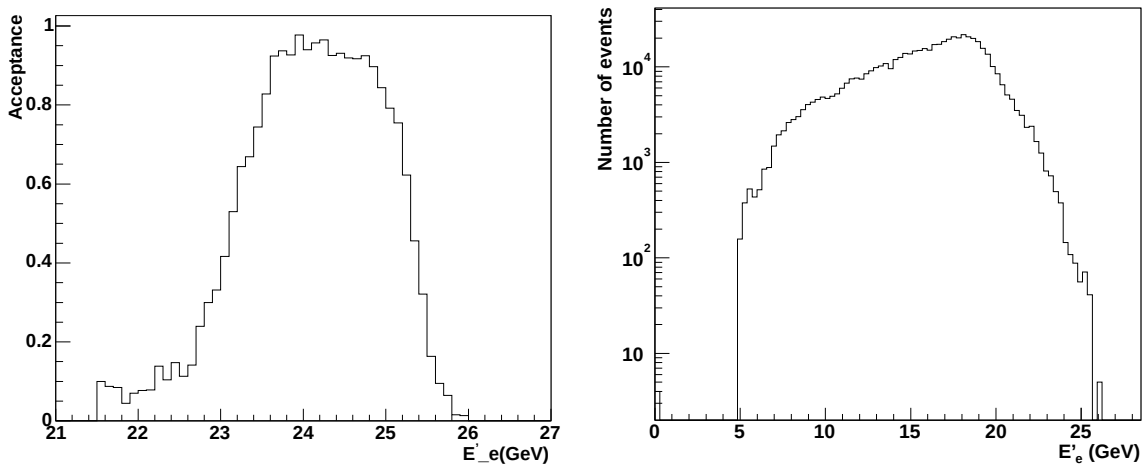

Figure 4.6: Acceptance of the electron taggers as a function of the electron energy. The left plot represents the 44m tagger acceptance. The right plot is the energy distribution of scattered electron reconstructed in 35 tagger acceptance.

so the full branching ratio of $D^{*\pm} \longrightarrow K^{\mp}\pi^{\pm}\pi_s^{\pm}$ decay is 2.57%. The probability for a charm quark to fragment into a $D^{*\pm}$ meson [66] is:

$$f(c \longrightarrow D^{*\pm}) = 20 \pm 0.9(stat)^{+0.8}_{-0.6}(syst)^{+0.8}_{-1.2}(br)\ \%, \tag{4.17}$$

The method has advantages and disadvantages. The disadvantage is the small branching ratio. The advantage is that the all the decay products are charged particles. In order to reconstruct the D^* invariant mass, one needs a precise measurement of the K, π, π_s momenta. That is achieved by the CTD with good resolution. The pion emitted from the $D^{*\pm}$ decay has a small momentum in the D^* rest frame and is called *the slow pion*. In order to distinguish it from the pion from D^0 decay it is denoted as π_s. The other advantage of this method is that this decay mode requires two mass reconstructions, the mass of the D^0 and the mass difference of D^* and D^0:

$$\Delta M = m(K\pi\pi_s) - m(K\pi). \tag{4.18}$$

The four-vectors of kaon and pion from the D^0 decay are used twice in calculation of ΔM, once for calculation of D^0 mass and once for calculation of D^* mass, and thus their errors cancel in the difference. Therefore the reconstruction error of ΔM mainly depends on the error of the π_s four-vector. Due to the multiplicity of tracks the combinatoric background in the D^0 mass distribution is high. Nevertheless, since the D^* and D^0 mass difference is only 145 MeV, ΔM from equation 4.18 is very small and just a bit more than the pion mass (139.5 MeV), the background from different combinations of kaons and pions can be significantly reduced by cutting on the reconstructed D_0 mass and ΔM mass. The background can be estimated using the D^* candidates coming from wrong charge combinations, see also Section 4.3.3 and Table 4.2 for the subtraction method.

4.3.3 Cuts

Due to the short lifetime of the D^* meson the vertices produced by the D^0 meson decay are very close to the primary vertex. Unfortunately the resolution of the tracking system is not sufficient to reconstruct them separately from the primary vertex. That is why the all reconstructed D^* mesons tracks should come from the same primary vertex. Each track should

Sign of Charge			Type	Treatment in the Analysis
K	π	π_s		
+	+	-	WC	D^{*+} background
+	-	-	RC	D^{*-} signal
-	+	+	RC	D^{*+} signal
-	-	+	WC	D^{*-} background

Table 4.2: The charge combinations of CTD tracks to build a D^* candidate. RC is the rights charge combination and WC is the wrong one. For right charge combinations the π_s should always carry the sign of D^*.

also traverse at least three CTD superlayers, therefore the pseudorapidity of tracks should be $|\eta(track)| < 1.75$, where θ is the azimuth of the tracking particle.

As can be seen from equation 4.14 for D^* reconstruction three charge tracks are needed. The transverse momenta of charged particles with opposite charges coming from D^0 decay should be more than 0.4 GeV/c. The ZEUS detector cannot reliably distinguish charged kaons from pions over most of the momentum region relevant for this analysis [1], that is why for the invariant mass calculation the charged particles are treated equally with opposite charges and combined to form D^0 candidate. After that the momentum of the next charged track, which is assigned to be the slow pion, is required to be more than 0.12 GeV/c and with an opposite charge to the kaon candidate. In this way the selected D^* candidate tracks have the following cuts:

- $|\eta(K, \pi, \pi_s)| < 1.75$
- $p_\perp(K),\ p_\perp(\pi)\ > 0.4$ GeV/c, to provide a good ratio of signal to noise for tracks from the D^0 meson decay
- $p_\perp(\pi_s)\ > 0.12$ GeV/c, to provide reliable track measurement in the CTD

By limiting η and $p_\perp$ for the tracks we are making in principal a limit also on $\eta(D^*)$ and $p_\perp(D^*)$, because decay products are boosted in the direction of the charm quark. The following cuts on $p_\perp$ and η of D^* meson are applied:

- $-1.0 <\ \eta(D^*)\ < 1.5$ for the 44m tagger
  $-1.5 <\ \eta(D^*)\ < 1.0$ for the 35m tagger
- $p_\perp(D^*) > 1.5$ GeV for the 44m tagger
  $p_\perp(D^*) > 2.0$ GeV for the 35m tagger
  The reconstructed mass ranges for ΔM and M_{D^0} are defined in the following mass windows:
- 0.143 GeV$<\ \Delta M\ <$ 0.148 GeV
- 1.81 GeV$<\ M(D^0)\ <$ 1.92 GeV

In Fig. 5.1 and 5.2 (bottom plots) the transverse momentum and pseudorapidity distribution of the D^* candidates for both taggers are shown and compared to MC. For all the

[1] With the CTD kaons and pions can be distinguished using the dE/dx information for momenta up to ~1 GeV.

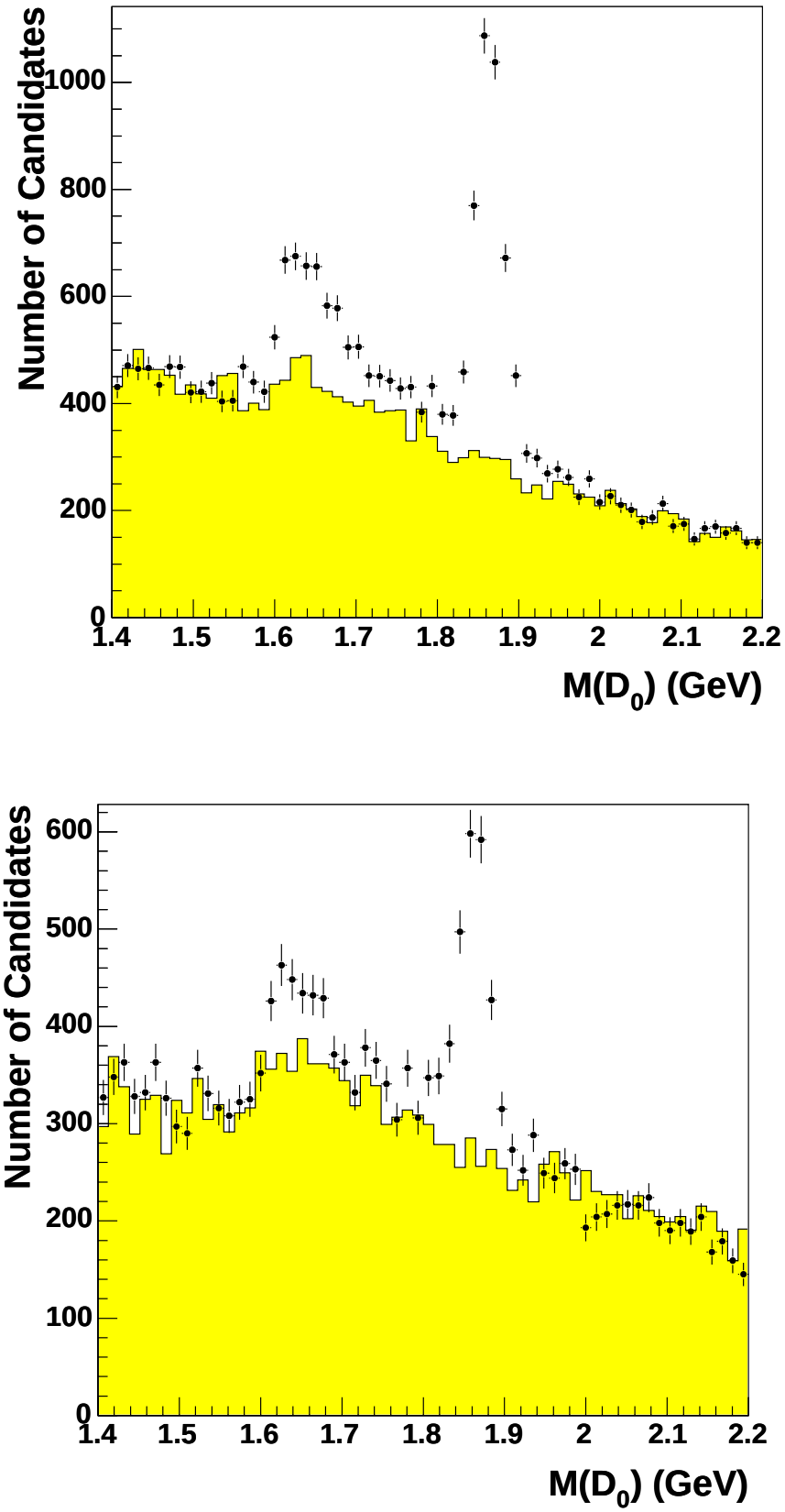

Figure 4.7: $M(D_0)$ distribution for events with an electron in the 44m (upper plot) and in the 35m (lower plot) taggers. The point show the distribution for candidates with the right charge combination and the histogram shows the wrong charge combination background.

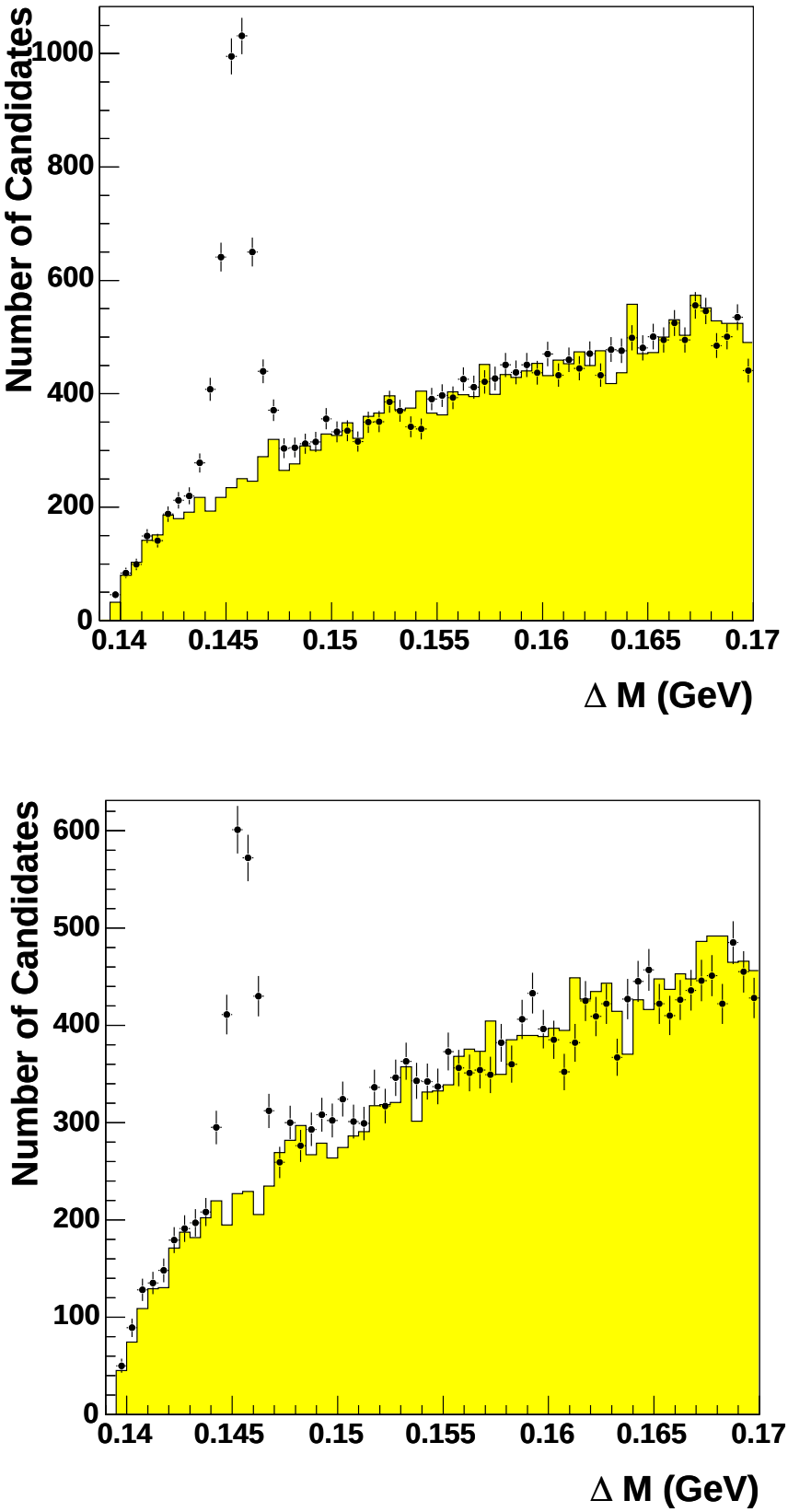

Figure 4.8: ΔM distribution for events with an electron in 44m (upper plot) and 35m (lower plot) taggers. The point show the distribution for candidates with the right charge combination and the histogram shows the wrong charge combination background.

distributions all analysis cuts are applied. Comparison shows good agreement between data and MC. As you can see from $\eta(D^*)$ distributions. for 44m tagger sample the D^* are mainly produced in the forward region, while for the 35m tagger sample they tend to go in the backward direction. The ΔM and $M(D_0)$ distributions for each tagger are shown in Fig. 4.7 and 4.8. In those distributions all cuts except the ΔM or D^0 cut respectively are applied. A clear excess of right charge combinations with respect to combinatorical background estimates is observed for masses below of that D^0 signal (Fig. 4.7). This excess is due mainly to events in which a D^0 decays into $K\pi\pi^0$, and the extra π^0 has not been included into the D^0 invariant mass reconstruction [67].

4.3.4 Signal Extraction

For signal extraction the *wrong charge combination* method is used. In this analysis the measurements of D^{*+} and D^{*-} mesons are done together. In this case the ΔM distribution of wrong charge combinations is subtracted from the ΔM distribution of right charge combinations using a normalisation factor obtained from a control region.

The ΔM distributions both for the correct charge combination and for the wrong charge combination are divided into mass windows, see Fig. 4.9. The regions A and C represent the mass windows of D^* candidates for correct charge and wrong charge combinations respectively, where we expect the signal. The B and D regions are chosen in order to normalise the background distribution (C) to the signal (A) for correct subtraction and are called *control areas*. Thus the number of events and its error are calculated as:

$$N_{events} = N(A) - N(C)\frac{N(B)}{N(D)} \tag{4.19}$$

$$\sigma_N = \sqrt{N(A) + N(C)N(B)\frac{N(C) + N(B) + N(C)\frac{N(B)}{N(D)}}{N(D)^2}} \tag{4.20}$$

A (C) is evaluated in the range $0.143 < \Delta M < 0.148$ GeV and B (D) is evaluated in the range $0.151 < \Delta M < 0.165$ GeV. The ratio:

$$R = \frac{N(B)}{N(D)}, \tag{4.21}$$

represents the normalisation factor. This factor varies between 0.9 - 1.3 depending on the bin.

This method is used for the cross-section calculation in every kinematic range considered below. In each range the normalisation factor is calculated separately and used to extract the number of D^* candidates. In Fig. 4.10 the subtracted signal is shown for the 35m data sample, where the signal is fitted by a modified function [68]. The number of signal events can also be obtained by fitting the ΔM distribution with a signal + background. This method is very useful in case of low statistics. For this analysis there is a large statistic, so the wrong charge background method is used to extract the D^* signal.

The total number of D^* candidates after all cuts for the 44m and 35m taggers obtained from wrong charge background subtraction are:

$$N_{D^*,44m} = 2953 \pm 97, \tag{4.22}$$

$$N_{D^*,35m} = 1338 \pm 94. \tag{4.23}$$

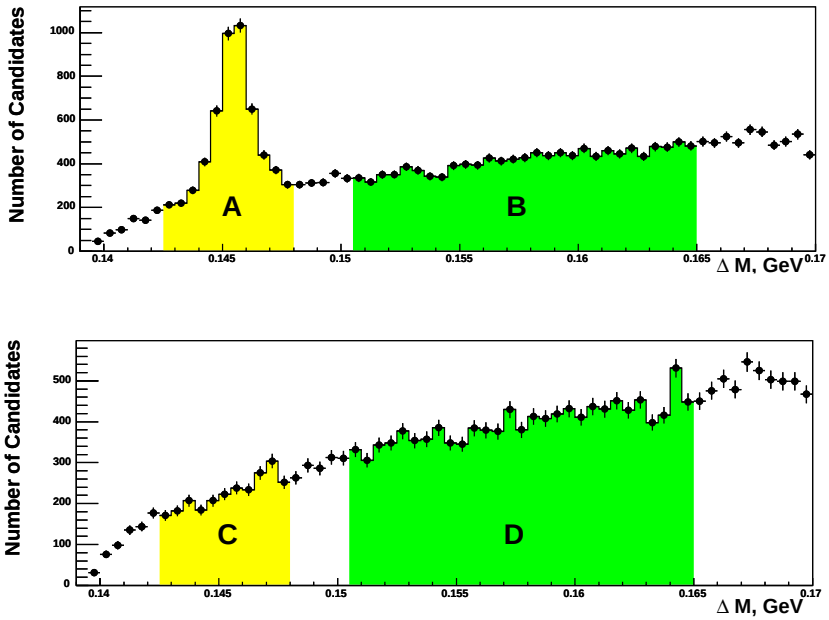

Figure 4.9: D^* right charge selection is shown (top histogram) and wrong charge distribution (bottom histogram) for events with an electron in 35m. Both separated into example signal regions A and C : $0.143 < \Delta M < 0.148\,\text{GeV}$, and background normalisation regions B and D : $0.151 < \Delta M < 0.165\,\text{GeV}$.

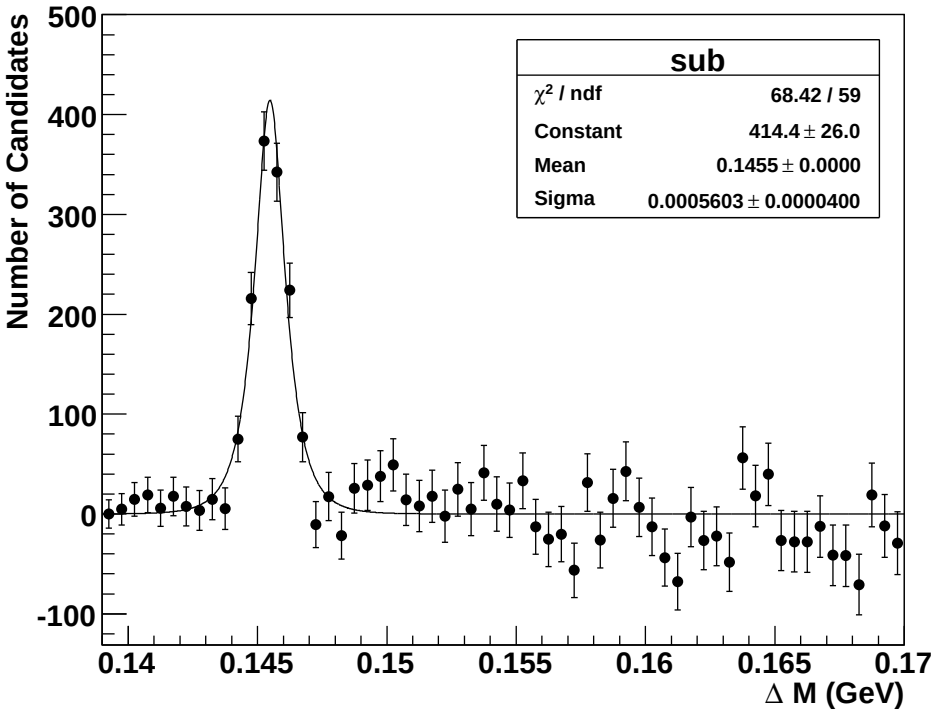

Figure 4.10: The subtracted ΔM distribution for events with an electron in 35m.

4.4 Acceptance of the 44m Tagger

The 44m tagger acceptance is not included in the detector simulation program. Therefore it is calculated separately, using the bremsstrahlung data, and added to the MC afterwards. A 44m tagger trigger is fired if an electron deposits energy more then 1 GeV in the tagger. The procedure to simulate the 44m tagger acceptance consists of two steps.

First, the bremsstrahlung process, $ep \longrightarrow e'\gamma p$, is studied using real data. Second, bremsstrahlung events are generated with the Monte Carlo and passed through a program, which simulate the beam optics from the interaction point to the 44m tagger. Then the simulated distribution of the acceptance of the 44m tagger is extracted by smearing the beam parameters until the simulated acceptance reproduces the shape of that in data.

The bremsstrahlung photons are detected in the photon detector (LUMI-γ detector), which is placed 107m away from interaction point, and the electrons (or positrons) are detected in the 44m tagger. A sketch of the tagging procedure is shown in Fig. 4.11. Two distributions are observed: one is a photon energy distribution in LUMI-γ and the second is an electron

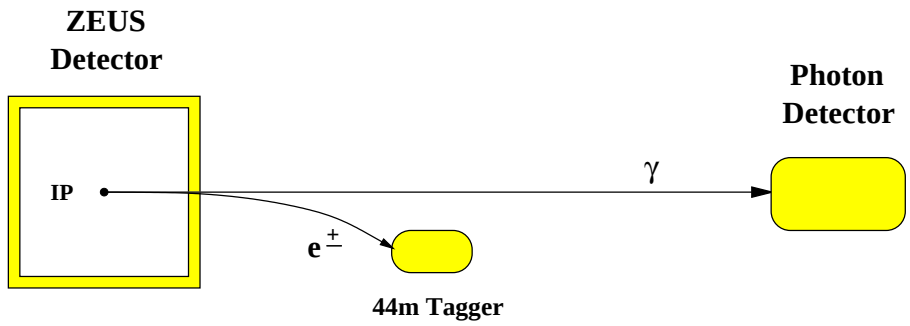

Figure 4.11: Sketch of the tagging system for the photon and electron/positron scattered under small angle.

energy distribution in 44m tagger, when also a photon was observed in the photon calorimeter. The acceptance of the 44m tagger is defined as a ratio of the events with a coincidence of the electrons in the tagger and the photons in the LUMI-γ detector to all events in the LUMI-γ detector. Unfortunately the energy resolution of scattered electron in the 44m tagger is very poor and cannot be used for acceptance calculation. The tagger is used only for tagging the electrons. Therefore the acceptance of tagger was studied as a function of radiated photon energy and then, the electron energy, E', was extracted from the incoming electron beam energy, E_e, and the radiated photon energy in $LUMI_\gamma$ detector, E_γ, using the relation[2]:

$$E' = E_e - E_\gamma. \tag{4.24}$$

The procedure of the geometrical acceptance calculation of the photon detector is described in [69]. The photon energy in $LUMI_\gamma$ detector is measured in ADC channels and then transformed into GeV. The average response of the photon detector is well described above a photon energy of 1 GeV by linear function with a small quadratic non-linear term. There is also a relative deviation from a linear behaviour of about 7x10^{-4} GeV[1] created by the readout electronics. Therefore the following parameterisation of the average detector response is used for getting photon energy spectrum in GeV, $\overline{ADC_\gamma}$, as a function of the *true* photon energy, E_γ:

$$\overline{ADC_\gamma} = c_\gamma[1 + f_{nl}(E_e - E_\gamma)](E_\gamma - E_{filter}) + ADC_\gamma^{ped}, \tag{4.25}$$

[2]The energy exchanged between the primary electron and proton is very small, of the order of m_e^2/m_p.

where c_γ is a conversion constant from GeV to ADC counts (sensitive to the overall gain), f_{nl} is a global non-linear parameter, and E_{filter} is a parameter accounting for the energy loss in the carbon filter of the $LUMI_\gamma$ detector. The fluctuation of the response function is modelled by a Gaussian smearing of the energy deposition in the calorimeter due to the sampling fluctuations, $\Delta E/E = \sigma_0/\sqrt{E_\gamma(\,\mathrm{GeV})}$.

The parameters $c_\gamma, f_{nl}, E_{filter}$ and σ_0 are obtained from the fits to the data and their values vary between years 1998 and 2000.

In Fig. 4.12 the bremsstrahlung photon energy spectrum in the $LUMI_\gamma$ detector for a single run is shown in units of the ADC counts. The upper plot shows the photon energy distribution for all events and for events tagged in the 44m tagger, while in the lower plots the acceptance, A_B, of 44m tagger as a function of ADC channels is shown.

The right tail in the acceptance distribution results from multiple bremsstrahlung scattering and indicates the amount of multiple events. The fraction of such events depends on the beam rate.

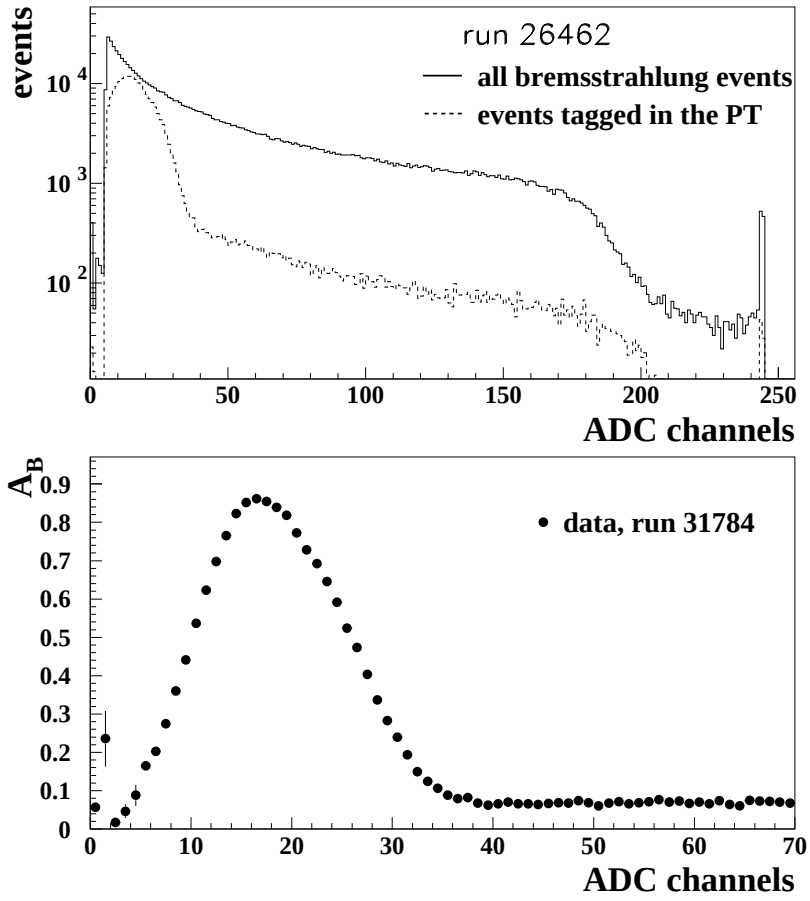

Figure 4.12: The bremsstrahlung photon energy distribution in the $LUMI_\gamma$ detector as a function of ADC counts for all events (solid histogram, upper plot) and for events tagged in the 44m tagger (dashed histogram, upper plot), together with the tagging efficiency (dots, lower plot).

During passing the beam line optics the scattered electron changes direction due to dipole and quadrupole magnets and triggers an event only when it hits the 44m tagger. The main

variables determining the direction and the path of the electron are the scattering angle, θ_e, energy, E'_e, and the interaction vertex distribution. For the acceptance of 44m tagger due to the beam optics the important parameter is only the x position of the vertex, v_x, the y and z vertex position, v_y, v_z, does not change the efficiency much. The three features of the trigger efficiency A_B shape were studied in [70] run-by-run for the 96-97 data: a maximal acceptance, A_{max}, a width of the A_B distribution A_w and an energy E_{max} which corresponds to A_{max}. The studies show that A_{max} and A_w are constant as a function of the run number and are independent of the vertex, while E_{max} varies strongly with the run number and is correlated with the distribution of v_x. Hence the v_x distribution plays an important role in the 44m tagger acceptance shape. That is why big attention was payed to its reproduction in the MC for evaluating the final acceptance.

The second step is to study the *ep* bremsstrahlung events generated by the MC program. This was done using the BREMGE MC generator [71]. The Monte Carlo program also simulates the detector response assuming the nominal values of the parameters $\sigma_0, E_{filter}, f_{fnl}$ and c_γ. Then these events were passed through the program which simulates the beam optics in ZEUS from the interaction point (IP) to the 44m tagger. v_y and v_z were set to the zero because they do not influence on the 44m tagger acceptance. All the other parameters, for example v_x, position and geometry of the tagger, the number of the of multiple bremsstrahlung events and spatial resolution of the beam were tuned to give the best description of the data using the runs which have the large statistics in the running period.

In the Fig. 4.13 the acceptance of the 44m tagger is shown as a function of the collision energy W. The average acceptance range is $80 < W < 120$ GeV.

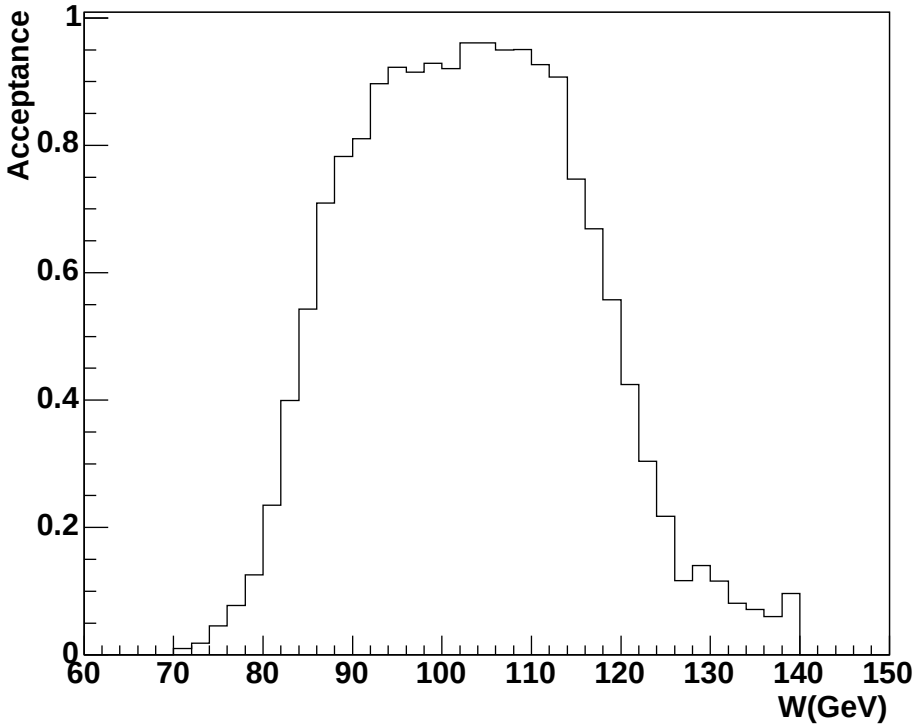

Figure 4.13: The acceptance of the 44m tagger as a function of the hadronic centre-of-mass energy, W.

4.5 Acceptance of the 35m Tagger

The simulation of the 35m tagger acceptance is already built in the ZEUS detector simulation program. The procedure used to simulate the 35m tagger acceptance is similar to that defined for the 44m tagger. The BREMGE MC generator was used to determine the acceptance of tagger. The parameters of incoming positron beam used in the generator were determined using the bremsstrahlung data. In contrast to the 44m tagger, the 35m tagger has good energy resolution, therefore the energy of scattered electron detected in the 35m tagger, $E_e^{'}$, was used for the acceptance calculation. In this case the 35m tagger acceptance was defined as the ratio of events containing an electron with $E_e^{'} > 5$ GeV in the tagger and a photon with energy $E_\gamma > 5$ GeV in the $LUMI_\gamma$ detector to all events containing a photon with energy $E_e^{'} > 5$ GeV in the $LUMI_\gamma$ detector. The energy of the scattered electron is reliable in the range $9 < E_e^{'} < 16.6$ GeV, which corresponds to the collision energy range $200 < W < 260$ GeV. Fig. 4.14 shows the 35m tagger acceptance efficiency as a function of Q^2 and W.

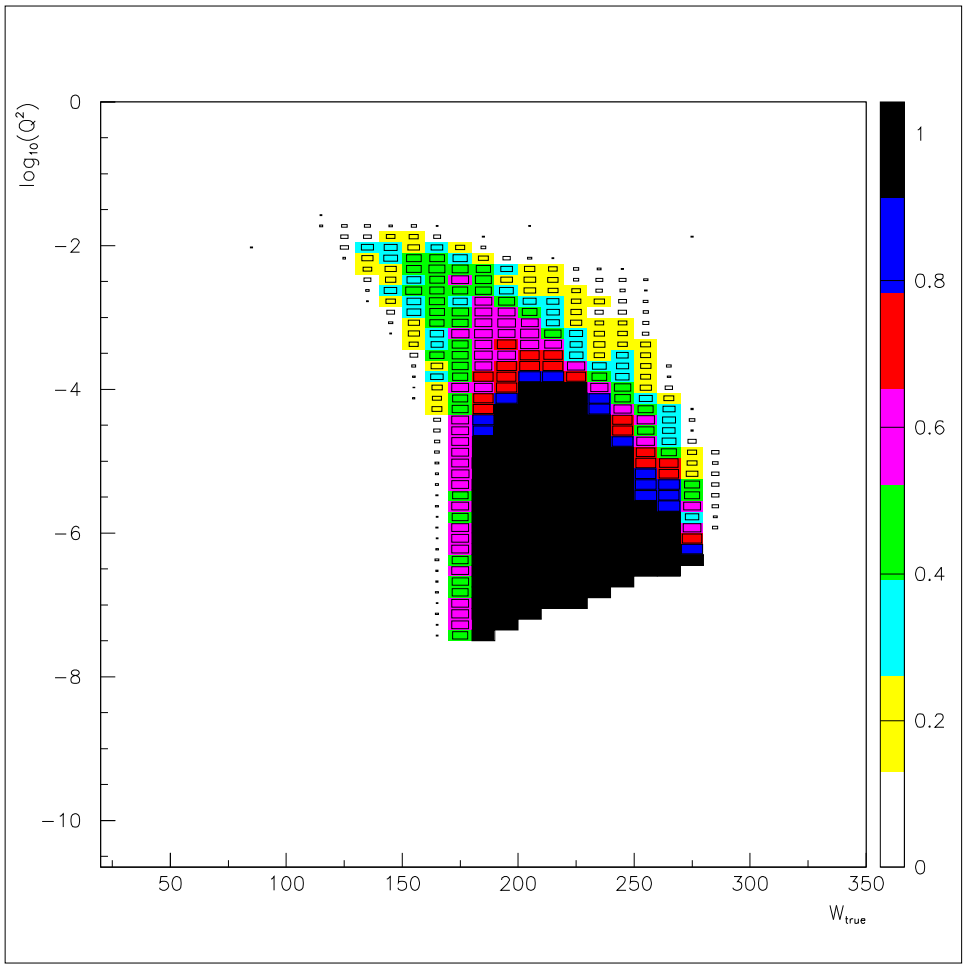

Figure 4.14: The efficiency of the 35m tagger for D^* photoproduction.

Chapter 5

Analysis

5.1 Comparison of Data and Monte Carlo

In this section, the data and Monte Carlo are compared for reconstructed D^* candidates. It is important to check that the MC simulates well the distributions in the data, so we can properly calculate the acceptance for each bin used for the cross sections.

All compared distributions, both the data and MC, are background subtracted. Usually in the data there is significantly higher background than in the MC simulation as the MC only contains events with a charm quark. However, there is disadvantage of doing this: the large error on the resultant number of events after subtraction. Therefore there are large fluctuations in the data distributions, which sometimes makes it difficult to decide if there is a real difference between the data and MC.

The MC used for this analysis is HERWIG 6.301. It was generated by the ZEUS HFL working group. It contains several charm and beauty production and decay modes. The integrated MC luminosity generated for the running periods 1998 - 2000 is about 600 pb^{-1}.

In all distributions shown the MC is normalised to the same luminosity (in data). This normalisation is done for easy comparison between the data and MC, it checks both the shapes of the distributions and the MC cross sections.

5.1.1 CTD Water Correction

In 2000 the gain of the CTD significantly decreased. To fix the aging of the CTD a small amount of water was added to the chamber gas, which affected the CTD gain. This changed the resolution of the CTD, which affected the HFL trigger for the reconstruction of low p_T tracks. Hence some corrections need to be done to take this in to account.

The CTD *water correction* is done following the procedure described below.

First, all D^* candidates from runs with run number greater than 36560 and with $p_T(\pi_s) < 0.25\,\text{GeV}$ (in the data sample) are excluded. Then, the fraction of the D^* candidates for the 1998-2000 MC sample with $p_T(\pi_s) < 0.25\,\text{GeV}$ is calculated, as a ratio of the integrated luminosity in the data before was water added to the CTD gas to the whole integrated luminosity for 1998 - 2000 running period:

$$R = \frac{L_{before\ water}}{L_{1998-2000}} = 0.795 \tag{5.1}$$

This ratio was then used to reweight the events in the MC sample with $p_T(\pi_s) < 0.25\,\text{GeV}$. Due to this effect every 5th D^* candidate in the MC with low $p_T(\pi_s)$ is lost.

5.1.2 Comparison of Kinematic Variables and Their Resolutions

The list of analysis cuts for the 35m and 44m samples from Section 4.3.3 is summarised in Table 5.1.

As can be seen in the table, different cuts on $p_T(D^*)$ and $\eta(D^*)$ were used for the two samples. This is due to the absence of the signal in the first bin of those variables in the 35m data sample, and in the last bin of $\eta(D^*)$ in the 44m data sample.

	Cuts for 44m sample	Cuts for 35m sample
Vertex	$Z_{vtx} < 50$ cm	$Z_{vtx} < 50$ cm
Photoproduction	Electron in 44m tagger $80 < W < 120$ GeV	Electron in 35m tagger $200 < W < 260$ GeV
D^* selection	$\lvert\eta(track)\rvert < 1.75$ $p_T(\pi_s) > 0.12$ GeV/c $p_T(\pi) > 0.4$ GeV/c $p_T(K) > 0.4$ GeV/c $1.81 < D^0 < 1.92$ GeV/c^2 $0.143 < \Delta M < 0.148$ GeV/c^2 $p_T(D^*) > 1.5$ GeV/c $-1 < \eta(D^*) < 1.5$	$\lvert\eta(track)\rvert < 1.75$ $p_T(\pi_s) > 0.12$ GeV/c $p_T(\pi) > 0.4$ GeV/c $p_T(K) > 0.4$ GeV/c $1.81 < D^0 < 1.92$ GeV/c^2 $0.143 < \Delta M < 0.148$ GeV/c^2 $p_T(D^*) > 2$ GeV/c $-1.5 < \eta(D^*) < 1$

Table 5.1: Summary of the selection cuts for the 44m and 35m samples.

In Fig. 5.1 and 5.2 the $p_T(tracks)$, $\eta(tracks)$, $p_T(D^*)$, $\eta(D^*)$ distributions for the 44m tagger and 35m tagger samples are shown. The data are compared to the MC using the normalisation factor, which comes from the ratio of luminosities in the data and MC. As you can see from the plots, the p_T and η distributions for the tracks and D^* candidates are reasonably well described by the MC over the entire range.

The quality of reconstruction of the event kinematics needs to be considered, and shown that it provides an acceptable description of the *true* kinematics. For this the MC sample was used. The correlation between the true MC and the measured kinematic variables is shown in Figs. 5.3 and 5.4. The resolution of the main kinematic variables, mainly where the cross sections were calculated, also was assessed. The resolution shows the spread on the difference between the reconstructed and true values. Hence for kinematic variable X, the absolute resolution can be defined as:

$$R_X = \sigma(X^{REC} - X^{TRUE}), \tag{5.2}$$

where σ is the width of a fit using a Gaussian function to the distribution of difference between true and reconstructed kinematic value. The resolution of the main reconstructed kinematic variables are shown in Figs. 5.5 and 5.6.

The reconstructed and true variables are well correlated.

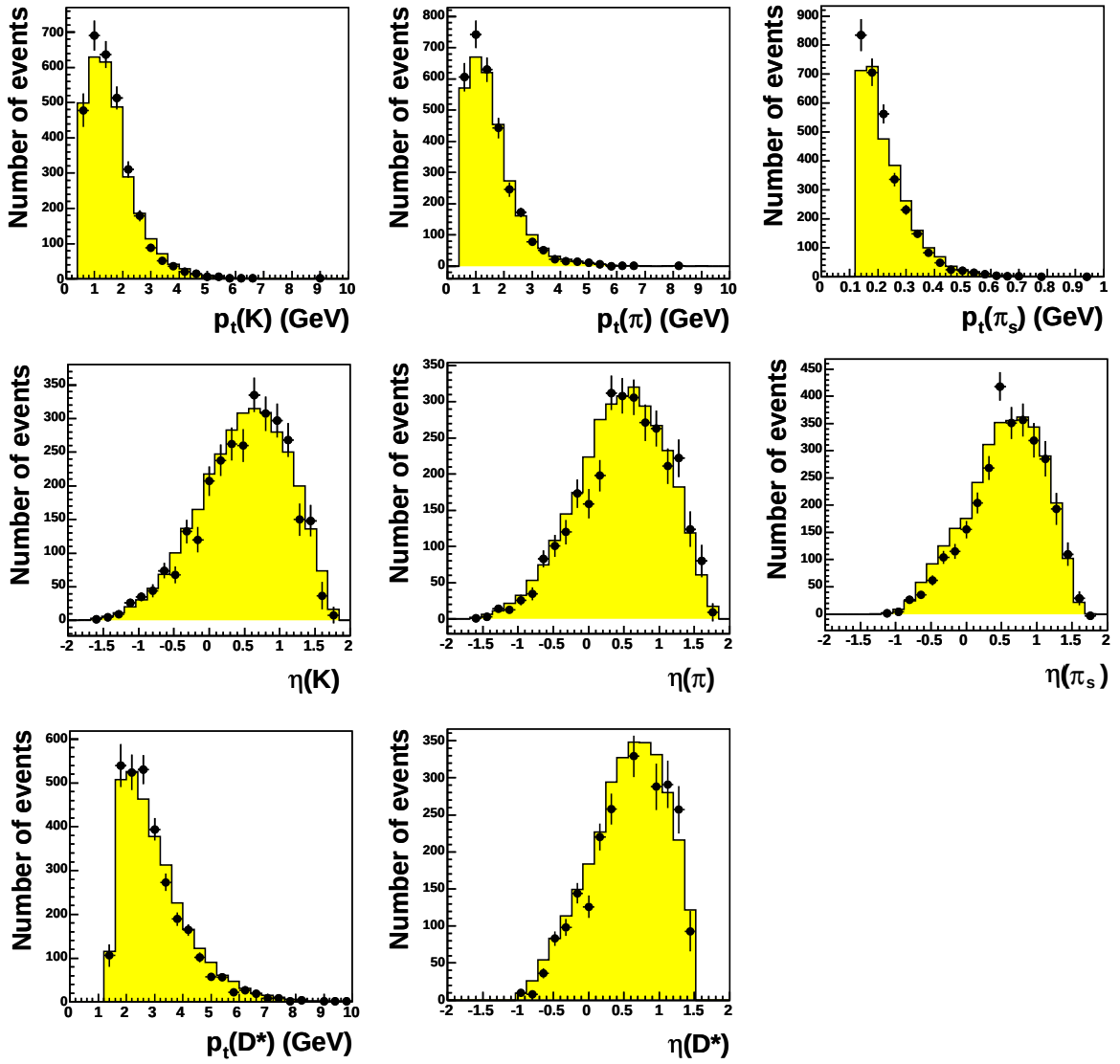

Figure 5.1: 44m DATA - MC comparison of variables related to the D^* reconstruction for D^* candidates. The data are shown as points, the MC is shown as a histogram.

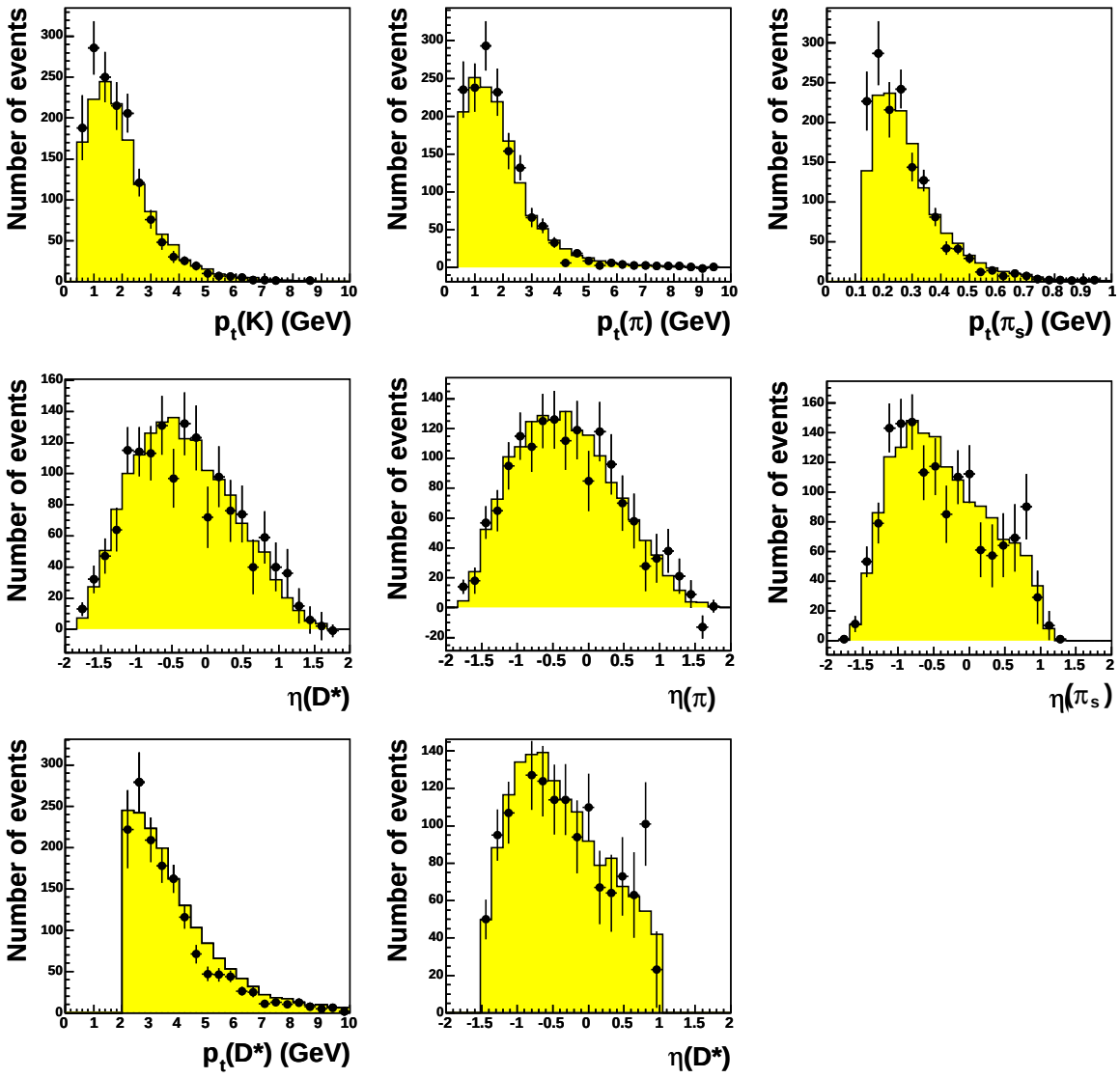

Figure 5.2: 35m DATA - MC comparison of variables related to the D^* reconstruction for D^* candidates. The data are shown as points, the MC is shown as a histogram.

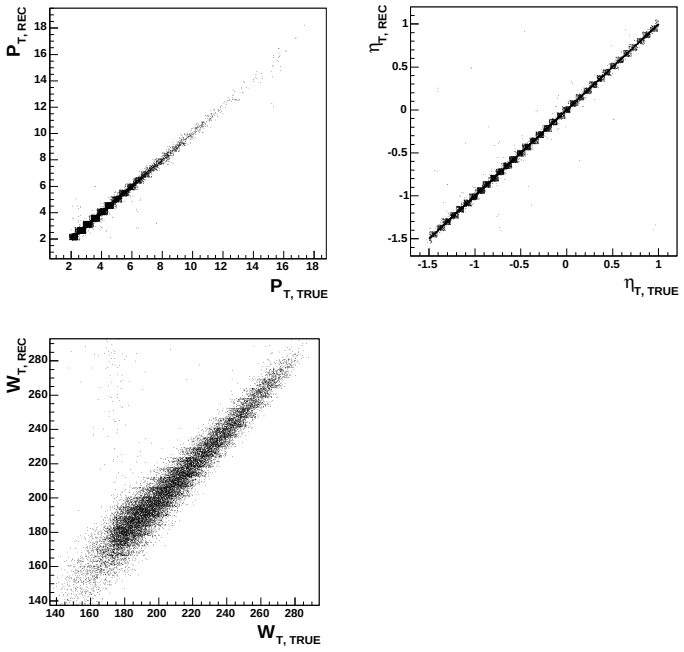

Figure 5.3: Scattered plot of the reconstructed vs. the true kinematic MC variables: $P_T(D^*)$, $\eta(D^*)$ and W for the 44m sample.

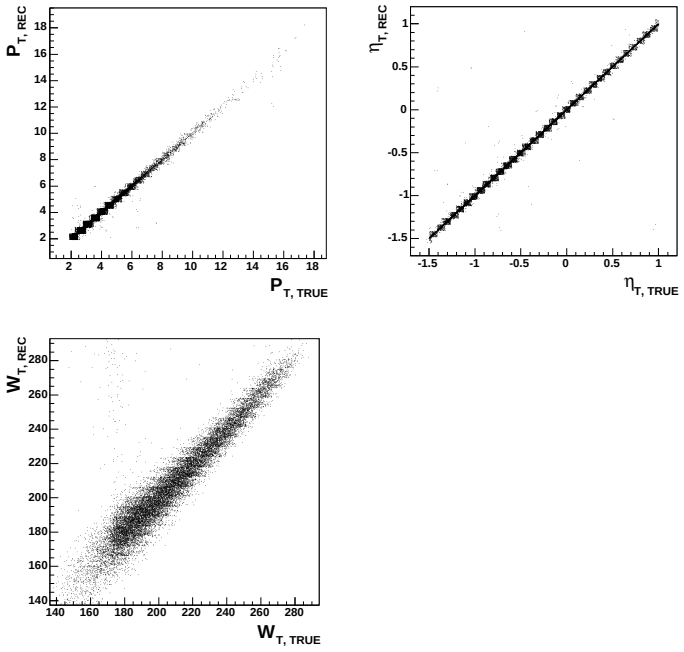

Figure 5.4: Scattered plot of the reconstructed vs. the true kinematic MC variables: $P_T(D^*)$, $\eta(D^*)$ and W for the 35m sample.

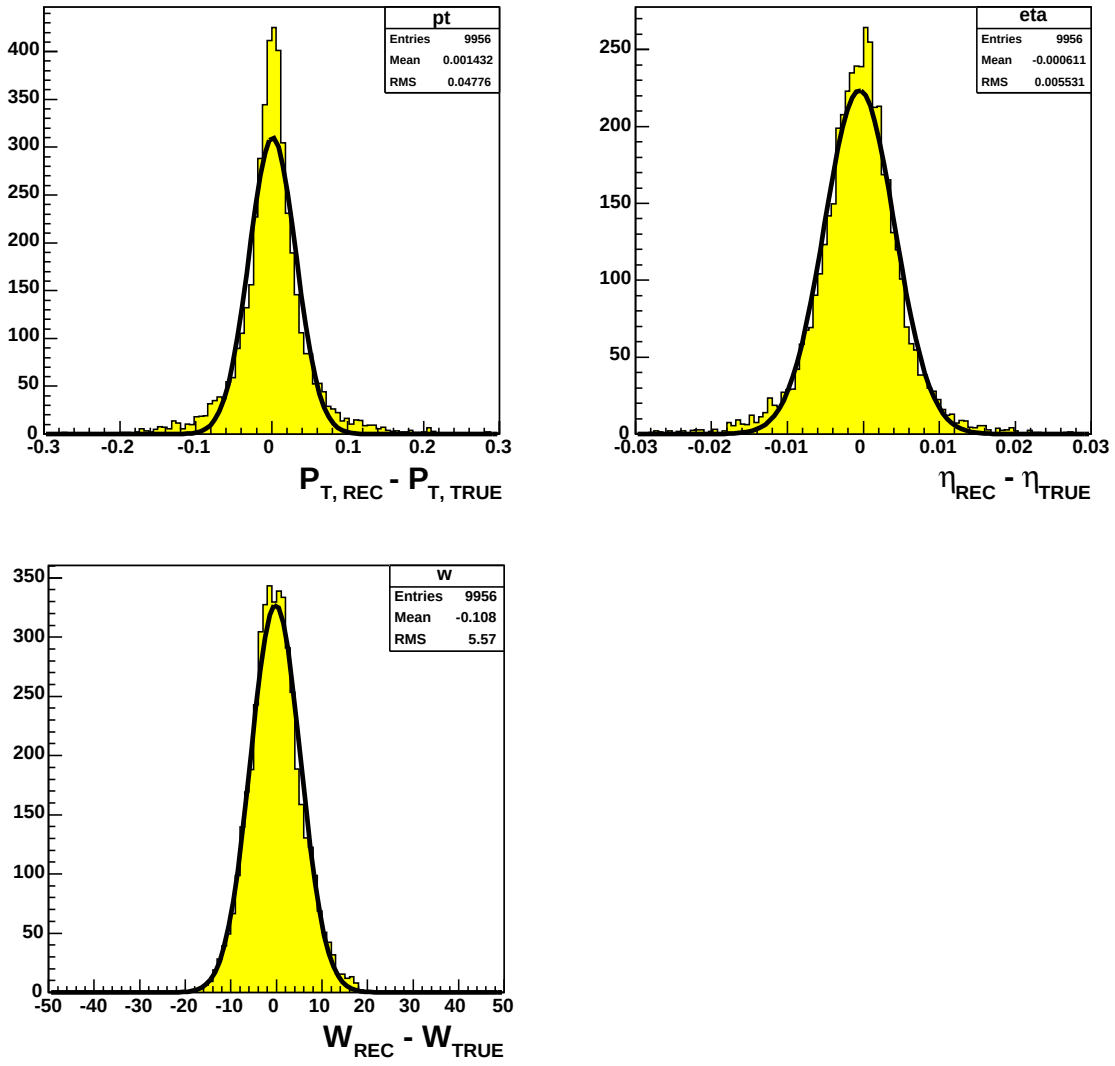

Figure 5.5: Distributions of the differences of the reconstructed and true MC kinematic variables: $P_{T,REC}(D^*) - P_{T,TRUE}(D^*)$ (top-left plot), $\eta_{REC}(D^*) - \eta_{TRUE}(D^*)$ (top-right plot) and $W_{REC}(D^*) - W_{TRUE}(D^*)$ (bottom plot) for the the 44m sample are shown.

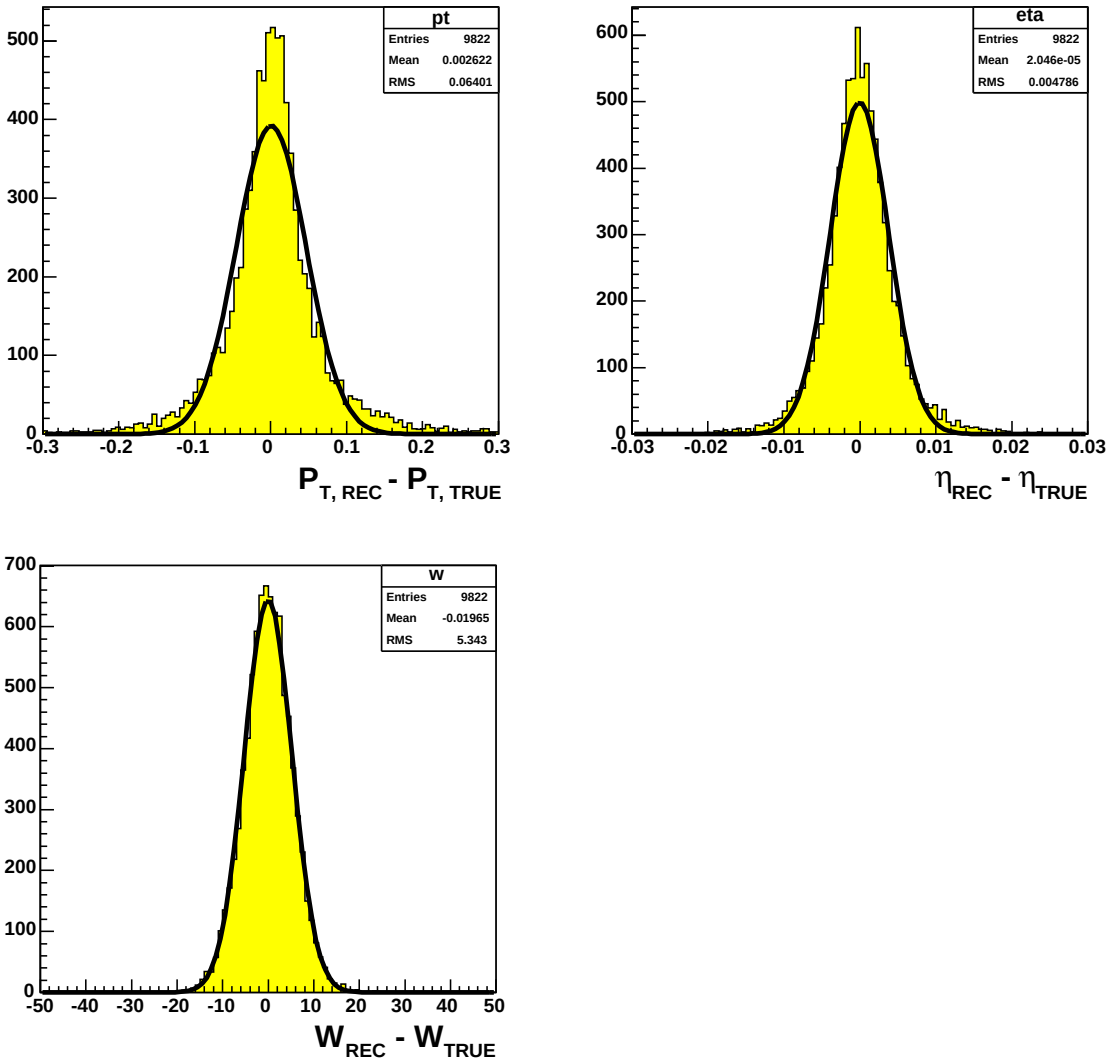

Figure 5.6: Distributions of the differences of the reconstructed and true MC kinematic variables: $P_{T,REC}(D^*) - P_{T,TRUE}(D^*)$ (top-left plot), $\eta_{REC}(D^*) - \eta_{TRUE}(D^*)$ (top-right plot) and $W_{REC}(D^*) - W_{TRUE}(D^*)$ (bottom plot) for the the 35m sample are shown.

5.1.3 Binning the data

The total cross section of the process gives information on the overall normalisation of the production process. It is also interesting to calculate the differential cross sections and to consider the shape of the distributions. For that the complete signal in the large bin, which is defined by the kinematic cuts, is split into smaller bins. The bin definitions of the kinematic variables, $p_t(D^*)$, $\eta(D^*)$, W, for both the 44m and 35m samples where the single differential cross sections were measured is presented in the Table 5.2.

	44m Sample			35m Sample		
Bin	W (GeV)	$p_T(D^*)$ GeV/c	$\eta(D^*)$	W (GeV)	$p_T(D^*)$ GeV/c	$\eta(D^*)$
1	80 - 100	1.5, 2.0	-1.0, -0.5	200 - 220	2.0, 2.5	-1.5, -1.0
2	100 - 120	2.0, 2.5	-0.5, 0.0	220 - 240	2.5, 3.0	-1.0, -0.5
3	—	2.5, 3.0	0.0, 0.5	240 - 260	3.0, 3.5	-0.5, 0.0
4	—	3.0, 3.5	0.5, 1.0	—	3.5, 4.0	0.0, 0.5
5	—	3.5, 4.0	1.0, 1.5	—	4.0, 4.5	0.5, 1.0
6	—	4.0, 4.5	—	—	4.5, 5.0	—
7	—	4.5, 5.0	—	—	5.0, 5.5	—
8	—	5.0, 5.5	—	—	5.5, 6.5	—
9	—	5.5, 6.5	—	—	6.5, 8.0	—
10	—	6.5, 8.0	—	—	—	—
Total	2 bins	10 bins	8 bins	3 bins	9 bins	7 bins

Table 5.2: Bin definitions for the differential cross-section calculations of W, $p_T(D^*)$, $\eta(D^*)$ for 35m and 44m samples.

There are many considerations which have to be taken into account when the kinematic region is divided into bins. For this analysis the statistics, number of D^* candidates, is quite high, so we care most that the bin size should be larger than the resolution of the kinematic variable. As was shown in Fig. 5.5 and 5.6 the resolution of $p_T(D^*)$ and $\eta(D^*)$ is good for both the 44m and 35m samples. Hence those regions were divided into more bins than the W region. The η region for the different taggers split differently. This is due to the different kinematic region which corresponds to different taggers, 44m and 35m. Depending on the tagger the D^* candidates are boosted in different directions compared with the interaction point. The W resolution for both the 44m and 35m samples is poor; that is why W region for both taggers divided into large bins with a width of 20 GeV for both the 44m and 35m taggers. In Figs. 5.7- 5.12 the ΔM distributions for each bin are shown for the data. The ΔM distributions for each bin in the Monte Carlo for both taggers can be found in the Appendix A. The number of D^* candidates and normalisation factor for each of these bins for both data and MC are presented in Appendix B. In most bins there is a clean signal. At high p_t the statistic is low, and the background is large at low p_t and high η.

5.1.4 Acceptance

Due to the detector geometry and efficiency not all events containing a D^* candidate can be measured and reconstructed in the detector. Therefore, for the cross-section calculation, the total number of events has to be correctly defined. It is done by scaling the measured number of events containing a D^* candidate in the data with the acceptance, A.

To do this, first, D^* candidates in the MC in the same kinematic region as the data, are counted. These events are called *generated* events.

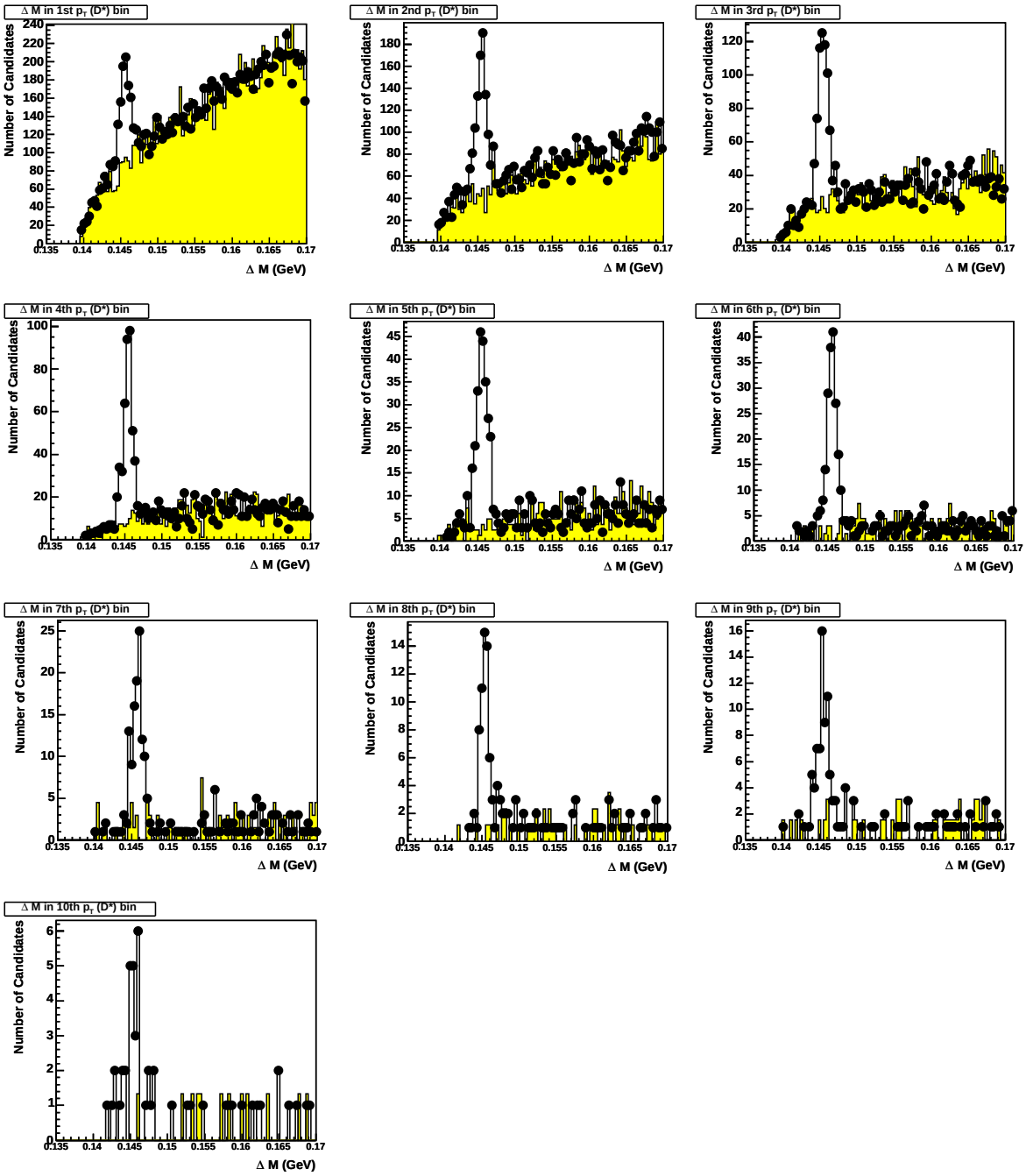

Figure 5.7: ΔM distributions for each bin in $p_T(D^*)$ for the 44m sample. The background distributions from the wrong-charge contributions are normalised in the control region $0.151 < \Delta M < 0.165\,\text{GeV}$. The points represent the correct charge combinations of the D^* candidates and the filled histograms represent the wrong charge combinations of D^* candidates.

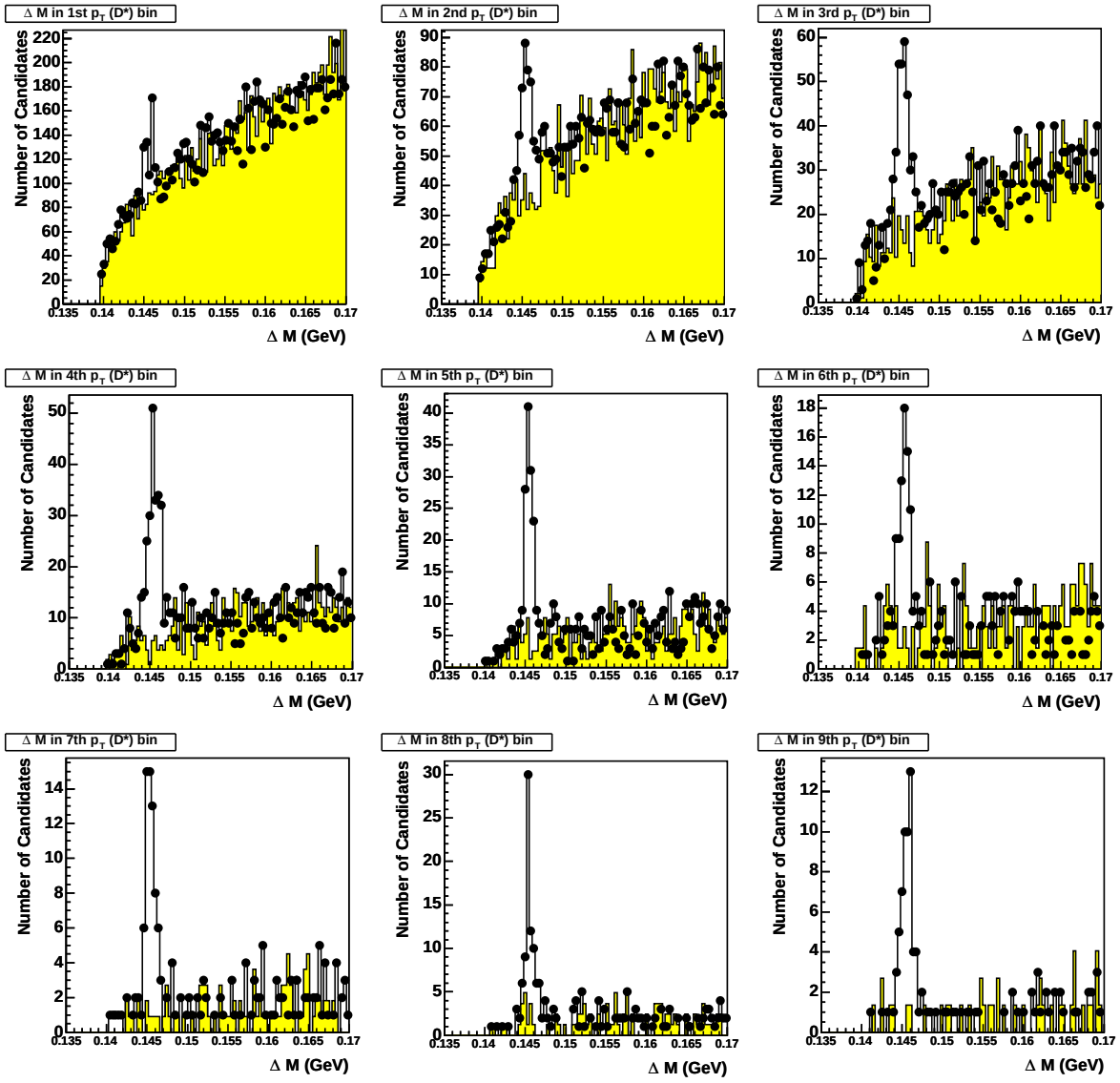

Figure 5.8: ΔM distributions for each bin in $p_T(D^*)$ for the of 35m sample. The background distributions from the wrong-charge contributions are normalised in the control region $0.151 < \Delta M < 0.165\,\text{GeV}$. The points represent the correct charge combinations of the D^* candidates and the filled histograms represent the wrong charge combinations of D^* candidates.

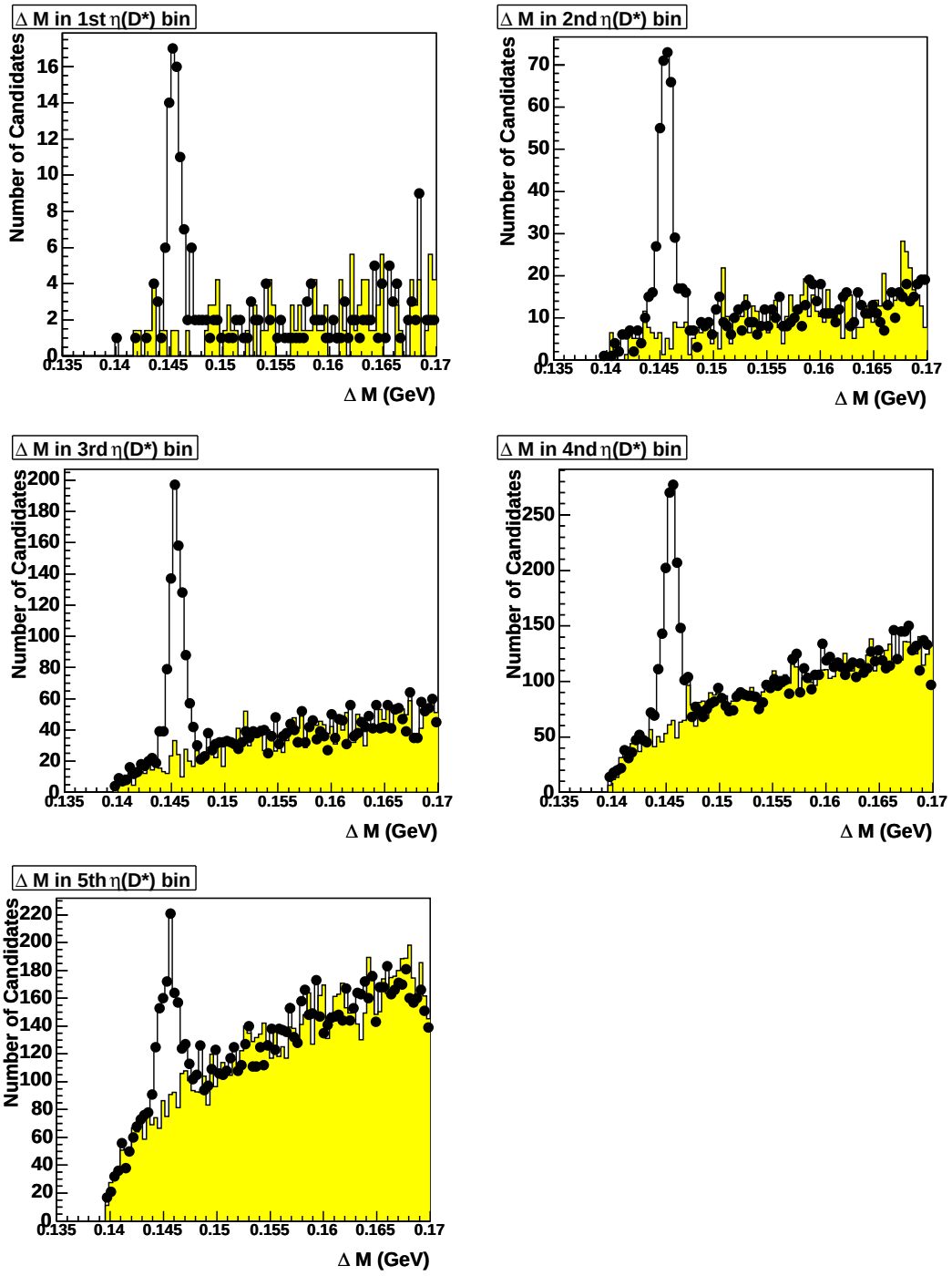

Figure 5.9: ΔM distributions for each bin in $\eta(D^*)$ cross section for the 44m sample. The background distributions are normalised in the control region $0.151 < \Delta M < 0.165\,\text{GeV}$. The points represent the correct charge combinations of the D^* candidates and the filled histograms represent the wrong charge combinations of D^* candidates.

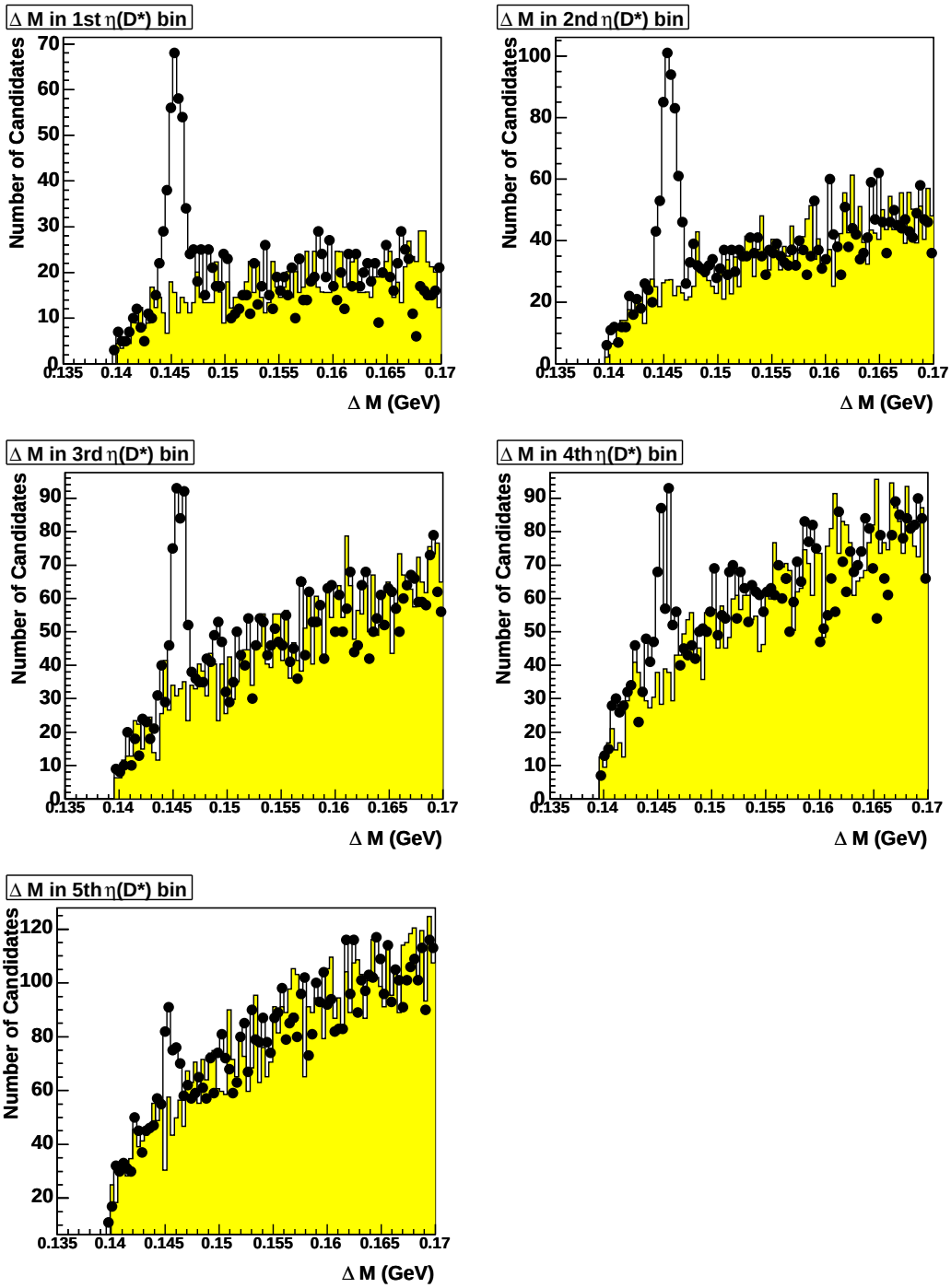

Figure 5.10: ΔM distributions for each bin in $\eta(D^*)$ cross section for the 35m sample. The background distributions are already normalised in the control region $0.151 < \Delta M < 0.165\,\text{GeV}$. The points represent the correct charge combinations of the D^* candidates and the filled histograms represent the wrong charge combinations of D^* candidates.

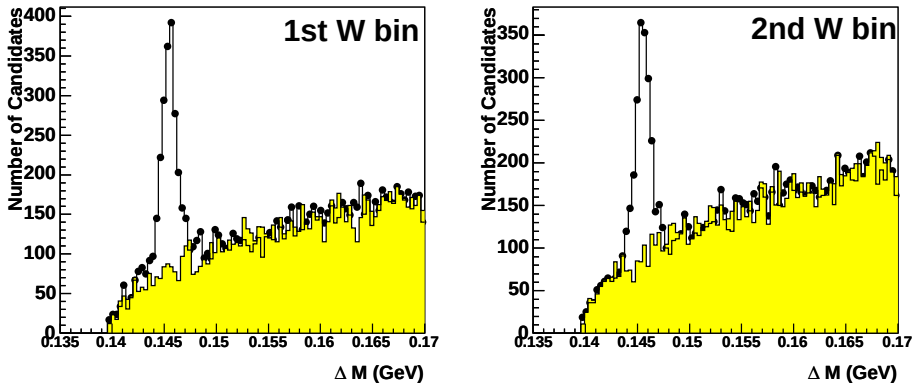

Figure 5.11: ΔM distributions for each bin in W cross section for the 44m sample. The background distributions are normalised in the control region $0.151 < \Delta M < 0.165\,\text{GeV}$. The points represent the correct charge combinations of the D^* candidates and the filled histograms represent the wrong charge combinations of D^* candidates.

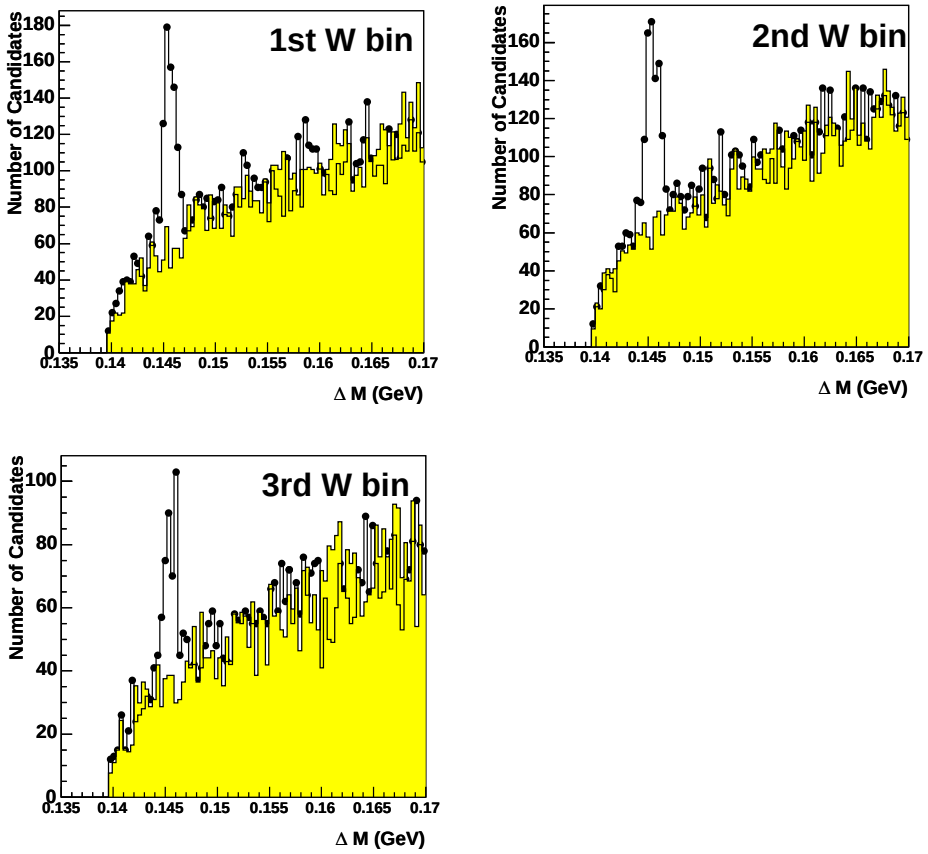

Figure 5.12: ΔM distributions for each bin in W cross section for the 35m sample. The background distributions are already normalised in the control region $0.151 < \Delta M < 0.165\,\text{GeV}$. The points represent the correct charge combinations of the D^* candidates and the filled histograms represent the wrong charge combinations of D^* candidates.

Then, all simulated MC events that pass the same kinematic and trigger cuts are also counted. Such events are called *reconstructed* events. As in the data, in order to extract the number of reconstructed D^* candidates the wrong-sign background subtraction method was used.

The acceptance is calculated as the ratio of the number of events reconstructed to the number of events generated.

$$A = \frac{number\ of\ reconstructed\ D^*\ meson}{number\ of\ generated\ D^*\ meson} \tag{5.3}$$

In this analysis the total acceptance is generally the product of the D^*-meson acceptance and the tagger acceptance. The D^*-meson acceptance depends on the geometrical acceptance and the track reconstruction in CTD, whereas the electron tagger acceptance depends on the kinematic parameters of the scattered electron, see Sec. 4.4 and 4.5. The acceptance of the 44m tagger is not implemented in the MC simulation program. Therefore the total acceptance is calculated from the D^* acceptance as a function of W weighted by the tagger acceptance as a function of W. For the 35m tagger the acceptance of the tagger is already simulated in MC. Therefore for the 35m tagger analysis only one acceptance was calculated.

The total acceptances of D^* mesons for both the 44m and 35m samples are calculated as a function of $\eta(D^*)$, $p_T(D^*)$ and W, and are shown in Fig. 5.14 and 5.13. The difference between $\eta(D^*)$ acceptances are due to the taggers, accepting different ranges of W.

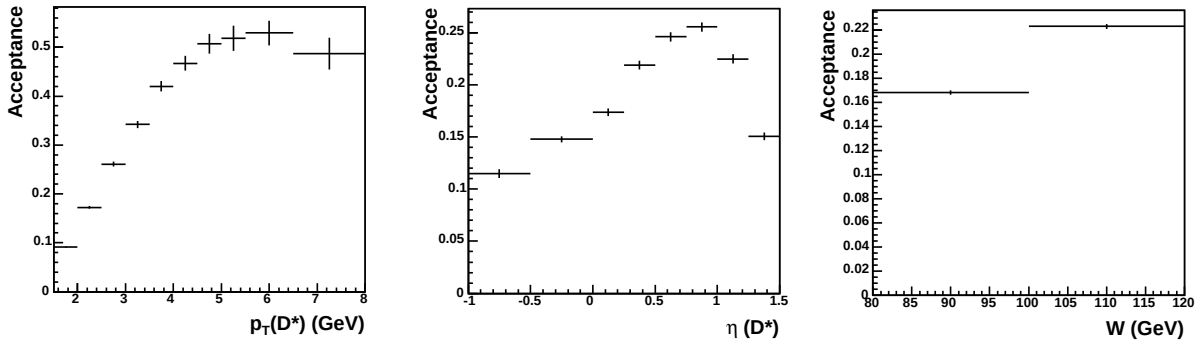

Figure 5.13: Acceptance in each bin of cross section for the 44m sample as a function of $p_T(D^*)$, $\eta(D^*)$ and W.

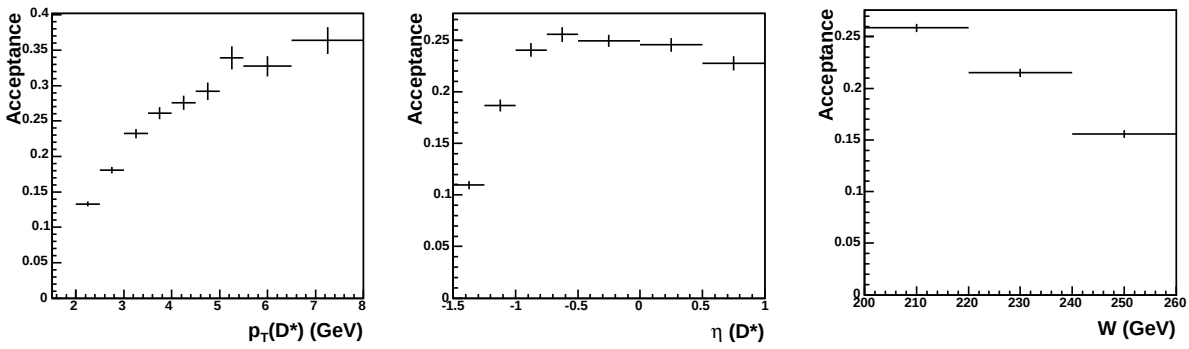

Figure 5.14: Acceptance in each bin of cross section for the 35m sample as a function of $p_T(D^*)$, $\eta(D^*)$ and W.

5.2 Cross Sections

The cross section for the process $ep \longrightarrow e'D^*X$ is calculated using:

$$\sigma_{ep\longrightarrow e'D^*X} = \frac{N(D^*)}{A \cdot B(D^{*\pm} \longrightarrow K\pi\pi_s) \cdot L_{int}} \ , \tag{5.4}$$

where $N(D^*)$ is the number of D* candidates observed in the signal region after background subtraction in the data, A is the total acceptance, BR is the branching ration of D^* mesons decaying into the $K\pi\pi_s$ channel and L_{int} is the integrated luminosity of the data set used for this analyses, see Tab. 4.1.

5.2.1 Total Cross Sections

Using equation 5.4, the total cross section for the $ep \longrightarrow e'D^*X$ process with the number of D^* from Eq. 4.22 for 44m sample is

$$\sigma_{ep\longrightarrow e'D^*X} = 7.19 \pm 0.39 \,\text{nb}, \tag{5.5}$$

where the quoted error is statistical only. This is calculated in the kinematic region $Q^2 < 0.015$ GeV^2, $80 < W < 100$ GeV, $p_T(D^*) > 1.5$ GeV, $-1.0 < \eta(D^*) < 1.5$.

Similarly the total cross section for 35m sample with the number of D^* candidates from Eq. 4.23 is

$$\sigma_{ep\longrightarrow e'D^*X} = 2.99 \pm 0.26 \,\text{nb}, \tag{5.6}$$

where the kinematic region is restricted to $Q^2 < 0.02$ GeV^2, $200 < W < 260$ GeV, $p_T(D^*) > 2$ GeV, $-1.5 < \eta(D^*) < 1$.

The same kinematic limits are applied to the differential cross sections, discussed in the next section, for both 35m and 44m samples.

The systematic errors on these values are evaluated and presented in Sec. 5.3.

5.2.2 Differential Cross Sections

The large available data sample allows us to measure the cross section differentially in $p_T(D^*), \eta(D^*)$ and W.

The differential cross sections are calculated for each bin, n, defined in the Table 5.2, of the kinematic variables using:

$$\frac{d\sigma}{dX_n}(ep \longrightarrow e'D^*X) = \frac{N_{X_n}(D^*)}{A_{X_n} \cdot B(D^{*\pm} \longrightarrow K\pi\pi_s) \cdot L \cdot \Delta_{Xn}} \ , \tag{5.7}$$

where X represents kinematic variable where cross section is calculated differentially, $N_{X_n}(D^*)$ is the number of signal events in the nth bin, A_{X_n} is the acceptance in the bin and Δ_{X_n} is the bin width. The differential cross sections for both the 44m and 35m analyses are shown in Fig. 5.16 and 5.15. The results are tabulated in Tables 5.5 - 5.10.

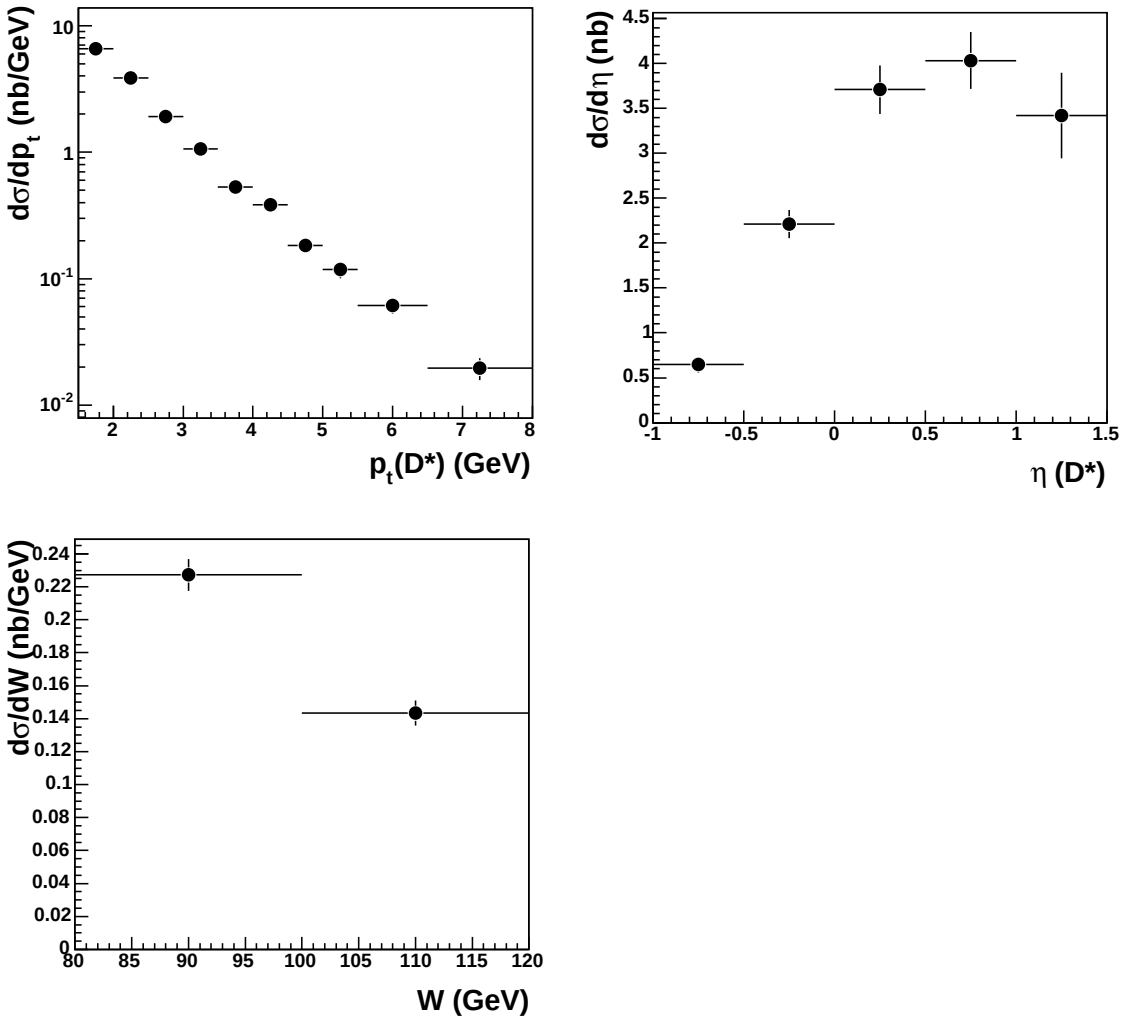

Figure 5.15: Differential cross sections analysis using the 44m tagger as a function of $p_T(D^*)$, $\eta(D^*)$ and W.

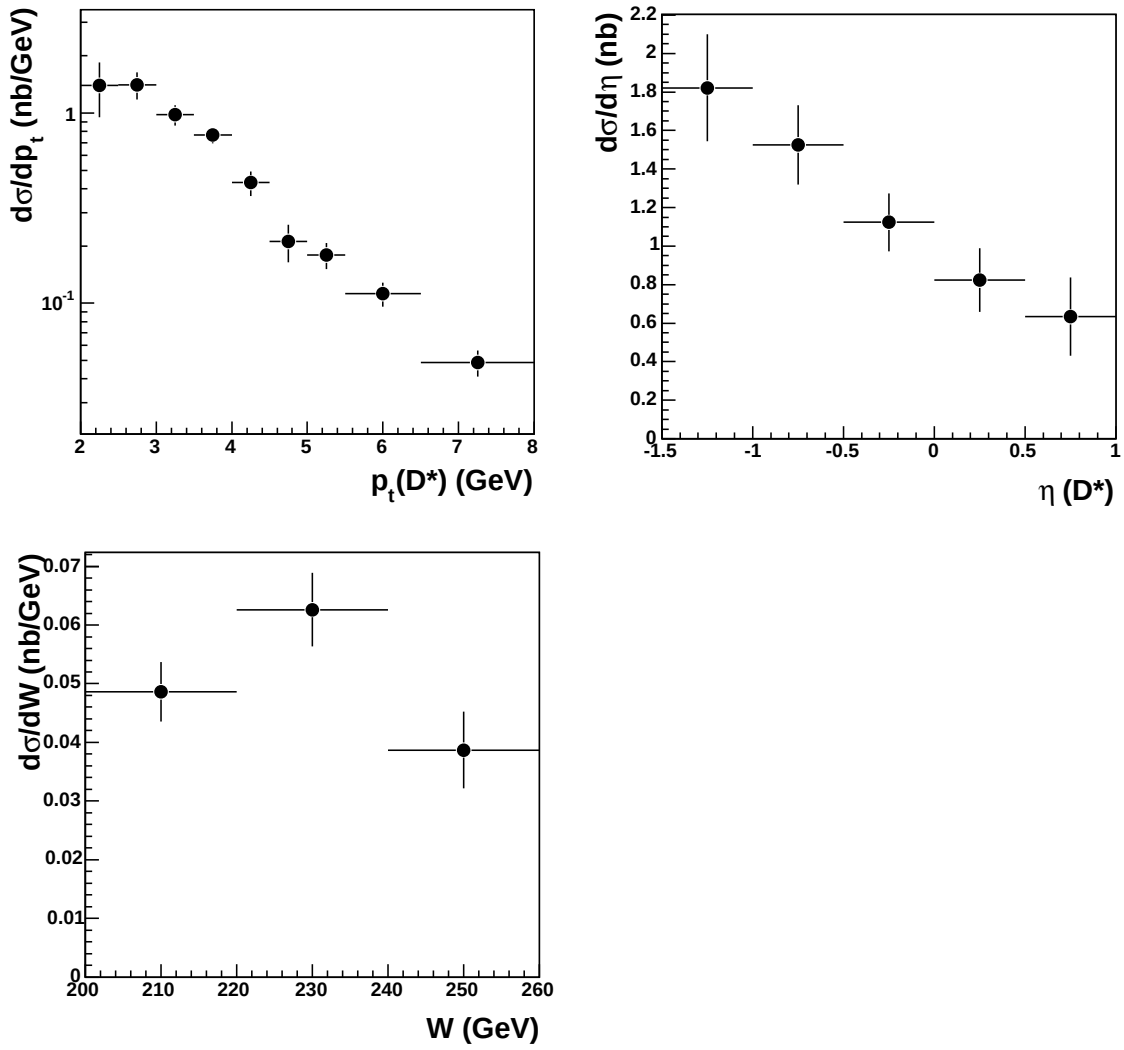

Figure 5.16: Differential cross sections analysis using the 35m tagger as a function of $p_T(D^*)$, $\eta(D^*)$ and W.

5.2.3 Total Charm Cross Sections

In order to obtain the total charm cross sections from the visible cross sections within a limited (P_T, η) phase space the visible cross sections are extrapolated to the full (p_T, η) phase space at fixed W using:

$$\sigma_{\gamma p}^{DATA}(c\bar{c})(W_{fixed}) = \frac{\sigma_{ep}^{DATA}(D^*)}{\sigma_{ep}^{FMNR}(D^*)}\ \sigma_{\gamma p}^{FMNR}(c\bar{c})(W_{fixed}) \tag{5.8}$$

The theoretical calculations have been done with the GRV-G HO photon PDF set. Two values of the total charm photoproduction cross section was calculated: one for the 44m analysis with $80\,\text{GeV} < W < 120\,\text{GeV}$ at $W = 100$ GeV, and another one for the 35m analysis with $200\,\text{GeV} < W < 260\,\text{GeV}$ at the $W = 230$ GeV:

$$\sigma_{\gamma p \longrightarrow c\bar{c}X} = 8.75\mu\text{b} \quad \text{at} \langle W_{\gamma p} \rangle \approx 230\,\text{GeV}, \tag{5.9}$$

$$\sigma_{\gamma p \longrightarrow c\bar{c}X} = 4.45\mu\text{b} \quad \text{at} \langle W_{\gamma p} \rangle \approx 100\,\text{GeV}. \tag{5.10}$$

An important aspect of the extrapolation to the total charm photoproduction cross section and transferring the electroproduction cross sections into the photoproduction cross sections is the photon flux. For FMNR calculations the electroproduction cross sections are evaluated by transferring the photoproduction cross sections using the flux factor.

5.2.4 The Photon Flux

In photoproduction processes, $Q^2 \sim 0\,\text{GeV}$, the lepton-proton collisions can be regarded as a collision between a real quasi-photon and a proton. The boson exchange between the lepton and the proton take place via a photon. The contribution from the weak interactions can be neglected, since the Z and $W^{\pm}$ boson propagators are essentially zero (they are expressed as $Q^2/(M_{W/Z}^2 + Q^2)$), as can the longitudinal component of the cross section (σ_L). Therefore, in photoproduction, the lepton-proton interaction can be described as a photon-proton scattering. As was discussed in Sec. 1.4, the photon besides coupling directly to one of partons from proton can also act like a hadron.

The hadronic structure of the photon has been studied at e^+e^- collider processes where one highly virtual photon emitted by one of the incoming leptons interacts with an almost real photon from the other lepton (Fig. 5.17). The process $e^+e^- \longrightarrow e^+e^- hadrons$ can be regarded as an interaction between a real photon and an electron, $e\gamma \longrightarrow ehadrons$. The flux of quasi-real photons from the electron is factorised using the Equivalent Photon Approximation (EPA) [48]:

$$\frac{d\sigma}{dz}(ee \longrightarrow eeX) = f^{\gamma e}(z)\sigma(e\gamma \longrightarrow eX), \tag{5.11}$$

where z is the fraction of the electron energy carried by the photon, and the flux $f^{\gamma e}$ is given by:

$$f^{\gamma e}(z) = \frac{\alpha}{2\pi}\left[\frac{1+(1-z)^2}{z}\log\frac{P_{max}^2}{P_{min}^2} - 2m_e^2 z\left(\frac{1}{P_{min}^2} - \frac{1}{P_{max}^2}\right)\right], \tag{5.12}$$

where P_{min}^2 is the kinematic limit,

$$P_{min}^2 = \frac{m_e^2 z^2}{1-z} \tag{5.13}$$

and P_{max}^2 corresponds to the maximum scattering angle θ_{max} for the electron not to be detected.

$$P_{max}^2 = (1-z)E_{beam}^2\theta_{max}^2. \tag{5.14}$$

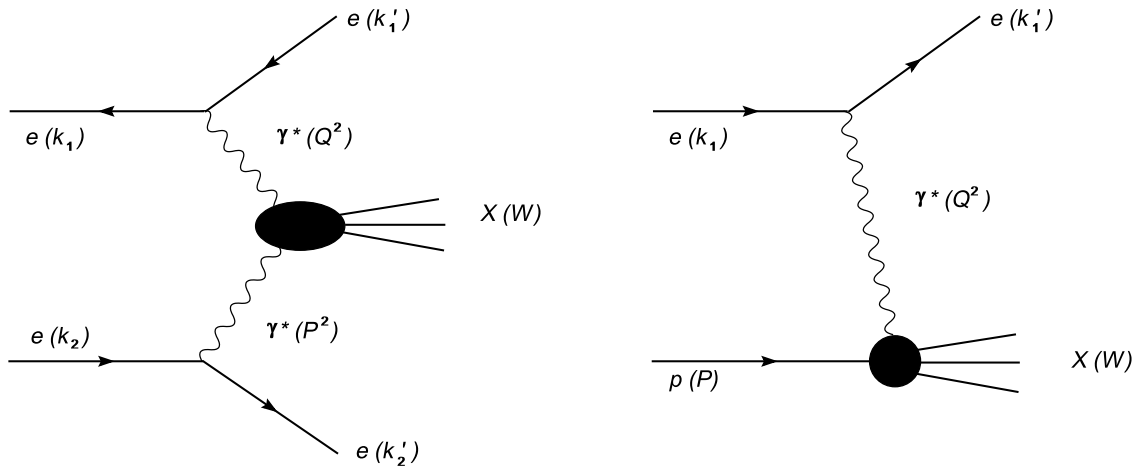

Figure 5.17: In the left plot two-photon production in e^+e^- collisions is shown. If $P^2 = -(k_2 - k_2')^2 \approx 0$ and $Q^2 = -(k_1 - k_1')^2 > 0$ the photon structure function can be studied: the high Q^2 photon is the probe, while the other is the target. The right plot shows photoproduction in HERA.

The structure of the photon can also be studied in ep collisions at HERA. In the photoproduction regime, when $Q^2 \sim 0\,\mathrm{GeV}$ and the exchanged photon is almost real, the electron-proton scattering can be regarded as a γp scattering (Fig. 5.17b). In this case the photon direction is collinear with the lepton beam and by analogy to the e^+e^- scattering, the electroproduction cross section can be expressed by the photoproduction cross section and the photon flux of the quasi-real photon from the lepton vertex:

$$\sigma^{ep} = \Phi^{\gamma e}\sigma^{\gamma p}. \tag{5.15}$$

The photon flux, $\Phi^{\gamma e}$, can be obtained from equation 5.12 by replacing the energy fraction z with the inelasticity, y:

$$\Phi^{\gamma e} = \frac{\alpha}{2\pi}\left[\frac{1+(1-y)^2}{y}\log\frac{Q^2_{max}}{Q^2_{min}} - 2m_e^2 y\left(\frac{1}{Q^2_{min}} - \frac{1}{Q^2_{max}}\right)\right], \tag{5.16}$$

where Q^2_{min} and Q^2_{max} has the same meaning as P^2_{min} and P^2_{max} defined in the equations 5.13 and 5.14. In this analysis the upper limit of the Q^2 value is limited by taggers. For the 35m tagger $Q^2_{max} = 0.02\,\mathrm{GeV}^2$ and for the 44m tagger $Q^2_{max} = 0.015\,\mathrm{GeV}^2$. According to Eq. 5.13, the lower limit of Q^2 is almost 0 ($10^{-9}\,\mathrm{GeV}^2$).

For a certain kinematic range of W and Q^2 we have:

$$\sigma_i^{ep} = \int_{Q^2_{min}}^{Q^2_{max}}\int_{y_{min,i}}^{y_{max,i}} \Phi^{\gamma e}(y,Q^2)\ \sigma^{\gamma p}(y,Q^2)\ dy\ dQ^2, \tag{5.17}$$

where the y range is determined from the W range (see equation 4.6).

The photoproduction cross sections are evaluated in different $W_{0,i}$ regions:

$$\sigma_i^{\gamma p} = \sigma^{\gamma p}(W_{0,i}), \tag{5.18}$$

where $W_{0,i}$ is the mean of the W distribution of the reconstructed signal Monte Carlo in a bin.

Practically it is done by converting the electroproduction cross section into photoproduction cross section in each W region with a corresponding flux factor for that region. In the Table 5.3 the photon flux and the cross sections for the kinematic range of W for both taggers are shown.

44m Tagger Sample				
W range	W_0[GeV]	$\Phi_i^{\gamma p}$ $[10^{-3}]$	$\sigma_{ep}^{DATA}(W_0)$ nb	$\sigma_{\gamma p}^{DATA}(W_0)$ nb
$80 < W < 120$ GeV	100	24.92	7.19 ± 0.39	288.5 ± 15.6
35m Tagger Sample				
$200 < W < 260$ GeV	230	8.34	2.99 ± 0.26	358.5 ± 31.2

Table 5.3: The tabulated results of the D^* electroproduction and photoproduction visible cross sections as well the photon fluxes for both the 44m and 35m samples.

5.3 Systematic uncertainties

Besides the statistical errors it is important to asses the uncertainty for the measured cross section due to the choice of cuts made for the final selection, the extraction method and the Monte Carlo model used in this analysis. In this section the systematic errors of the measured cross sections have been estimated for different sources of uncertainty.

For that purpose cross sections have been re-calculated by changing the procedure or varying the cuts. The cross sections (σ_i') obtained by varying parameters are compared to the nominal ones (σ_0), which were obtained by the optimized procedure and cuts described in the previous chapters. For each systematic source, i, for example the tagger acceptance, the upper and lower systematical errors from that source (Δ_i^+ and Δ_i^-) were calculated by:

$$\Delta_i^+ = \begin{cases} \delta_i & (\delta_i > 0) \\ 0 & (\delta_i < 0) \end{cases} \tag{5.19}$$

$$\Delta_i^- = \begin{cases} 0 & (\delta_i > 0) \\ \delta_i & (\delta_i < 0) \end{cases} \tag{5.20}$$

where δ_i is the deviation of the cross section given by

$$\delta_i = \sigma_i' - \sigma_0. \tag{5.21}$$

Afterwards all systematic errors were added in quadrature:

$$\Delta_i^+ = \sqrt{\sum_i (\Delta_i^+)^2} \tag{5.22}$$

$$\Delta_i^- = \sqrt{\sum_i (\Delta_i^-)^2} \tag{5.23}$$

The following set of systemtic checks was done for this analysis

- **PYTHIA**. This systematic estimates the influence of the Monte Carlo model. For the nominal values of the cross sections the HERWIG Monte Carlo is used, while the PYTHIA is used for the systematic error. The PYTHIA Monte Carlo is not applicable

for this analysis as the Q^2 ($Q^2 \sim 0$) distribution for the kinematic region of the tagger is not correct. Thus the errors are taken from other inclusive D^* analysis [71] . In that analysis the systematical error on the Monte Carlo is neglegible at low $p_t(D^*)$ and varies from -2.2% till -4.6% for the high $p_T(D^*)$ values. Our $p_T(D^*)$ is small compared to that analysis, $p_t^{44m}(D^*) > 1.5\,\mathrm{GeV}$, $p_t^{35m}(D^*) > 2.0\,\mathrm{GeV}$. To be conservative the systematic error for both the 44m and the 35m taggers is taken to be -4%.

- **Tagger acceptance**. This systematic is estimated for both the 44m and 35m taggers. The 44m tagger systematics includes checks on the LUMI photon detector calibration, the position and geometry of the tagger, the error of the x-vertex, v_x, distribution measurement. It is $\sim 7\%$. The 35m tagger systematics includes checks on the LUMI photon detector calibration, different simulation programs, influence of the "quadrupole" description, the error on the v_x distribution measurement, electron beam tilt. It is estimated to be $\sim 8\%$. In table 5.4 the list of the systematic errors for taggers is presented;

Contribution from	Range	35m tagger[%]	44m tagger[%]
vertex x position	$\pm 1\sigma$	2.9	
vertex x position rms	$\pm 1\sigma$		
influence of the magnet position	0.1 cm	1	
different simulation program		1.7	–
x tilt	± 0.05 mrad	3–6	
x tilt rms	± 50 %		
γ-cal calibration constant	± 0.5 %	1.1	
γ-cal calibration correlated error:		3.4	–
γ-cal calibration constant	± 1 %		
filter deposit	$\pm$ 25 %		
electronic non-linearity	$\pm 1\sigma$		
Total		8	7

Table 5.4: Systematic errors for the taggers acceptance.

- **Shift of the CTD momentum scale ($\pm$ 0.3%)**. These uncertainties arise from the kinematic selection cuts, p_T, etc. They have been investigated by varying the cut value on the reconstructed variables in the data for both the 44m and 35m taggers and re-evaluating cross sections. Fot the both taggers the systematic errors are very small;

- **Signal extraction (+2.5%/−1.51%; +3.48%/−2.7%)**. These uncertainties are arising from D^* cuts and background subtraction. They have been investigated by varying the size of the mass window, ΔM, by ± 1 MeV, and the size of the "control regions" for wrong charge background subtraction by $\pm$ 10 MeV;

- **Shift of electron energy for the 35m tagger (+4.1%, -3.4%)**. This comes from the uncertainty of the energy scales of the electron calorimeter, E_e, and the emitted photon energy, E_γ, for the 35m tagger. It has been investigated by varying those variables by $\pm 1\%$

- **Shift of energy of hadronic system in the CAL for the 44m tagger (+1.0%,-0.2%)**. This comes from uncertainty of the energy scales of the uranium CAL for the 44m tagger. The relative uncertainty of the hadronic energy scale was 2 % for the

RCAL and 1 % for the FCAL and BCAL [72]. For the 44m tagger most of the events are detected in the FCAL and BCAL ($-1 < \eta(D^*) < 1.5$). Therefore for systematic uncertainty on the energy measured in calorimeter the energy scale was varied by $\pm 1\%$. Variaton of energy scale of the calorimeter by this amount in the detector simulation induces small shifts of the Jacquet-Blondel estimators of the kinematic variable.

- **Luminocity**. The uncertainty of the luminosity measurement in 1998 - 2000 was estimated to be 2%.
- **Branching ratio**. The uncertainties coming from the D^* and D^0 branching ratios is 0.06% [65].

The largest systematic uncertainty comes from the acceptance of the taggers. Uncertainty coming from luminosity determination and branching ratio of D^* decaying into $K\pi\pi_s$ is included in neither the figures nor the tables.

The tabulated variables of differential cross sections for D^* production $d\sigma/dp_T$, $d\sigma/d\eta$ and $d\sigma/dW$ measured with the 44m and the 35m taggers, including statistical and systematic uncertainties are shown in the Tab. 5.7-5.8. The systematics for each bin of the differential cross sections are presented in the Appendix C.

For the cross differential section in W from the 44m tagger, the systematic uncertainties are in general larger, or about the same size as the statistical uncertainty, in contrast to the cross sections in p_T and η where they are generally smaller than the statistical uncertainty. This is because the W distribution has only two bins, so the statistical precision is correspondingly higher. In terms of the fraction of the cross section, the systematic uncertainty for the W distribution is approximately 10% overall which is approximately the same as for the p_T and η distributions (see Appendix C).

The systematics of the total charm photoproduction cross section also includes the extrapolation uncertainty due to the choice of the charm quark mass and scales. The systematics of the total visible D^* photoproduction cross-sections and the total charm cross sections are summarized in the Table 5.11.

p_T range [GeV]	$d\sigma/dp_T$ [nb/GeV]	stat	systematic
1.5 – 2.0	6.601	$\pm$ 0.663	$^{+\ 0.037}_{-\ 0.422}$
2.0 – 2.5	3.878	$\pm$ 0.275	$^{+\ 0.174}_{-\ 0.202}$
2.5 – 3.0	1.917	$\pm$ 0.144	$^{+\ 0.177}_{-\ 0.091}$
3.0 – 3.5	1.058	$\pm$ 0.077	$^{+\ 0.044}_{-\ 0.063}$
3.5 – 4.0	0.530	$\pm$ 0.044	$^{+\ 0.003}_{-\ 0.031}$
4.0 – 4.5	0.382	$\pm$ 0.033	$^{+\ 0.004}_{-\ 0.030}$
4.5 – 5.0	0.183	$\pm$ 0.025	$^{+\ 0.012}_{-\ 0.009}$
5.0 – 5.5	0.118	$\pm$ 0.018	$^{+\ 0.002}_{-\ 0.010}$
5.5 – 6.5	0.061	$\pm$ 0.008	$^{+\ 0.005}_{-\ 0.005}$
6.5 – 8.0	0.020	$\pm$ 0.004	$^{+\ 0.002}_{-\ 0.005}$

Table 5.5: Differential cross sections of the 44m tagger in each $p_T(D^*)$ bin with the statistical and systematic errors.

η range	$d\sigma/d\eta$ [nb]	stat	systematic
-1.0 – -0.5	0.648	± 0.090	$^{+\ 0.003}_{-\ 0.076}$
-0.5 – 0.0	2.211	± 0.157	$^{+\ 0.081}_{-\ 0.157}$
0.0 – 0.5	3.709	± 0.271	$^{+\ 0.095}_{-\ 0.185}$
0.5 – 1.0	4.033	± 0.315	$^{+\ 0.029}_{-\ 0.202}$
1.0 – 1.5	3.421	± 0.474	$^{+\ 0.456}_{-\ 0.268}$

Table 5.6: Differential cross sections of the 44m tagger in each $\eta(D^*)$ bin with the statistical and systematic errors.

W range [GeV]	$d\sigma/dW$ [nb/GeV]	stat	systematic
80.0 – 100.0	0.227	± 0.010	$^{+\ 0.015}_{-\ 0.021}$
100.0 – 120.0	0.143	± 0.008	$^{+\ 0.004}_{-\ 0.008}$

Table 5.7: Differential cross sections of the 44m tagger in each W bin with the statistical and systematic errors.

p_T range [GeV]	$d\sigma/dp_T$ [nb/GeV]	stat	systematic
2.0 – 2.5	1.400	± 0.451	$^{+\ 0.344}_{-\ 0.232}$
2.5 – 3.0	1.405	± 0.229	$^{+\ 0.131}_{-\ 0.185}$
3.0 – 3.5	0.981	± 0.122	$^{+\ 0.094}_{-\ 0.101}$
3.5 – 4.0	0.769	± 0.076	$^{+\ 0.092}_{-\ 0.074}$
4.0 – 4.5	0.430	± 0.063	$^{+\ 0.051}_{-\ 0.045}$
4.5 – 5.0	0.211	± 0.047	$^{+\ 0.036}_{-\ 0.042}$
5.0 – 5.5	0.179	± 0.028	$^{+\ 0.016}_{-\ 0.023}$
5.5 – 6.5	0.112	± 0.016	$^{+\ 0.010}_{-\ 0.015}$
6.5 – 8.0	0.049	± 0.008	$^{+\ 0.005}_{-\ 0.005}$

Table 5.8: Differential cross sections of the 35m tagger in each $p_T(D^*)$ bin with the statistical and systematic errors.

η range	$d\sigma/d\eta$ [nb]	stat	systematic
-1.5 – -1.0	1.822	± 0.277	$^{+\ 0.199}_{-\ 0.179}$
-1.0 – -0.5	1.526	± 0.207	$^{+\ 0.144}_{-\ 0.173}$
-0.5 – 0.0	1.123	± 0.150	$^{+\ 0.105}_{-\ 0.159}$
0.0 – 0.5	0.823	± 0.165	$^{+\ 0.179}_{-\ 0.124}$
0.5 – 1.0	0.633	± 0.203	$^{+\ 0.086}_{-\ 0.081}$

Table 5.9: Differential cross sections of the 35m tagger in each $\eta(D^*)$ bin with the statistical and systematic errors.

W range [GeV]	$d\sigma/dW$ [nb/GeV]	stat	systematic
200.0 – 220.0	0.049	± 0.005	$^{+\ 0.006}_{-\ 0.005}$
220.0 – 240.0	0.063	± 0.006	$^{+\ 0.006}_{-\ 0.007}$
240.0 – 260.0	0.039	± 0.007	$^{+\ 0.005}_{-\ 0.007}$

Table 5.10: Differential cross sections of the 35m tagger in each W bin with the statistical and systematic errors.

	central value	stat	systematic
$\sigma^{44m}(ep \to D^*X)$ $[nb]$	7.10	$\pm$ 0.39	$^{+\ 0.13}_{-\ 0.18}$
$\sigma^{35m}(ep \to D^*X)$ $[nb]$	2.99	$\pm$ 0.29	$^{+\ 0.29}_{-\ 0.27}$
$\sigma^{44m}(\gamma p \to c\bar{c}X)$ $[\mu$b$]$	4.16	$\pm$ 0.22	$^{+\ 0.31\ +\ 1.82}_{-\ 0.38\ -\ 1.04}$
$\sigma^{35m}(\gamma p \to c\bar{c}X)$ $[\mu$b$]$	8.75	$\pm$ 0.76	$^{+\ 0.87\ +\ 3.89}_{-\ 0.90\ -\ 2.22}$

Table 5.11: Total charm and total visible D^* cross sections with the statistical ans systematic errors. For the total charm cross sections the first systematic error comes from the systematics of the data and the second systematical error comes from the extrapolation uncertainty.

Chapter 6

Results and Discussion

In this chapter comparisons between data cross sections and the leading order (LO) MC cross sections as well as next-to-leading order (NLO) calculations are presented. The results are discussed and compared and with previous experimental measurements.

6.1 Comparison of Data Cross Sections with MC Cross Sections

The differential cross sections are first compared with the leading order (LO) MC cross sections, using the HERWIG MC. Calculated MC cross sections are normalised to the data with normalisation factors $f_{35} = 1.47$ and $f_{44} = 1.23$ for the 44m tagger and the 35m tagger respectively.

Fig. 6.1 shows the differential D* cross sections for the 44m tagger as a function of $p_T(D^*)$, $\eta(D^*)$ and W compared with the LO predictions. The $p_t(D^*)$ and $\eta(D*)$ cross-section distributions in the Monte Carlo appear to largely agree with the data. Although there may be a slight excess in the MC in the rear direction. The MC does not agree with data in case of the W distribution. In the W cross-section distribution the data are clearly falling while the MC appears be flat.

In Fig. 6.2 the differential D* cross sections for the 35m tagger as a function of $p_T(D^*)$, $\eta(D^*)$ and W are compared with the LO predictions. The $p_t(D^*)$ and $\eta(D*)$ distributions in the Monte Carlo agree reasonably well with the data. For the W distribution agreement with the shape is¡not good, but the uncertainties in the data are large.

6.2 Comparison of Data Cross Sections with NLO Calculations

Measured differential and visible total cross sections are also compared with the NLO QCD predictions performed in the massive scheme. For that the FMNR FORTRAN code developed by Frixione [24] is used. The calculation is performed separately for direct and resolved processes and summed at the end. A detailed description of the FMNR program is in Sec. 3.3.

The theoretical predictions are calculated in the same kinematic region of $p_T(D^*), \eta(D^*), Q^2$ and W as the measurements. Cuts on D^* quantities $(p_T(D^*), \eta(D^*))$ are applied by calculating the $D^*(\bar{D}^*)$ momentum from the c $(\bar{c})$ quark momentum using the Peterson function with the parameter $\epsilon = 0.035$ [54]. The value of the Peterson parameter was obtained from an NLO fit to the factorisation measured by the ARGUS experiment [73]. The cross section for $ep \longrightarrow D^*X$ has been obtained from the calculated cross section $ep \longrightarrow cX$ by

$$\sigma(ep \longrightarrow D^*X) = 2f(c \longrightarrow D^*)\sigma(ep \longrightarrow cX), \tag{6.1}$$

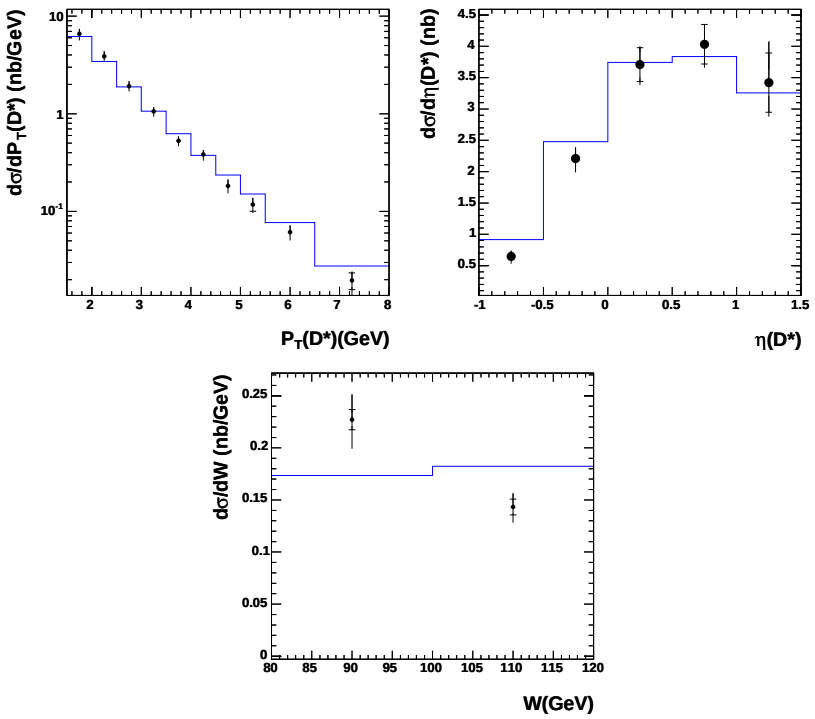

Figure 6.1: Measured cross sections in bins of $p_T(D^*)$ (top left plot), $\eta(D^*)$ (top right plot) and W (bottom plot) compared with the LO HERWIG MC prediction for the 44m analysis. Dots represent the data points and the line is the MC cross sections.

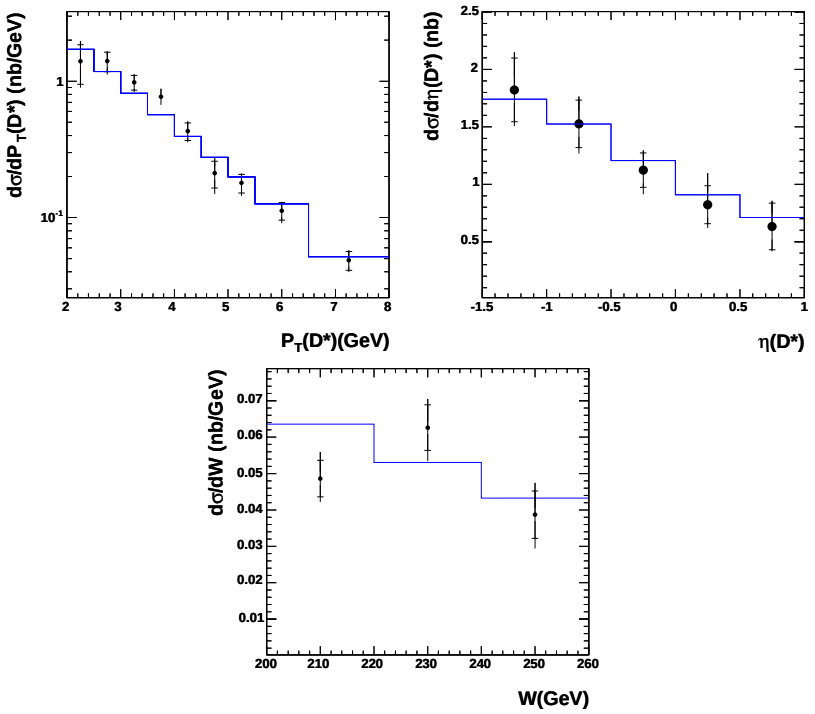

Figure 6.2: Measured cross sections in bins of $p_T(D^*)$ (top left plot), $\eta(D^*)$ (top right plot) and W (bottom plot) compared with the LO HERWIG MC prediction for the 35m analysis. Dots represent the data points and the line is the MC cross sections.

where $f(c \longrightarrow D^*)$ is the fragmentation fraction of the D^* meson. For this analysis the fragmentation fraction value is taken from the last ZEUS measurement [74], $f(c \longrightarrow D^*) = 20\%$. Changing the fragmentation fraction to the 23.5% [66] increases the theoretical predictions by about 15%. The factor two in the Eq. 6.1 is included because both c and $\bar{c}$ can fragment into D^{*+} or D^{*-}.

The theoretical NLO calculation are performed using CTEQ5M1 [75] for the proton and AFG-G HO [76] for the photon PDF sets. The renormalisation scale μ_R and factorisation scales of proton $\mu_{F,p}$ and the photon $\mu_{F,\gamma}$ are taken as

$$\mu_R^2 = \mu_{F,p}^2 = \mu_{F,\gamma}^2 = \mu_0^2 = m_c^2 + \langle p_T \rangle^2, \tag{6.2}$$

where $\langle p_T \rangle^2$ is the average squared transverse momentum of the charm quark. The nominal value for mass of the charm quark is taken as $m_c = 1.5\,\mathrm{GeV}/c^2$.

The estimation of the uncertainties on the theoretical prediction is done by changing the parameters used in the calculation, which are: the variation of the charm quark mass $1.3\,\mathrm{GeV} < m_C < 1.7\,\mathrm{GeV}$, in the range of results from the HERA photoproduction analyses [77], the variation of scales $0.25(p_T^2 + m_c^2) < \mu^2 < 4(p_T^2 + m_c^2)$, and the variation of the Peterson fragmentation function $0.028 < \epsilon < 0.042$. Changing the photon PDF to GRV-G HO [21] loweres the cross section by $\approx 5\%$. The largest contributions to the theoretical uncertainty come from the variation of charm mass and scale.

In Fig. 6.3 the differential cross sections $d\sigma/dp_t(D^*)$, $d\sigma/d\eta(D^*)$ and $d\sigma/dW$ as a function of $p_T(D^*)$, $\eta(D^*)$ and W respectively are compared with the theroetical predictions for the 44m tagger. Within the very large theoretical uncertainties the NLO preditions agree with the data. However the shape of $\eta(D^*)$ distribution is not well reproduced by QCD NLO calculation. The shape of p_t cross section of the theoretical prediction agrees with the data, but $\eta(D^*)$ cross-section is clearly underestimated in the forward region and overestimated in the backward region. In the W cross-section distribution the data falls more steeply than in the theoretical calculation.

In Fig. 6.4 the differential cross sections $d\sigma/dp_t(D^*)$, $d\sigma/d\eta(D^*)$ and $d\sigma/dW$ as a function of $p_T(D^*)$, $\eta(D^*)$ and W respectively are compared with the theoetical predictions for the 35m tagger. The agree well. But the shape of $p_t(D^*)$ and W distributions are a bit different, but the theoretical and data uncertainties are also large.

The FMNR calculation for the total visible region of 44m tagger yields:

$$\sigma_{tot,ep}^{FMNR}(D^* \longrightarrow K\pi\pi) = 7.3^{+6.5}_{-2.6}(th.syst)\ \mathrm{nb}, \tag{6.3}$$

and for total visible region of 35m tagger:

$$\sigma_{tot,ep}^{FMNR}(D^* \longrightarrow K\pi\pi) = 2.32^{+1.8}_{-0.8}(th.syst)\ \mathrm{nb}. \tag{6.4}$$

The total visible cross sections in the restricted (p_t, η, W) range are defined in the Section 5.2.1. The uncertainty of the theory is much greater than the uncertainty of the measurement, and the central value of the theory lies below the data, but within the large uncertainties they are consistent.

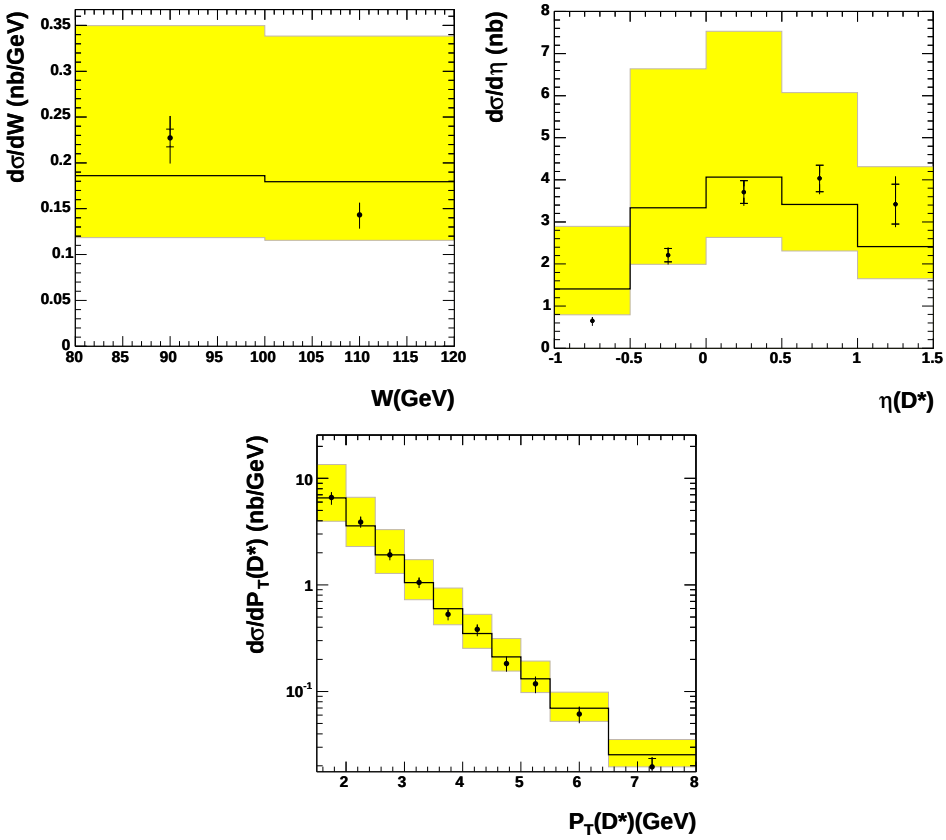

Figure 6.3: Measured differential cross section in bins of W (top-left), $\eta(D^*)$ (top-right) and $p_T(D^*)$ (bottom) compared with the FMNR NLO QCD predictions for the 44m tagger analysis. Data are represented by points. The black line is the NLO predictions with nominal parameters. The coloured area indicates the theoretical uncertainties obtained by variation of the FMNR parameters described in the Sec. 6.2.

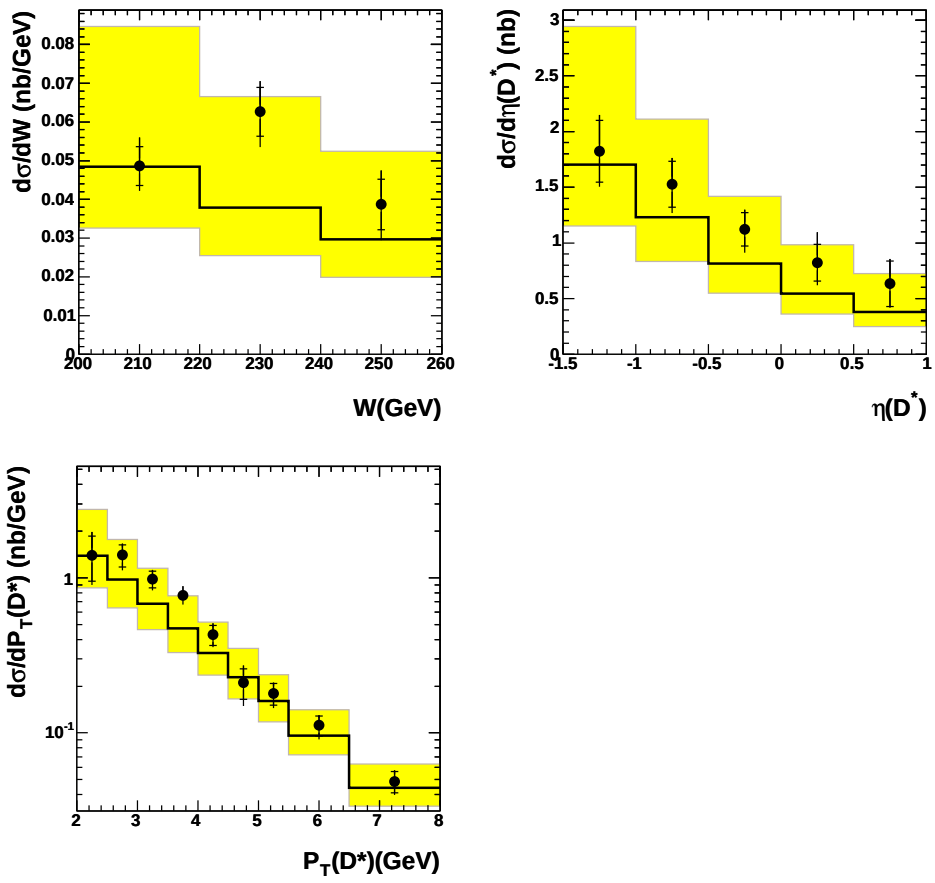

Figure 6.4: Measured differential cross section in bins of W (top-left), $\eta(D^*)$ (top-right) and $p_T(D^*)$ (bottom) compared with the FMNR NLO QCD predictions for the 35m tagger analysis. Data are represented by points. The black line is the NLO predictions with nominal parameters. The coloured area indicates the theoretical uncertainties obtained by variation of the FMNR parameters described in the Sec. 6.2.

6.3 Comparison of the 44m Tagger Results with Previous Analyses

The ZEUS preliminary results for D^* production via $K\pi\pi_s$ decay using the 44m tagger are shown in Fig. 6.5, [33, 71]. These measurements were made using the datasets from 1996 and 1997 with an integrated luminosity of $L = 16.6\text{pb}^{-1}$ at a centre-of-mass energy of $\sqrt{s} = 300\,\text{GeV}$. The kinematic region of this analyses is the same except the $p_T(D^*)$ region, $2.0 < p_T(D^*) < 8$ GeV. In our case the trigger configuration allows to go down in $p_T(D^*)$ to 1.5 GeV.

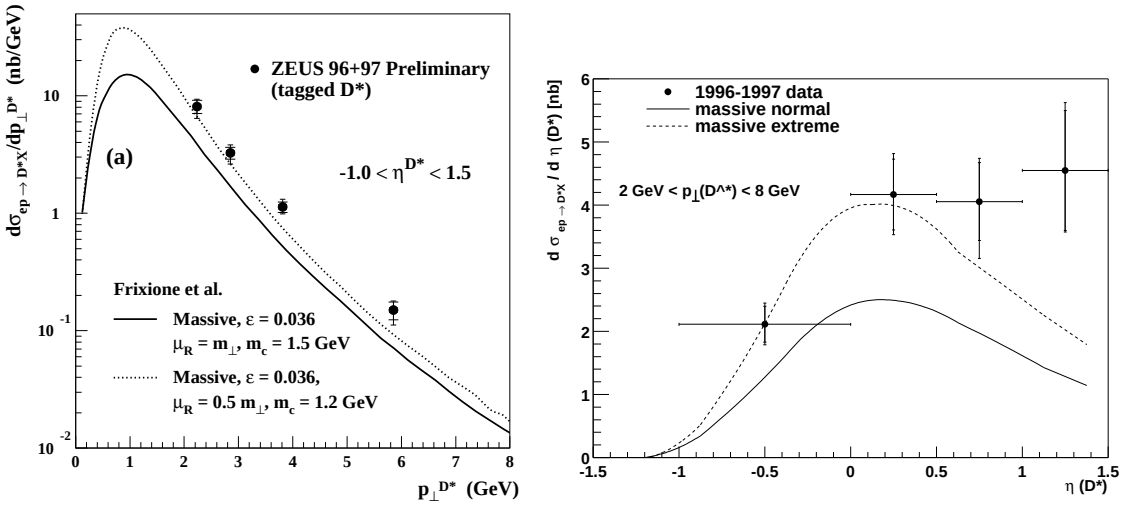

Figure 6.5: Differential cross sections $d\sigma/dp_T(D^*)$ (on left plot) and $d\sigma/d\eta(D^*)$ (on the right plot) for $-1.0 < \eta(D^*) < 1.5$, $2.0 < p_T(D^*) < 8$ GeV, $80 < W < 120$ GeV, $Q^2 < 0.015$ GeV^2. The filled circles show the data and the full line shows the predictions of QCD calculation obtained by FMNR program with the default parameters $\epsilon = 0.036, \mu_R = \mu_\perp, m_c = 1.5$ GeV. The dashed line represents the extreme settings $\epsilon = 0.036, \mu_R = 0.5\mu_\perp, m_c = 1.2$ GeV.

Comparing with the 1996 - 1997 results, the measurements in this thesis have higher statistics (about 5 times more) and are done more differentially. The comparison of 96-97 data with the massive QCD NLO calculations, which is done by the same FMNR program as for this thesis, shows that for the differential cross sections of $p_T(D^*)$ the data points are much higher than the calculation with the central (default) parameters (solid line), Fig. 6.5 (left plot). Better agreement is achieved by changing default parameters within the limits recommended by the authors (extreme case). However even with the extreme parameters the data points are still higher than the calculations (dashed line) in particular at high $p_T(D^*)$. The comparison of the data and the QCD NLO calculations for the analysis described in this thesis, 1998 - 2000 datasets, shows good agreement within the errors, Fig. 6.3 (bottom plot). The central (default) theoretical predictions agree well with the data points. In both the old and new datasets cases the shape of theoretical predictions and the data points agrees well.

The comparison of differential cross sections as a function of $\eta(D^*)$ for the 1996 - 1997 data with the QCD NLO calculations shows that neither of the two massive calculations (solid line for default and dashed line for extreme case) is in agreement with the data, Fig. 6.5 (right plot). For negative $\eta(D^*)$ the calculation with extreme parameters describes the data, but in the forward direction it is significantly below the data. The comparison of the $\eta(D^*)$ differential cross sections of 1998 - 2000 datasets shows a good agreement within the systematical

uncertainties. For negative $\eta(D^*)$ the data point are below the central predictions, while in the forward region they are a bit high. In both old and the new datasets the shape of the theoretical predictions does not really describe the data. The excess in the forward region of the $\eta(D^*)$ cross sections is also observed in the previous untagged ZEUS measurements [71, 78, 79]. For example, Fig. 6.6 shows the $\eta(D^*)$ results from ZEUS inclusive measurements. This analysis is similar to the one shown in this thesis but covers a different W region, $130 < W < 250\,\text{GeV}$. In this analysis no identification of the scattered electron is required. The selection of photoproduction events is done by rejecting all events where an electron was found in the main calorimeter (untagged photoproduction). The minimal $p_T(D^*)$ is given in each plot. For $p_T(D^*) > 3.25\,\text{GeV}$ the calculations underestimate the cross section in the forward direction.

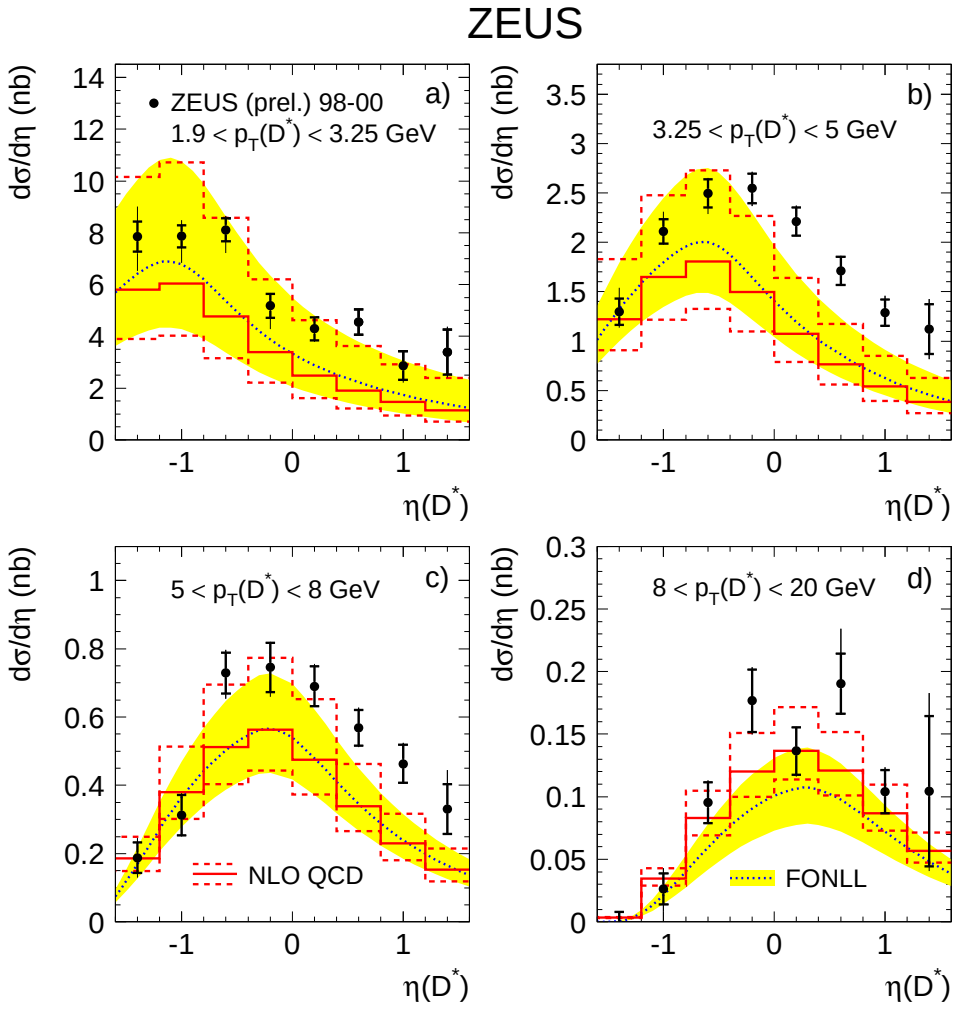

Figure 6.6: Differential cross sections $d\sigma/d\eta(D^*)$ for untagged photoproduction [79].

6.4 Comparison of the 35m Tagger Results with Previous Analyses

A very similar analysis of D^* production via $K\pi\pi_s$ mode in photoproduction was made by the H1 Collaboration at HERA [80, 81]. The analysis was performed with data taken in the 1999 and 2000 running periods with an integrated luminosiy $L = 49.2\text{pb}^{-1}$. Photoproduction events were selected by detecting of the scattered electron in an dedicated electron tagger close to the beampipe, 33m away from the interaction point. The kinematic range of the analysis is $Q^2 < 0.01\,\text{GeV}^2$, $171 < W < 256\,\text{GeV}$, $p_T(D^*) > 2.5\,\text{GeV}$ and $|\eta(D^*)| < 1.5$. The differential cross sections $d\sigma/dp_T$, $d\sigma/d\eta$ and $d\sigma/W$ are shown in Fig. 6.7. The measured cross sections are compared with the QCD NLO calculations. The calculations were done with the same FMNR Fortran program ("massless" scheme), which was used for this thesis, using the CTEQ5D [75] proton parton density and GRV-G HO [21] photon parton density parametrisation with the default parameters: Peterson fragmentation function $\epsilon_{pet} = 0.035$,

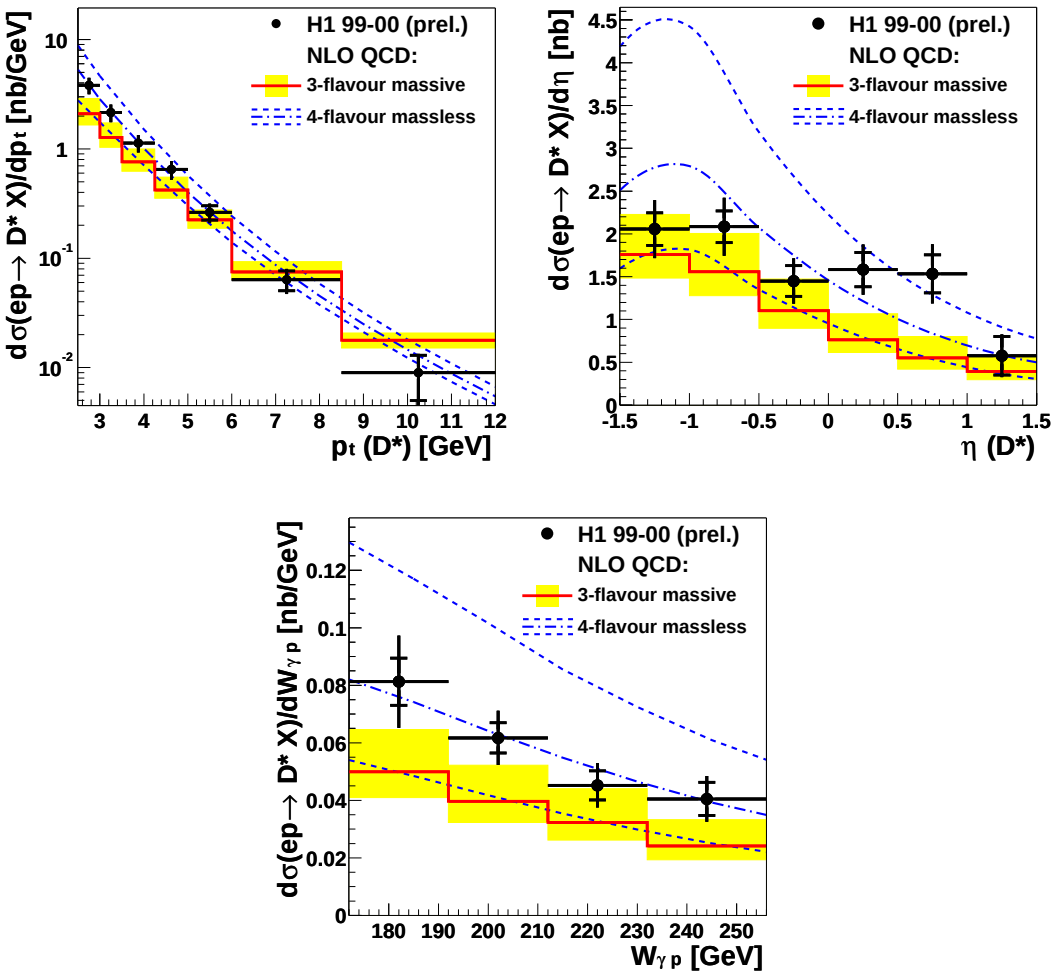

Figure 6.7: Differential D^*-photoproduction cross sections $d\sigma/dp_T$, $d\sigma/d\eta(D^*)$ and $d\sigma/W$ in the kinematic range $Q^2 < 0.01\,\text{GeV}^2$, $171 < W < 256\,\text{GeV}$, $p_T(D^*) > 2.5\,\text{GeV}$ and $|\eta(D^*)| < 1.5$ taken from [80]. The data are shown as points. The data compared with NLO QCD calculations (FMNR programm): the solid line represent a prediction with the central parameters, and the band is the theoretical uncertainties.

renormalisation and factorisation sacles $2\mu_R = \mu_{F,p} = \mu_{F,\gamma} = 2\sqrt{m_c^2 + \langle p_T \rangle^2}$.

For direct comparison with the H1 results, the analysis with the 35m dataset described in this thesis was redone for the H1 kinematic region of $p_T(D^*)$, $\eta(D^*)$ and Q^2. Fig. 6.8 the differential cross sections $d\sigma/W$ compared with the QCD NLO calculations are shown. The left plot shows the 35m tagger cross section compared with the H1 33m tagger cross section and theoretical predictions, calculated with the GRV-G HO photon parton density function (PDF) for the H1 kinematic region. The right plot shows the H1 33m tagger cross sections compared with the 35m tagger cross sections and theoretical predictions, calculated with the AFG-G HO photon parton density function for the kinematic region of 35m tagger. The theoretical prediction parameters are slightly different for the central and extreme cases and are summarised in Table 6.1.

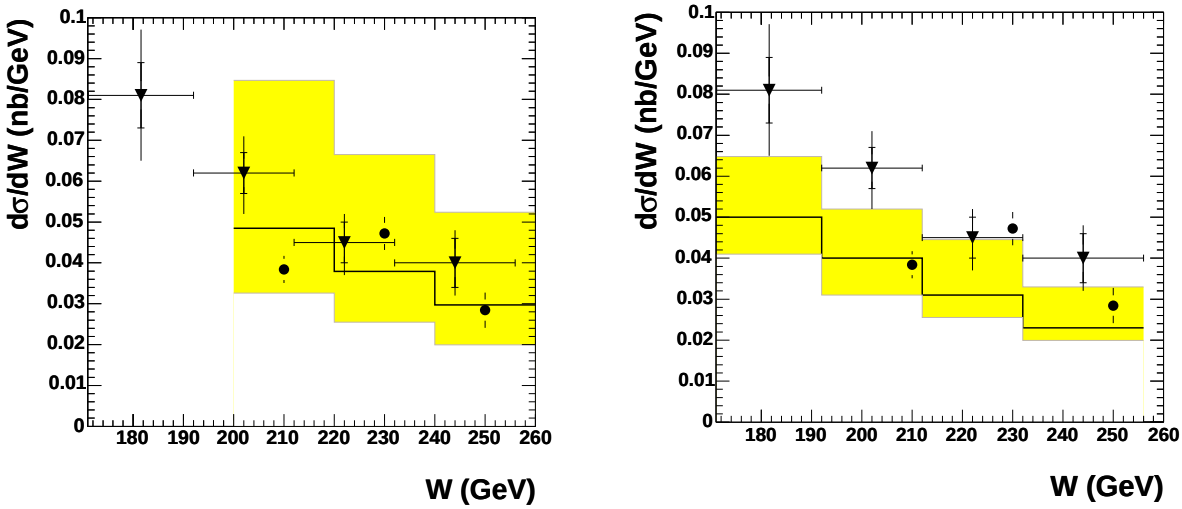

Figure 6.8: Differential cross section $d\sigma/dW$ (nb/ GeV) as a function of W of 35m tagger (points) comparing to the H1 cross sections (triangles). On the left plot the data are compared with the QCD NLO predictions with GRV-G HO photon parton density function calculated by H1, on the right plot the same data are compared with thetheoretical predictions calculated with AFG-G HO parton density function. The bold line is the NLO predictions with the central parameters, while the yellow band shows the sytematic uncertainties in the theory, see Table 6.1.

	FMNR	p-PDF	γ-PDF	m_c [GeV]	μ_R	μ_F	ϵ
35m (44m)[1] analysis	decreasing σ	CTEQ5M	AFG-G HO	1.7	$2{\cdot}m_T$	m_T	0.042
	default			1.5	m_T	m_T	0.035
	increasing σ			1.3	$0.5{\cdot}m_T$	m_T	0.028
33m analysis (H1)	decreasing σ	CTEQ5M	GRV-G HO	1.7	$2{\cdot}m_T$	m_T	0.042
	default			1.5	m_T	$2{\cdot}m_T$	0.035
	increasing σ			1.3	$0.5{\cdot}m_T$	$4{\cdot}m_T$	0.028

Table 6.1: Renormalisation (μ_R) and factorisation (μ_F) scales, the charm mass (m_c), the Peterson parameters (ϵ) and the parton density parametrisations of the D^* cross section calculation with the FMNR program with the default settings and variations for both 35m (44m) and 33m tagger analyses. The transverse mass is defined as $m_T = \sqrt{m_c^2 + \langle p_T \rangle^2}$.

[1]The same parameters are used for the theoretical calculations for 44m tagger analysis.

The FMNR calculations describe both the 35m and the 33m data quite well within the large theoretical uncertainties.

6.5 Comparison of 35m and 44m Tagger Analysis.

The difference between the 44m and 35m taggers analysis is largely the different W kinematic region. The 44m tagger analysis covers a lower W region, $80 < W < 120\,\text{GeV}$ than the 35m tagger, $200 < W < 260\,\text{GeV}$. The effect of this can be seen in the distribution of the differential cross section $d\sigma/d\eta(D^*)$ as a function of $\eta(D^*)$, see Fig. 6.9. The effect is that in the lower W kinematic region the photoproduction of D^* mesons mostly produced in the forward region (left plot), and in higher W kinematic region the production is boosted to the backward region (right plot). This can be understood because W is correlated with y and low-y events tends to be more boosted in the forward direction.

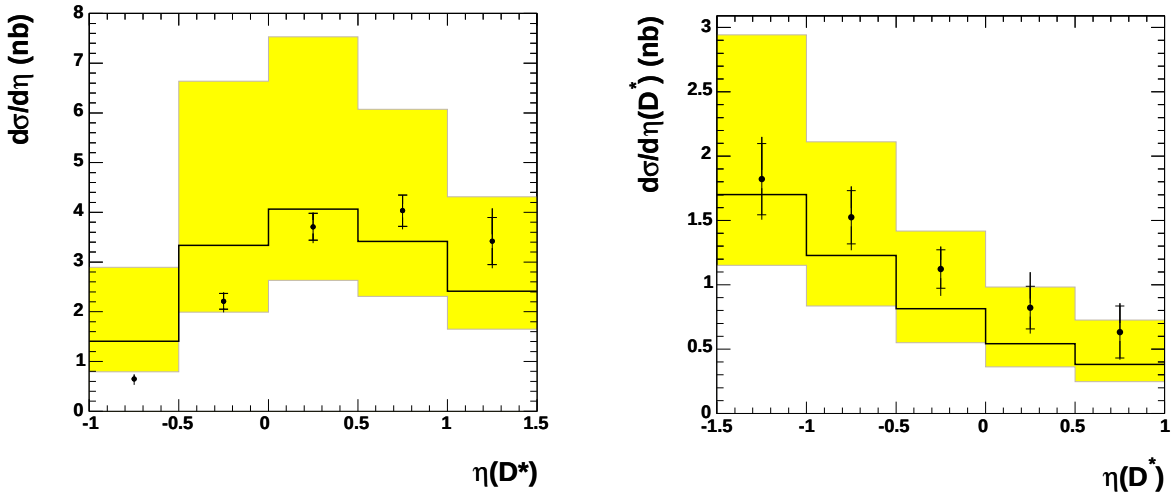

Figure 6.9: Diffrential cross sections $d\sigma/d\eta$ (nb) as a function of $\eta(D^*)$ for different W kinematic region. On the left plot the results from 44m tagger analysis with $80 < W < 120\,\text{GeV}$ are shown, and on the right plot the results from the 35m tagger analysis with the $200 < W < 260\,\text{GeV}$ are shown.

.

The fact that there are more events in the data than in NLO calculations might suggests that there are more events in low-W case than in the NLO calculations. In the case of the 35m tagger there are more events over all in whole kinematic range. Because the shape of the 35m tagger distribution all agree this supports that the normalisation of NLO calculation is low. A lower charm mass quark could lead to better agreement.

In the Fig. 6.10 the differential cross sections $d\sigma/dW$ as a function of W for both analysis are presented. The cross sections falls with the rising of W. Such a behaviour is expected in the theory. The difference in the theoretical uncertainties (yellow band) comes from the fact that the analysis have slightly different Q^2 regions: 44m tagger has $Q^2 < 0.015\,\text{GeV}^2$, and 35m tagger has $Q^2 < 0.02\,\text{GeV}^2$.

The differential cross sections $d\sigma/dp_T$ as a function of $p_T(D^*)$ are similar in shape and well agree with the theoretical predictions.

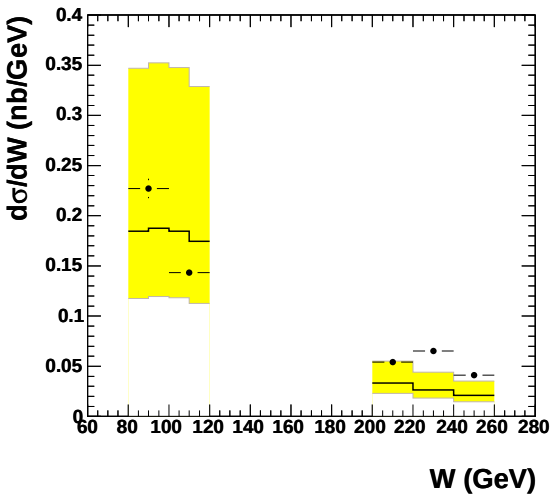

Figure 6.10: Diffrential cross sections $d\sigma/dW$ (nb/ GeV) as a function of W. On the left are the results from the 44m tagger and on the right the 35m tagger analysis are shown respectively.

.

6.6 Comparison of the Total Charm Photoproduction Cross Sections with the NLO Predictions

The analysis with the 44m tagger extends previous HERA and fixed target experiments measurements of the total charm cross sections in the full kinematic region in photoproduction. Both measured cross sections with the 44m and 35m taggers are observed in a restricted W region. The extrapolation procedure to the of visible cross sections to the cross sections in the full phase space can be found in Seq. 5.2.3.

In Fig. 6.11 the comparison of results (filled triangles) with the previous HERA measurements as well as with the fixed target experiments measurements at lower energies and NLO calculations is presented. The inner error bar shows the statistical uncertainty, the middle bar shows the experimental systematic and statistical uncertainty added in quadrature, and the outer bar (with no tick mark) shows the experimental statistical and systematic uncertainty added in quadrature with the theoretical systematic uncertainty from the extrapolation.

The data are in a good agreement with the theoretical predictions.

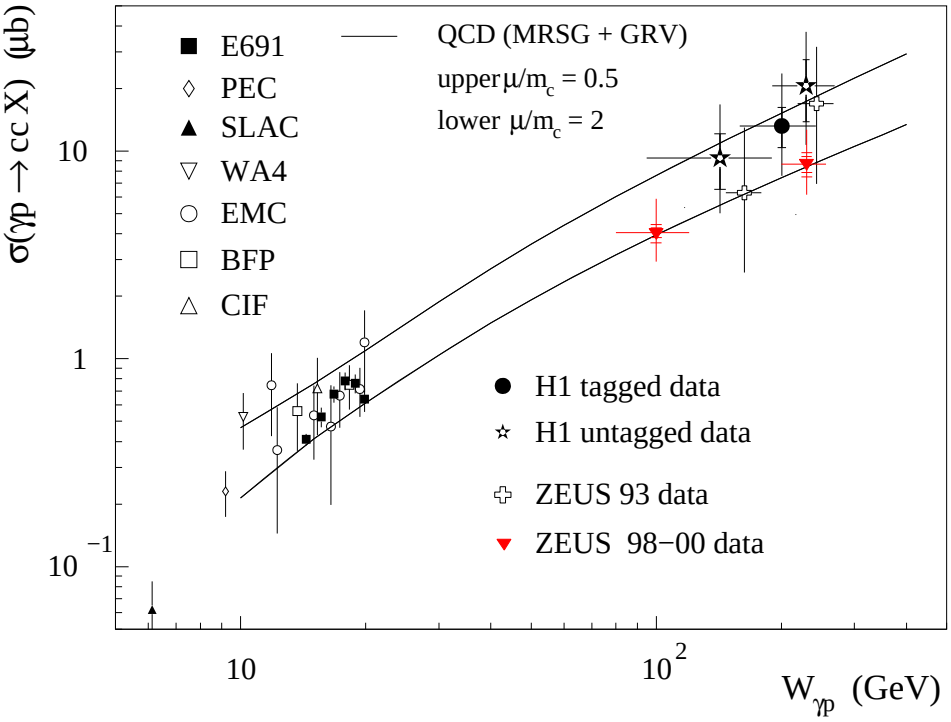

Figure 6.11: Total charm photoproduction cross-sections as a function of $W_{\gamma p}$. The solid crosses represent the present analysis. The empty crosses indicate previous ZEUS results, the solid stars and dots indicates the H1 collaboration results. All other symbols indicate results from lower energy fixed target experiments. The solid lines represent the prediction of a NLO QCS calculation using the MRSG and GRV-G HO parametrisation of the proton and photon PDF, respectively. The upper and lower lines delimit the range of values from varying the renormalisation scale within $0.5 < \mu/m_c < 2$.

Chapter 7

Summary and Conclusions

In this thesis a study of the $D^{*\pm}$ meson photoproduction and the total charm photoproduction in electron proton scattering at HERA has been presented. The data taken with the ZEUS detector at HERA in the running period 1998 - 2000 with an integrated luminosity of $L = 81.5\,\mathrm{pb}^{-1}$ for the 44m data sample and $L = 80.7\,\mathrm{pb}^{-1}$ for the 35m data sample have been analysed. The D^* visible and differential cross sections as well as the total charm cross sections have been measured and compared to NLO QCD predictions.

Photoproduction events were selected by requiring the identification of the scattered electron in the dedicated taggers, 44m and 35m away from the interaction point. Due to the geometrical position of the taggers the invariant mass of the γp system, W, and Q^2 are limited to:

- **for 44m tagger** $80\,\mathrm{GeV} < W < 120\,\mathrm{GeV}, \qquad Q^2 < 0.015\,\mathrm{GeV},$
- **for 35m tagger** $200\,\mathrm{GeV} < W < 260\,\mathrm{GeV}, \qquad Q^2 < 0.02\,\mathrm{GeV},$

for the 44m and 35m tagger respectively.

Charm photoproduction was identified by reconstructing a D^* meson via $D^{*\pm} \longrightarrow K^{\mp}\pi^{\pm}\pi_s^{\pm}$ mode together with a tagged scattered electron. Due to the detector geometry and acceptance effects the kinematic region was limited in the pseudorapidity and transverse momenta of the D^* meson to:

- **for 44m tagger** $-1.0 < \eta(D^*) < 1.5, \qquad p_T(D^*) > 1.5\,\mathrm{GeV}$
- **for 35m tagger** $-1.5 < \eta(D^*) < 1.0, \qquad p_T(D^*) > 2.0\,\mathrm{GeV}$

The total visible and differential cross section of the process:

$$ep \longrightarrow ec\bar{c}X \longrightarrow eD^*Y$$

has been evaluated in the phase space limited in $W, Q^2, p_t(D*)$ and $\eta(D^*)$ for both the 44m and 35m taggers and compared to the NLO QCD calculations using the FMNR program, which simulates the charm quark as a massive particle. The total cross section for centre-of-mass energy $\sqrt{s_{ep}} = 318\,\mathrm{GeV}$ for both the 44m and 35m taggers are measured:

$$\sigma^{44m}_{ep\to eD^*X} = 7.1 \pm 0.39(stat)^{+0.13}_{-0.18}(syst)\,\mathrm{nb},$$

$$\sigma^{35m}_{ep\to eD^*X} = 2.99 \pm 0.29(stat)^{+0.29}_{-0.27}(syst)\,\mathrm{nb}.$$

The comparison of differential cross section $d\sigma_{ep\to eD^*X}/dp_t(D^*)$ with theoretical predictions shows good agreement within the uncertainties. The differential cross section of $d\sigma_{ep\to eD^*X}/d\eta(D^*)$

for the 44m tagger shows that the NLO QCD calculation underestimates the cross sections in the forward region of pseudorapidity, which was also observed in previous photoproduction measurements at HERA. By comparison of the cross sections as a function of $\eta(D^*)$ one can see how the D^* production is boosted with the changing of the W kinematic region. Fig. 6.9 shows that in lower W kinematic region the D^* mostly produced in the forward region, while in higher W region the production is boosted to the backward region.

The total charm photoproduction cross sections in the new intermediate kinematic region, $80\,\text{GeV} < W_{44m} < 120\,\text{GeV}$, between fixed-target and HERA measurements, not studied before, as well as in an overlapping region with the previous HERA measurements, $200\,\text{GeV} < W_{35m} < 260\,\text{GeV}$, are:

$$\sigma^{44m}_{\gamma p \to c\bar{c}X} = 4.16 \pm 0.22(stat)^{+0.31}_{-0.38}(exp.syst)^{+1.82}_{-1.04}(theor.syst)\ \mu\text{b},$$

$$\sigma^{35m}_{\gamma p \to c\bar{c}X} = 8.75 \pm 0.76(stat)^{+0.87}_{-0.90}(exp.syst)^{+3.89}_{-2.22}(theor.syst)\ \mu\text{b}.$$

and compared to the NLO QCD calculation and previous HERA and fixed-target experimental results. The comparison shows that the NLO prediction describe the data within the theoretical uncertainties. The measured cross sections falling with the decreasing W, as predicted by the theory, see Fig. 6.11.

Appendix A

Control Plots

In this Appendix ΔM distributions for each bin of the differential cross section of p_T, η, W in the Monte Carlo for both the 44m and the 35m samples are presented, Fig. A.1 -A.6.

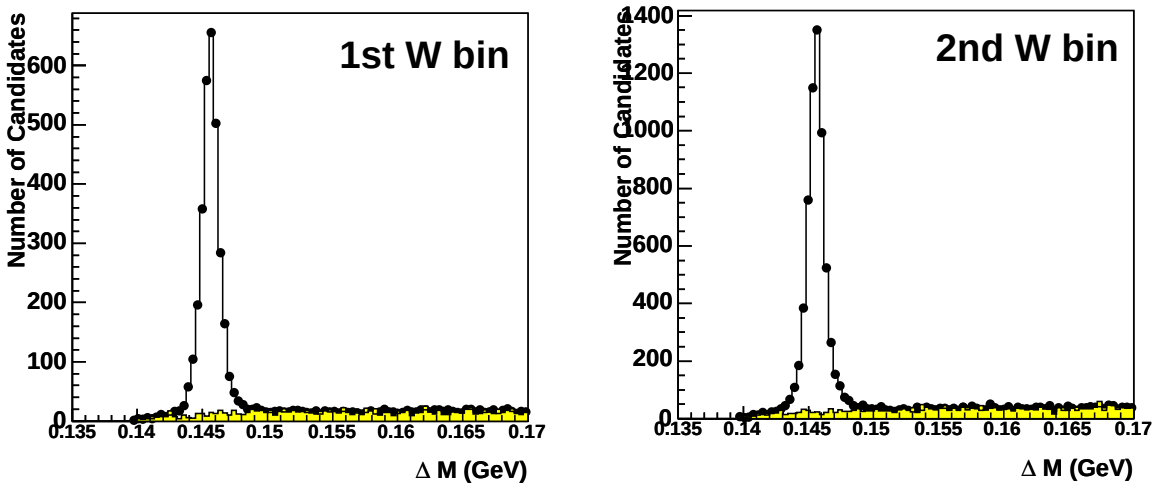

Figure A.1: ΔM distributions for each bin of W cross section of 44m Monte Carlo sample. The background distributions are already normalised in the control region. The points represent the correct charge combinations of the D^* candidates and the filled histograms represent the wrong charge combinations of D^* candidates.

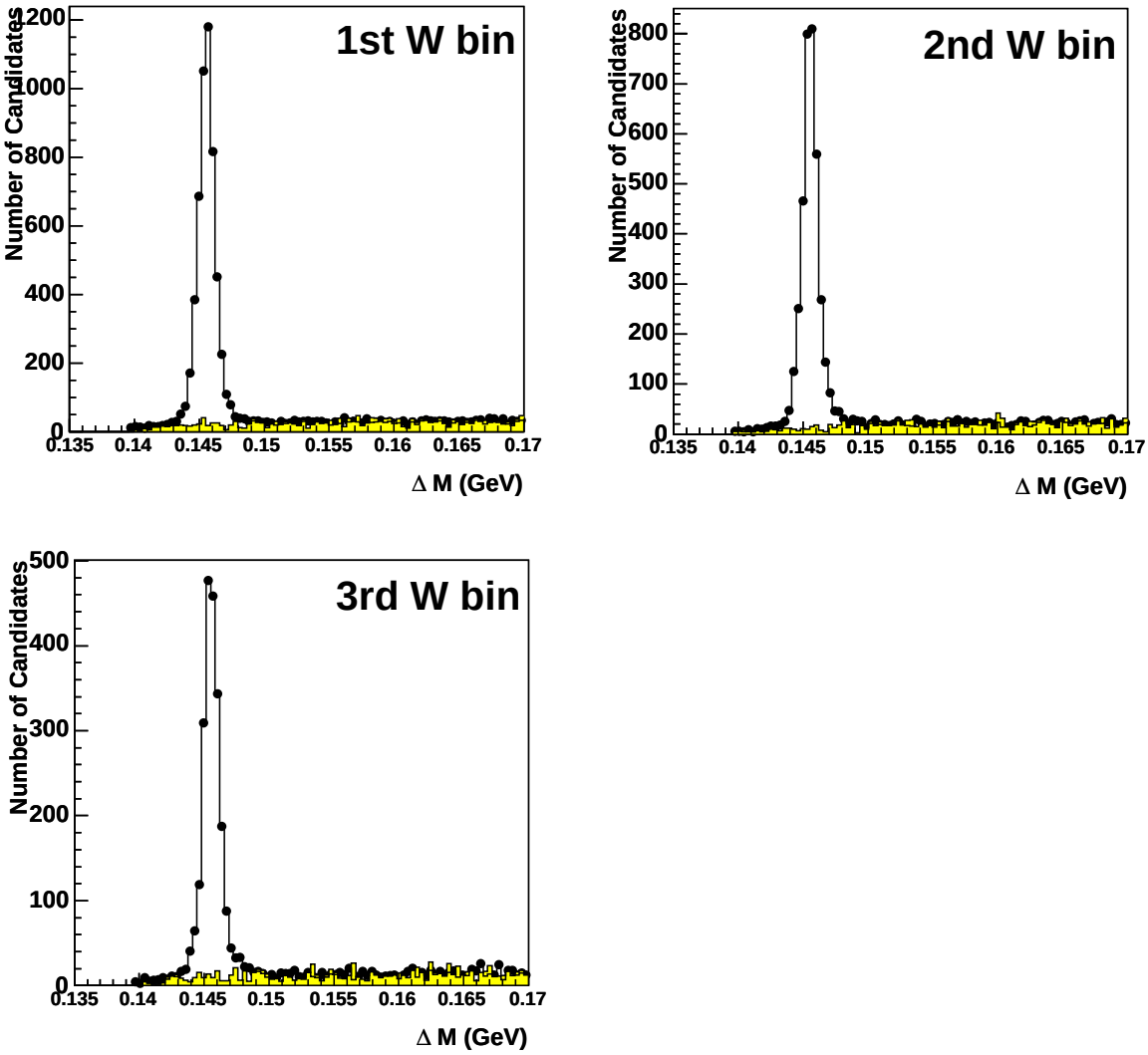

Figure A.2: ΔM distributions for each bin of W cross section of 35m Monte Carlo sample. The background distributions are already normalised in the control region. The points represent the correct charge combinations of the D^* candidates and the filled histograms represent the wrong charge combinations of D^* candidates.

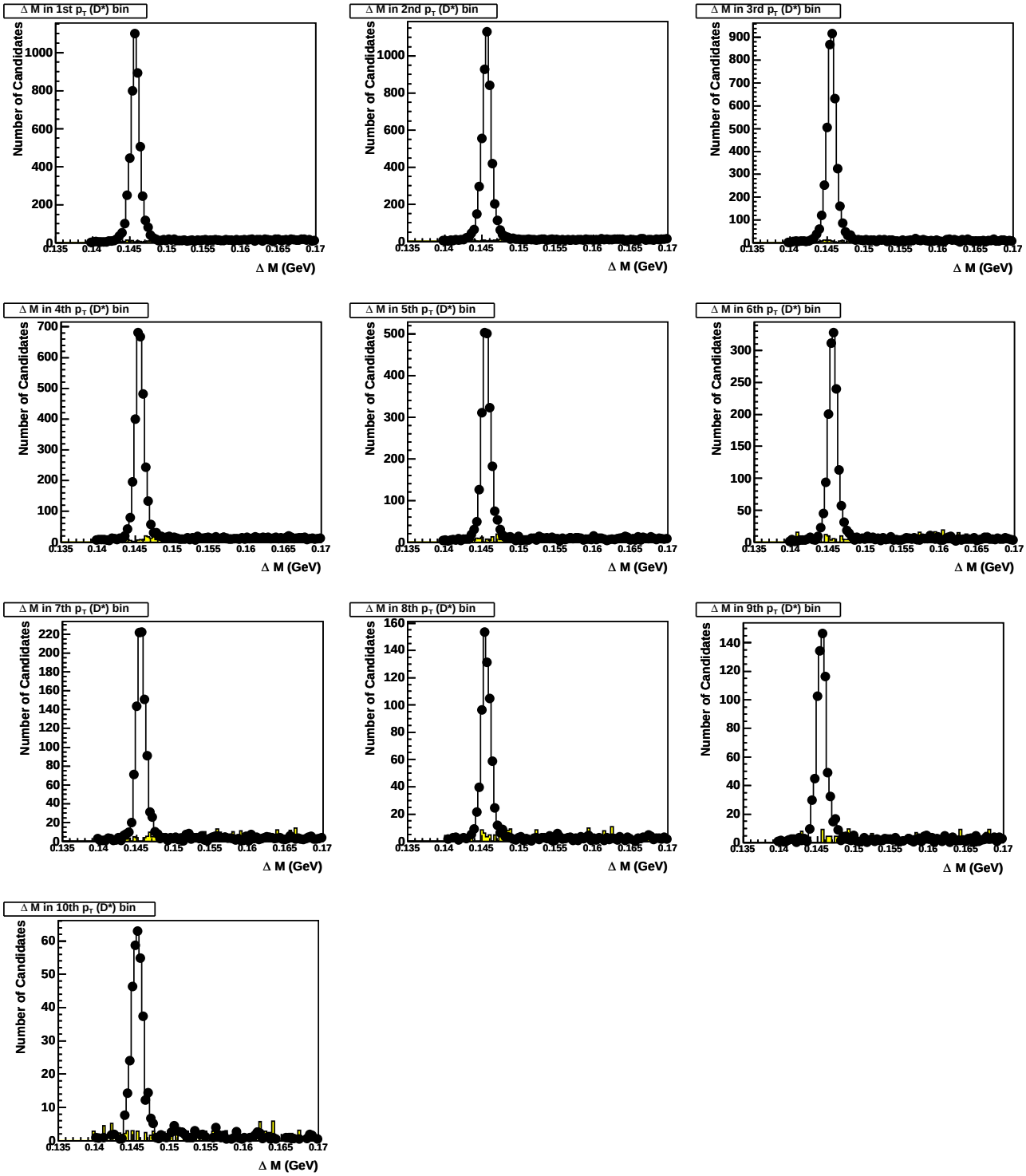

Figure A.3: ΔM distributions for each bin of $p_T(D^*)$ for the 44m Monte Carlo sample. The background distributions from the wrong-charge contributions are normalised in the control region $0.143 < \Delta M < 1.92\,\text{GeV}$. The points represent the correct charge combinations of the D^* candidates and the filled histograms represent the wrong charge combinations of D^* candidates.

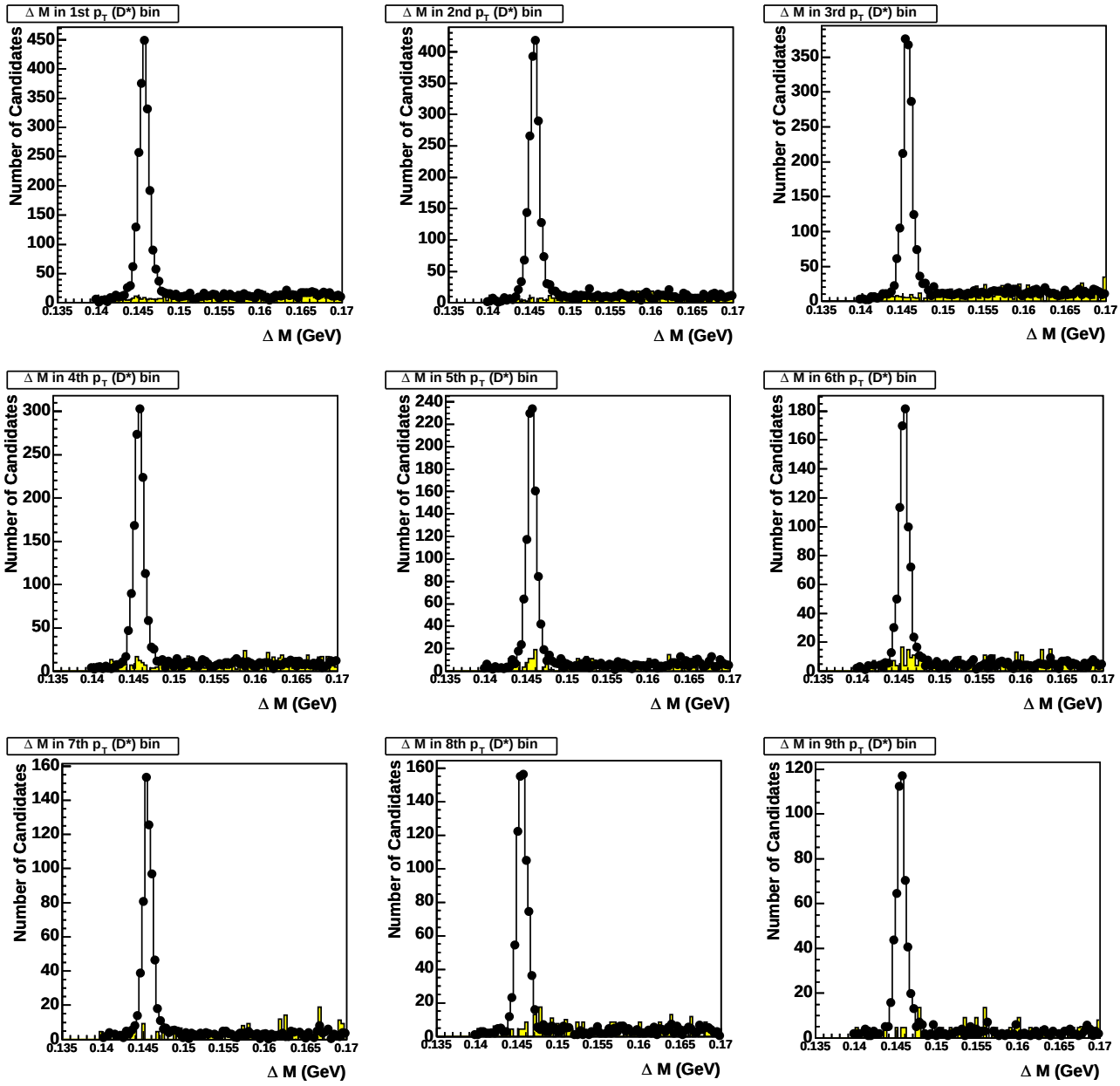

Figure A.4: ΔM distributions for each bin of $p_T(D^*)$ for the of 35m Monte Carlo sample. The background distributions from the wrong-charge contributions are normalised in the control region $0.143 < \Delta M < 1.92\,\text{GeV}$. The points represent the correct charge combinations of the D^* candidates and the filled histograms represent the wrong charge combinations of D^* candidates.

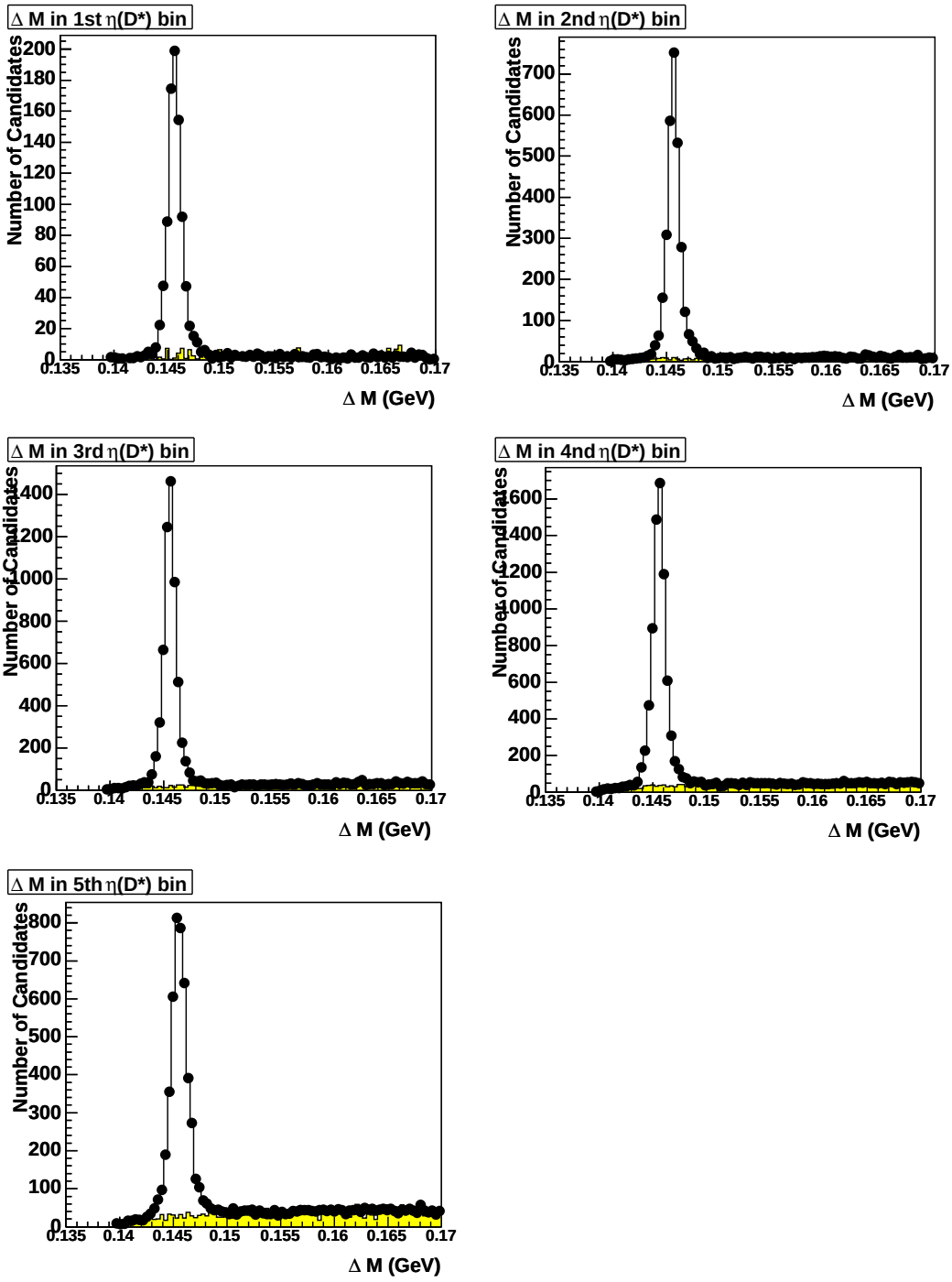

Figure A.5: ΔM distributions for each bin of $\eta(D^*)$ cross section of 44m Monte Carlo sample. The background distributions are already normalised in the control region. The points represent the correct charge combinations of the D^* candidates and the filled histograms represent the wrong charge combinations of D^* candidates.

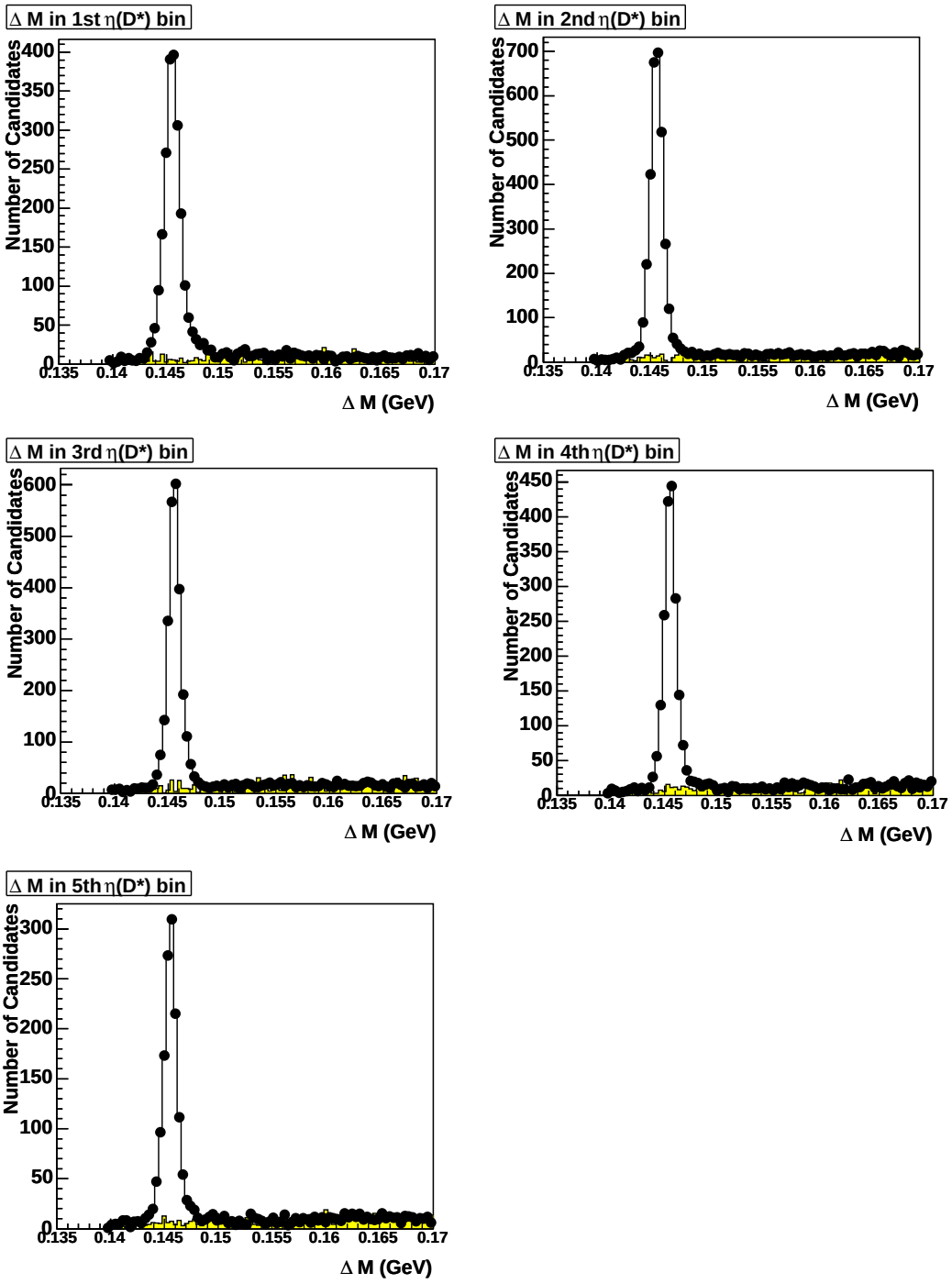

Figure A.6: ΔM distributions for each bin of $\eta(D^*)$ cross section of 35m Monte Carlo sample. The background distributions are already normalised in the control region. The points represent the correct charge combinations of the D^* candidates and the filled histograms represent the wrong charge combinations of D^* candidates.

Appendix B

Tables

In this Appendix the tabulated values of the D^* meson candidates with their errors are presented for each bin of differential cross section of $p_T(D^*)$, $\eta(D^*)$ and W in Tables B.1-B.6 for both the 44m and 35m samples. The procedure of the extracting the D^* candidates by subtracting the number of wrong-charge combination from the correct-charge combinations is described in Sec. 4.3.4. The calculated normalisation factor for the data used in this method is also presented in the tables. For the Monte Carlo the background is negligible, therefore the normalisation factor for simulated D^* candidates is not shown. In those bins where normalisation factor is large the statistical uncertainty is also large.

	p_T range [GeV]	$N^{DATA}(D^*)$	Norm. factor	$N^{MC}(D^*)$
1	1.5 - 2.0	630 ± 63	1.021	4593 ± 71
2	2.0 - 2.5	701 ± 49	1.001	4812 ± 72
3	2.5 - 3.0	524 ± 39	1.186	3998 ± 67
4	3.0 - 3.5	379 ± 27	1.247	2956 ± 64
5	3.5 - 4.0	233 ± 19	1.211	2137 ± 55
6	4.0 - 4.5	187 ± 16	1.487	1424 ± 45
7	4.5 - 5.0	97 ± 13	1.488	974 ± 38
8	5.0 - 5.5	64 ± 9	1.172	634 ± 32
9	5.5 - 6.5	68 ± 9	1.556	661 ± 34
10	6.5 - 8.0	30 ± 5	1.333	327 ± 21

Table B.1: Number of D^* candidates with the statistical error for each p_T bin of the differential cross section of the 44m sample.

	η range [GeV]	$N^{DATA}(D^*)$	Norm. factor	$N^{MC}(D^*)$
1	-1.5 - -1.0	78 ± 11	1.385	857 ± 31
2	-1.0 - -0.5	342 ± 24	1.285	2978 ± 57
3	-0.5 - 0.0	773 ± 56	1.105	6010 ± 132
4	0.0 - 0.5	1052 ± 83	1.058	7820 ± 128
5	0.5 - 1.0	691 ± 90	1.021	5012 ± 110

Table B.2: Number of D^* candidates with the statistical error for each η bin of the differential cross section of the 44m sample.

	W range [GeV]	$N^{DATA}(D^*)$	Norm. factor	$N^{MC}(D^*)$
1	80 - 100	1601 ± 68	1.022	9494 ± 104
2	100 - 120	1339 ± 71	1.076	13225 ± 124

Table B.3: Number of D^* candidates with the statistical error for each W bin of the differential cross section of the 44m sample.

	p_T range [GeV]	$N^{DATA}(D^*)$	Norm. factor	$N^{MC}(D^*)$
1	2.0 - 2.5	193 ± 62	1.071	1987 ± 48
2	2.5 - 3.0	263 ± 42	1.101	1855 ± 47
3	3.0 - 3.5	236 ± 29	1.031	1651 ± 48
4	3.5 - 4.0	208 ± 20	0.928	1295 ± 43
5	4.0 - 4.5	123 ± 18	1.304	947 ± 40
6	4.5 - 5.0	64 ± 14	1.459	704 ± 38
7	5.0 - 5.5	63 ± 9	0.904	587 ± 29
8	5.5 - 6.5	76 ± 11	1.222	720 ± 35
9	6.5 - 8.0	55 ± 8	1.350	491 ± 27

Table B.4: Number of D^* candidates with the statistical error for each p_T bin of the differential cross section of the 35m sample.

	η range	$N^{DATA}(D^*)$	Norm. factor	$N^{MC}(D^*)$
1	-1.5 - -1.0	286 ± 41	1.119	1034 ± 69
2	-1.0 - 0.0	390 ± 53	1.089	1534 ± 88
3	0.0 - 0.5	290 ± 39	1.064	2445 ± 57
4	0.5 - 1.0	209 ± 42	1.051	1813 ± 49
5	1.5 - 2.0	150 ± 48	1.085	1315 ± 41

Table B.5: Number of D^* candidates with the statistical error for each η bin of the differential cross section of the 35m sample.

	W range [GeV]	$N^{DATA}(D^*)$	Norm. factor	$N^{MC}(D^*)$
1	200 - 220	522 ± 54	1.080	5097 ± 81
2	220 - 240	559 ± 56	1.050	3533 ± 66
3	240 - 260	250 ± 42	1.104	2089 ± 53

Table B.6: Number of D^* candidates with the statistical error for each W bin of the differential cross section of the 35m sample.

Appendix C

Systematics

In this appendix the systematic errors for both the 44m and 35m taggers are presented as tabulated variables, see Tables C.1- C.6, and as histograms, see Figures C.1- C.6. The CTD systematic is not plotted because it is very small, but the tabulated variables can be found in the Tabs. C.1-C.6.

The yellow band in the plots represents the statistical errors of the central value of the differential cross section, the points are the shifted values and the error on the points is the square root of the difference of the statistical errors of the central and the shifted cross sections. Uncertainties due to ΔM variations are consistent with the background fluctuations.

		W range [GeV]	
		80 – 100	100 – 120
1	Δ M narrow	-0.0180	+0.0027
2	Δ M wide	+0.0099	-0.0033
3	Δ M contr L	+0.0040	-0.0015
4	Δ M contr R	+0.0098	-0.0002
5	CAL E scale incr.	-0.0043	+0.0027
6	CAL E scale decr.	+0.0047	-0.0032
7	44m acc down	-0.0160	-0.0100
8	44m acc up	+0.0160	+0.0100
9	Pythia	-0.0102	-0.0064
10	CTD incr.	+0.0008	+0.0001
11	CTD decr.	-0.0010	-0.0018

Table C.1: Systematics of the 44m tagger in each W bin.

		η range				
		-1 – -0.5	-0.5 – 0	0 – 0.5	0.5 – 1	1 – 1.5
1	Δ M narrow	-0.0170	-0.0970	-0.0410	-0.0820	-0.2200
2	Δ M wide	-0.0250	+0.0000	+0.0650	+0.0180	+0.1600
3	Δ M contr L	-0.0250	+0.0320	+0.0240	-0.0025	-0.0130
4	Δ M contr R	-0.0420	+0.0320	+0.0650	+0.0081	+0.3200
5	CAL E scale incr.	-0.0170	-0.0710	+0.0023	+0.0065	+0.0120
6	CAL E scale decr.	-0.0170	+0.0580	-0.0210	-0.0110	+0.0063
7	44m acc down	-0.0450	-0.1550	-0.2600	-0.2800	-0.2400
8	44m acc up	+0.0450	+0.1550	+0.2600	+0.2800	+0.2400
9	Pythia	-0.0290	-0.0990	-0.1670	-0.1800	-0.1500
10	CTD decr	-0.0032	-0.0210	-0.0670	-0.0310	-0.0098
11	CTD incr	+0.0030	+0.0069	+0.0014	+0.0260	+0.0250

Table C.2: Systematics of the 44m tagger in each η bin.

		W range [GeV]		
		200 - 220	220 - 240	240 - 260
1	ΔM narrow	+0.00075	-0.00420	+0.00330
2	ΔM wide	+0.00240	+0.00210	-0.00140
3	ΔM contr. left	-0.00056	+0.00067	-0.00560
4	ΔM contr. right	+0.00270	-0.00022	+0.00220
5	$E_{e'}$ of 35m tagger decr	-0.00150	-0.00220	-0.00140
6	$E_{e'}$ of 35m tagger inc	+0.00230	+0.00180	+0.00150
7	35m acceptance up	+0.00390	+0.00500	+0.00310
8	35m acceptance down	-0.00390	-0.00500	-0.00310
9	Pythia	-0.00220	-0.00280	-0.00170
10	CTD inc	1.61e-05	+0.00031	+0.00026
11	CTD decr	-0.00015	-0.00063	-0.00015

Table C.3: Systematics of 35m tagger in each W bin.

		η range				
		-1.5 - -1	-1 - -0.5	-0.5 - 0	0 - 0.5	0.5 - 1
1	ΔM narrow	-0.0270	-0.09000	-0.089	+0.134	+0.0470
2	ΔM wide	+0.0990	+0.02600	+0.019	+0.087	-0.0510
3	ΔM contr. left	-0.0320	+0.03900	-0.070	-0.095	-0.0043
4	ΔM contr. right	+0.0550	+0.02400	+0.027	+0.035	+0.0430
5	$E_{e'}$ of 35m tagger decr	-0.0490	-0.04800	-0.042	-0.028	-0.0240
6	$E_{e'}$ of 35m tagger inc	+0.0740	+0.05500	+0.042	+0.035	+0.0280
7	35m acceptance up	+0.1500	+0.12000	+0.090	+0.066	+0.0510
8	35m acceptance down	-0.1500	-0.12000	-0.090	-0.066	-0.0510
9	Pythia	-0.0820	-0.06900	-0.051	-0.037	-0.0290
10	CTD inc	+0.0061	+0.00370	+0.006	+0.005	+0.0033
11	CTD decr	-0.0010	-0.00044	-0.016	-0.010	-0.0120

Table C.4: Systematics of 35m tagger in each η bin.

		p_T range [GeV]									
		1.5 – 2	2 – 2.5	2.5 – 3	3 – 3.5	3.5 – 4	4 – 4.5	4.5 – 5	5 – 5.5	5.5 – 6.5	6.5 – 8
1	Δ M narrow	-0.2600	-0.0100	-0.0290	-0.0360	-0.0180	-0.02000	-0.0019	-0.0074	-0.0045	-0.0052
2	Δ M wide	-0.2900	+0.2900	+0.0219	+0.0200	-0.0045	-0.00820	+0.0019	+0.0000	+0.0027	+0.0013
3	Δ M contr L	-0.0940	+0.0220	+0.0810	+0.0084	-0.0023	+0.0000	+0.0057	+0.0018	-0.0009	+0.0007
4	Δ M contr R	-0.0310	+0.1200	+0.1200	+0.0280	+0.0023	-0.0082	+0.0075	-0.0018	+0.0036	+0.0013
5	CAL E scale incr.	+0.0000	-0.0167	+0.0150	-0.0140	+0.0000	-0.0020	+0.0000	+0.0000	+0.0000	+0.0000
6	CAL E scale decr.	-0.0834	-0.0170	+0.0260	+0.0180	-0.0023	+0.0041	+0.0019	+0.0000	+0.0000	+0.0000
7	44m acc down	-0.4600	-0.2700	-0.1300	-0.0740	-0.0370	-0.0270	-0.013	-0.0083	-0.0043	-0.0014
8	44m acc up	+0.4600	+0.2700	+0.1300	+0.0740	+0.0370	+0.0270	+0.013	+0.0083	+0.0043	+0.0014
9	Pythia	-0.2970	-0.1700	-0.0860	-0.0480	-0.0240	-0.0170	-0.0082	-0.0053	-0.0028	-0.0009
10	CTD decr	-0.0580	-0.0024	-0.0087	-0.0160	-0.0071	-0.0064	-0.0031	-0.0014	-0.0010	-0.0002
11	CTD incr	+0.0370	+0.0053	+0.0077	+0.0054	+0.0010	+0.0008	+0.0003	+0.0007	+0.0002	+0.0001

Table C.5: Systematics of the 44m tagger in each $p_T(D^*)$ bin.

		p_T range [GeV]								
		2 - 2.5	2.5 - 3	3 - 3.5	3.5 - 4	4 - 4.5	4.5 - 5	5 - 5.5	5.5 - 6.5	6.5 - 8
1	ΔM narrow	+0.0870	-0.0160	-0.0250	+0.0074	0.0000	+0.0165	-0.0114	-0.0089	-0.0018
2	ΔM wide	+0.2100	-0.1020	0.0000	+0.0520	+0.0350	-0.0033	0.0000	+0.0020	-0.0009
3	ΔM con. left	-0.1900	-0.0640	+0.0042	+0.0260	+0.0070	-0.0360	-0.0057	-0.0044	+0.0018
4	ΔM con. right	+0.2300	+0.0480	-0.0083	+0.0037	-0.0110	+0.0260	-0.0085	-0.0015	+0.0009
5	$E_{e'}$ of 35m decr	-0.0430	-0.0540	-0.0380	-0.0230	-0.0180	-0.0088	-0.0036	-0.0024	-0.0015
6	$E_{e'}$ of 35m inc	+0.0600	+0.0460	+0.0510	+0.0370	+0.0095	+0.0081	+0.0067	+0.0028	+0.0025
7	35m acc. up	+0.1120	+0.1120	+0.0760	+0.0620	+0.0340	+0.0170	+0.0140	+0.0090	+0.0040
8	35m acc. down	-0.1120	-0.1120	-0.0790	-0.0620	-0.0340	-0.0170	-0.0140	-0.0090	-0.0040
9	Pythia	-0.0630	-0.0630	-0.0440	-0.0350	-0.0190	-0.0095	-0.0081	-0.0050	-0.0022
10	CTD inc	+0.0073	+0.0075	+0.0012	+0.0015	+0.0029	+0.0003	5.28e-05	6.16e-06	+0.0002
11	CTD decr	-0.026	-0.0150	-0.0082	-0.0051	-0.0014	-0.0003	-0.0010	-0.0021	-0.0002

Table C.6: Systematics of 35m tagger in each $p_T(D^*)$ bin.

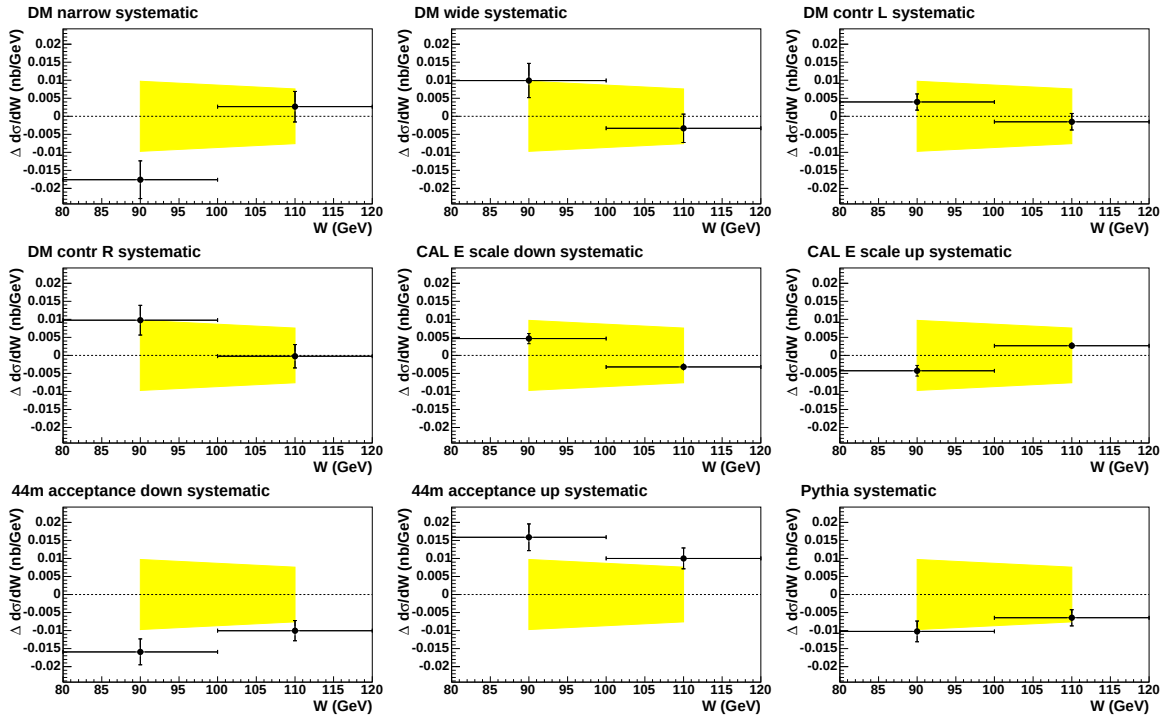

Figure C.1: Systematics of 44m tagger in each W bin separately, the order corresponds to the first nine rows in the Table. C.1

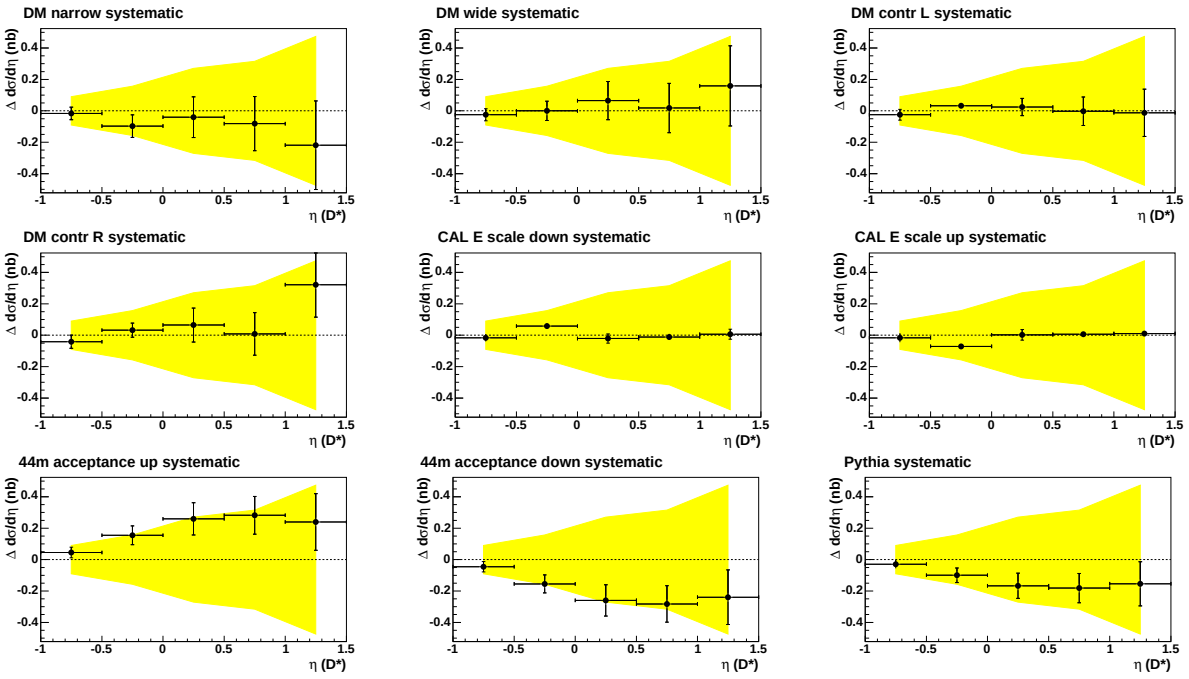

Figure C.2: Systematics of 44m tagger in each $\eta(D^*)$ bin separately, the order corresponds to the first nine rows in the Table. C.2

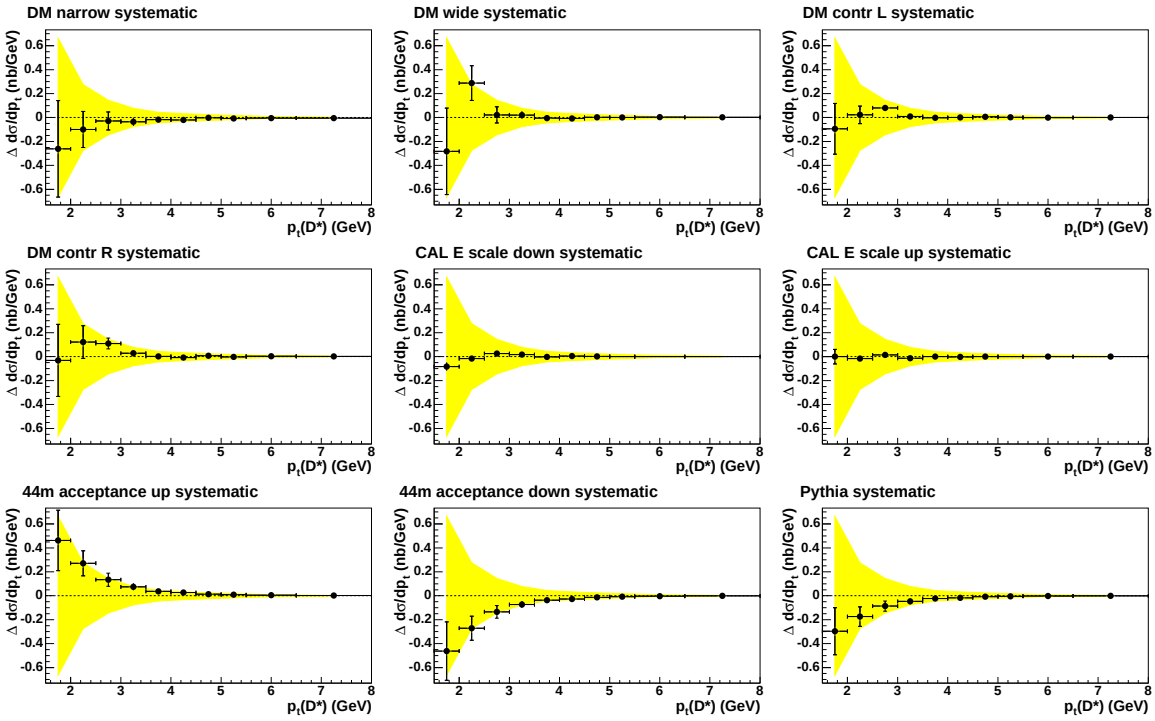

Figure C.3: Systematics of 35m tagger in each $p_T(D^*)$ bin separately, the order corresponds to the first nine rows in the Table C.6

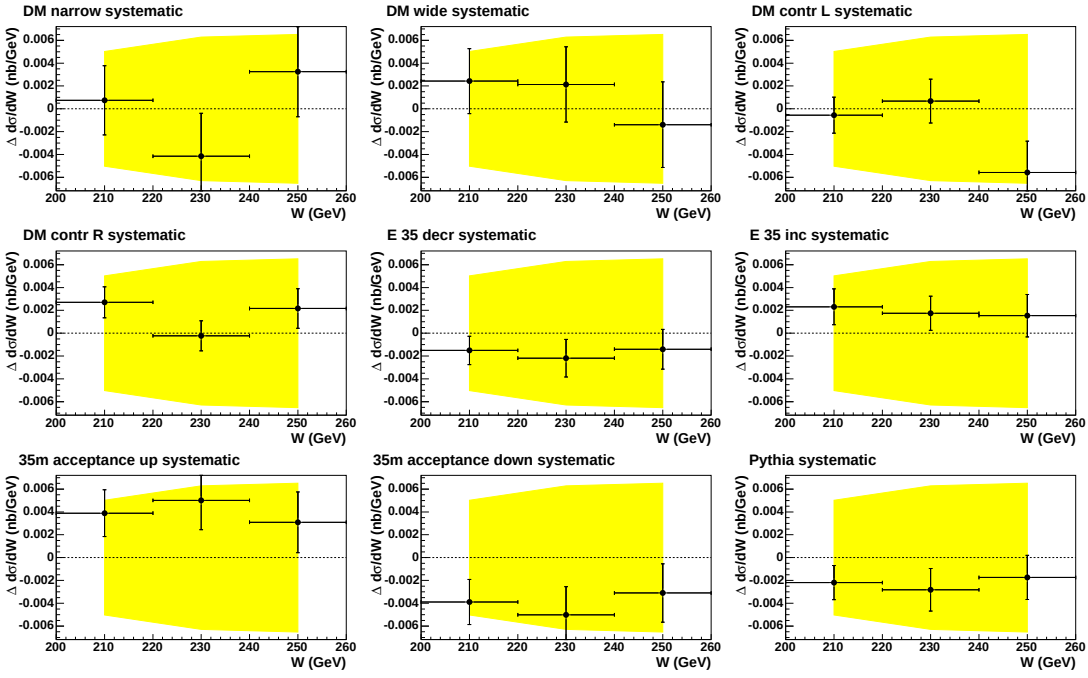

Figure C.4: Systematics of 35m tagger in each W bin separately, the order corresponds to the first nine rows in the Table. C.3

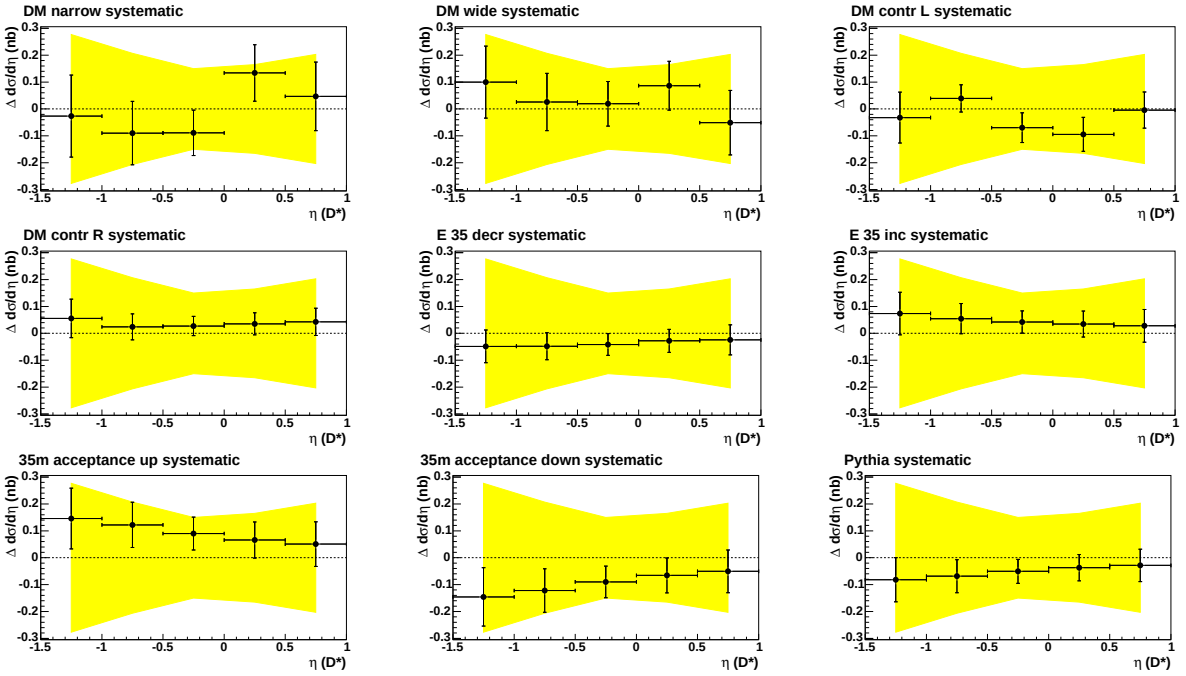

Figure C.5: Systematics of 35m tagger in each $\eta(D^*)$ bin separately, the order corresponds to the first nine rows in the Table. C.4

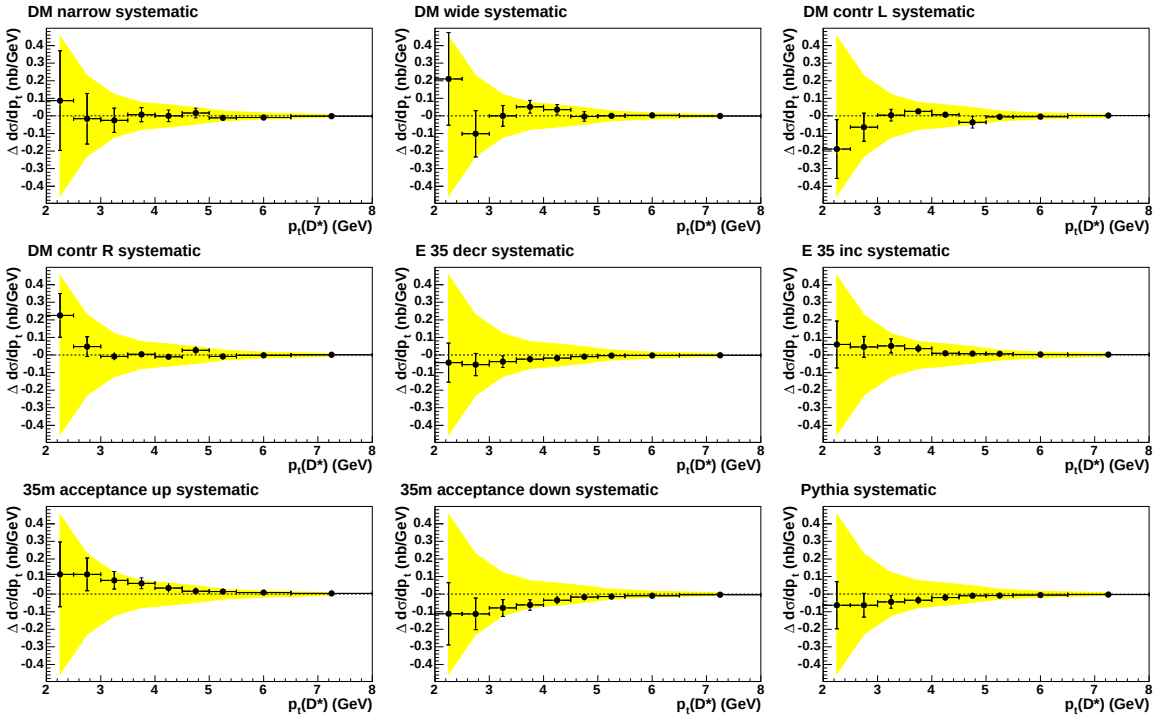

Figure C.6: Systematics of 35m tagger in each $p_T(D^*)$ bin separately, the order corresponds to the first nine rows in the Table C.6

List of Figures

1.1 Schematic diagram of electron-proton scattering. 7
1.2 Kinematic (x, Q^2) region at HERA (H1, ZEUS) compared to fixed target experiment. 9
1.3 The differential NC and CC cross sections measured by ZEUS and H1 collaborations as a function of Q^2 for e^+p and e^-p scatterings. 11
1.4 Leading order direct photoproduction: boson gluon fusion, initial state radiation and QCD Compton scattering. 12
1.5 Leading order resolved photoproduction. 13
1.6 General sketch of a resolved PHP process. 14
1.7 The photoproduction as a direct or as a resolved process depending on the choice of μ. 15
1.8 Total cross section for photoproduction of $c\bar{c}$ pairs as a function of the γp centre-of-mass energy compared to the the next-to-leading order QCD predictions and the other experimental results. 16
1.9 Comparison of massive (FMNR) and massless (PFF) calculations. 18
1.10 Total charm photoproduction cross section as a function of $W_{\gamma p}$. 20
1.11 Differential cross sections $d\sigma/d\eta(D^*)$ for untagged photoproduction. 21

2.1 The HERA colliderand the preselectors Linac, DESY and PETRA. 23
2.2 Integrated luminosity delivered by HERA in years 1992-2000 and integrated luminosity recorded by the ZEUS in the years 1993-2000. 24
2.3 The ZEUS coordinate system. 25
2.4 Longitudinal cross-sectional view of the ZEUS detector along the beam direction. 26
2.5 Transverse cross-sectional view of the ZEUS detector perpendicular to the beam direction. 26
2.6 Layout of a CTD octant. 27
2.7 Layout of a FCAL module. 29
2.8 The luminosity monitor system, 8m and 44m taggers position. 30
2.9 The W range of the tagged photoproduction events at ZEUS. 31
2.10 Horizontal cross-section of the 44m electron calorimeter with position. 31
2.11 Schematic layout of the trigger and readout system of ZEUS. 33

3.1 Schematic view of the processes in a generator. 35
3.2 Hadronisation models: a sketch of the cluster hadronization model as used in HERWIG and a sketch of the string fragmentation model as used in PYTHIA. 37
3.3 Examples of LO diagrams for charm production. 38
3.4 Examples of diagrams involving in NLO correction for direct photon process. . 39
3.5 A schematic diagram of the ZEUS Data and Monte Carlo reconstruction chain. 40

4.1 Schematic view of the reconstruction procedure with ZUFOs. 43

4.2 Hadronic system information, $E - P_z$, extracted using different algorithms for the 44m data sample. . . . 44
4.3 The CTD cells with a track of a charged particle and the calculated positions of the hits. . . . 45
4.4 An overview of the ZEUS HFL triggers for the 8m, 35m and 44m taggers as implemented in the 1998 - 2000 running period. . . . 46
4.5 $Z-$vertex distribution of data with all analysis cuts except z_{vtx} cut. . . . 50
4.6 Acceptance of the electron taggers as a function of the electron energy. . . . 51
4.7 $M(D_0)$ distribution for events with an electron in the 44m and in the 35m taggers. 53
4.8 ΔM distribution for events with an electron in 44m and 35m taggers. . . . 54
4.9 D^* right charge selection and wrong charge distribution for events with an electron in 35m. . . . 56
4.10 The subtracted ΔM distribution for events with an electron in 35m. . . . 56
4.11 Sketch of the tagging system for the photon and electron/positron scattered under small angle. . . . 57
4.12 The bremsstrahlung photon energy distribution in the $LUMI_\gamma$ detector as a function of ADC counts for all events and for events tagged in the 44m tagger together with the tagging efficiency. . . . 58
4.13 The acceptance of the 44m tagger as a function of the hadronic centre-of-mass energy, W. . . . 59
4.14 The efficiency of the 35m tagger for D^* photoproduction. . . . 60

5.1 44m DATA - MC comparison of variables related to the D^* reconstruction for D^* candidates. . . . 63
5.2 35m DATA - MC comparison of variables related to the D^* reconstruction for D^* candidates. . . . 64
5.3 Scattered plot of the reconstructed vs. the true kinematic MC variables: $P_T(D^*)$, $\eta(D^*)$ and W for the 44m sample. . . . 65
5.4 Scattered plot of the reconstructed vs. the true kinematic MC variables: $P_T(D^*)$, $\eta(D^*)$ and W for the 35m sample. . . . 65
5.5 Distributions of the differences of the reconstructed and true MC kinematic variables: $P_{T,REC}(D^*) - P_{T,TRUE}(D^*)$, $\eta_{REC}(D^*) - \eta_{TRUE}(D^*)$ and $W_{REC}(D^*) - W_{TRUE}(D^*)$ for the the 44m sample. . . . 66
5.6 Distributions of the differences of the reconstructed and true MC kinematic variables: $P_{T,REC}(D^*) - P_{T,TRUE}(D^*)$, $\eta_{REC}(D^*) - \eta_{TRUE}(D^*)$ and $W_{REC}(D^*) - W_{TRUE}(D^*)$ for the the 35m sample. . . . 67
5.7 ΔM distributions for each bin in $p_T(D^*)$ for the 44m sample. . . . 69
5.8 ΔM distributions for each bin in $p_T(D^*)$ for the of 35m sample. . . . 70
5.9 ΔM distributions for each bin in $\eta(D^*)$ cross section for the 44m sample. . . . 71
5.10 ΔM distributions for each bin in $\eta(D^*)$ cross section for the 35m sample. . . . 72
5.11 ΔM distributions for each bin in W cross section for the 44m sample. . . . 73
5.12 ΔM distributions for each bin in W cross section for the 35m sample. . . . 73
5.13 Acceptance in each bin of cross section for the 44m sample as a function of $p_T(D^*)$, $\eta(D^*)$ and W. . . . 74
5.14 Acceptance in each bin of cross section for the 35m sample as a function of $p_T(D^*)$, $\eta(D^*)$ and W. . . . 74
5.15 Differential cross sections analysis using the 44m tagger as a function of $p_T(D^*)$, $\eta(D^*)$ and W. . . . 76
5.16 Differential cross sections analysis using the 35m tagger as a function of $p_T(D^*)$, $\eta(D^*)$ and W. . . . 77

5.17 The two-photon production in e^+e^- collisions and photoproduction in HERA. . 79

6.1 Measured cross sections in bins of $p_T(D^*)$, $\eta(D^*)$ and W compared with the LO HERWIG MC prediction for the 44m analysis. 86
6.2 Measured cross sections in bins of $p_T(D^*)$, $\eta(D^*)$ and W compared with the LO HERWIG MC prediction for the 35m analysis. 86
6.3 Measured differential cross section in bins of W, $\eta(D^*)$ and $p_T(D^*)$ compared with the FMNR NLO QCD predictions for the 44m tagger analysis. 88
6.4 Measured differential cross section in bins of W, $\eta(D^*)$ and $p_T(D^*)$ compared with the FMNR NLO QCD predictions for the 35m tagger analysis. 89
6.5 Differential cross sections $d\sigma/dp_T(D^*)$ and $d\sigma/d\eta(D^*)$ for $-1.0 < \eta(D^*) < 1.5,\ 2.0 < p_T(D^*) < 8$ GeV, $80 < W < 120$ GeV, $Q^2 < 0.015$ GeV^2. 90
6.6 Differential cross sections $d\sigma/d\eta(D^*)$ for untagged photoproduction. 91
6.7 Differential D^*-photoproduction cross sections $d\sigma/dp_T$, $d\sigma/d\eta(D^*)$ and $d\sigma/W$ in the kinematic range $Q^2 < 0.01\,\text{GeV}^2$, $171 < W < 256\,\text{GeV}$, $p_T(D^*) > 2.5\,\text{GeV}$ and $|\eta(D^*)| < 1.5$. 92
6.8 Differential cross section $d\sigma/dW$ as a function of W of 35m tagger comparing to the H1 cross sections. 93
6.9 Diffrential cross sections $d\sigma/d\eta$ as a function of $\eta(D^*)$ for different W kinematic region. 94
6.10 Diffrential cross sections $d\sigma/dW$ as a function of W for both the 44m and the 35m taggers. 95
6.11 Total charm photoproduction cross-sections as a function of $W_{\gamma p}$ with the 44m and the 35m results. 96

A.1 ΔM distributions for each bin of W cross section of 44m Monte Carlo sample. 99
A.2 ΔM distributions for each bin of W cross section of 35m Monte Carlo sample. 100
A.3 ΔM distributions for each bin of $p_T(D^*)$ for the 44m Monte Carlo sample. . . 101
A.4 ΔM distributions for each bin of $p_T(D^*)$ for the of 35m Monte Carlo sample. . 102
A.5 ΔM distributions for each bin of $\eta(D^*)$ cross section of 44m Monte Carlo sample. 103
A.6 ΔM distributions for each bin of $\eta(D^*)$ cross section of 35m Monte Carlo sample. 104

C.1 Systematics of 44m tagger in each W bin. 110
C.2 Systematics of 44m tagger in each $\eta(D^*)$ bin. 110
C.3 Systematics of 35m tagger in each $p_T(D^*)$ bin. 111
C.4 Systematics of 35m tagger in each W bin. 111
C.5 Systematics of 35m tagger in each $\eta(D^*)$ bin. 112
C.6 Systematics of 35m tagger in each $p_T(D^*)$ bin. 112

References

[1] M. S. Atiya et al. CIF Coll.., Phys. Rev. Lett. **43**, 414 (1979);
A. R. Clark et al. BFP Coll.., Phys. Rev. Lett. **45**, 682 (1980);
K. Abe et al. SLAC HFP Coll., Phys. Rev. **D 30**, 1 (1984);
M. Arneodo et al. EMC Coll., Z. Pfys. **C 35**, 1 (1987);
M. Aubert et al. EMC Coll., Nucl. Phys. **B 213**, 31 (1983). Phys. Lett. B 167, 127 (1986);
M. Adamovich et al. PEC Coll., Nucl. Phys. **B 187**, 437 (1987);
J. C. Anjos et al. E691 Coll., Phis. Rev. Lett. **65**, 2503 (1990);
D. Aston et al. WA4 Coll., Phis. Lett. **B 94**, 113 (1980).

[2] ZEUS Coll., M. Derrick et al., Phys. Lett. **B 349**, 225 (1995).

[3] H1 Coll., S. Aid et al., Preprint DESY-96-055, DESY, 1996, available on `http://hep-ex/9604005`.

[4] D. Griffiths, *Introduction to elementary particles*. John Wiley & Sons, Inc., 1987.

[5] Donald H. Perkins, *Introduction to High Energy Physics*. Cambridge U. Press, 1972.

[6] F. Halzen and A.D. Martin, *Quarks and Leptons: An Introductory Course in Modern Particle Physics*. John Wiley & Sons, Inc, 1984.

[7] M. Gell-Mann, Phys. Lett. **8**, 214 (1964).

[8] G. Zweig (1964). CERN-8192/TH 401, CERN-8419/TH 402, 1964.

[9] G. Zweig, *An SU(3) model for strong interaction symmetry and its breaking*. CERN-TH-412, p 74, 1964.

[10] J.D. Bjorken, Phys. Rev. **179**, 1547 (1969).

[11] Available on `http://www-zeus.desy.de/physics/sfew/PUBLIC/sfew_results/preliminary/eps03/zeush1.php`.

[12] Robert Devenish and Amanda Cooper-Sarkar, *Deep Inelastic Scattering*. Oxford University Press, New York, USA, 2004.

[13] ZEUS and H1 Coll., Gabareen Mokhtar, Arafat et al., Preprint hep-ex/0406036, 2004, available on `http://www-zeus.desy.de/physics/sfew/PUBLIC/sfew_results/preliminary/eps03/zeush1.php`.

[14] G. Ridolfi, Nucl. Phys. **25**, 1313 (1999).

[15] R.K. Ellis, W.J. Stirling and B.R. Webber, *QCD and Collider Physics*, Cambridge Monographs on Particle Physics, Nuclear Physics and Cosmology, Vol. 8. Cambridge University Press, 1996.

[16] G. Bellini, *La Thuile 1994, Results and perspectives in particle physics*, M. Greco (ed.), pp. 435–466. Editions Frontieres, Gif-sur-Yvette, France (1994).

[17] Tagged Photon Spectrometer Coll., J.C. Anjos et al., Phys. Rev. Lett. **62**, 513 (1989).

[18] NA14/2 Coll., M.P. Alvarez et al., Z. Phys. **C 60**, 53 (1993).

[19] H1 Coll., S. Aid et al., Nucl. Phys. **B 472**, 32 (1996).

[20] A.D. Martin, R.G. Roberts and W.J. Stirling, Phys. Lett. **B 354**, 155 (1995).

[21] M. Glück, E. Reya and A. Vogt, Phys. Rev. **D 45**, 3986 (1992).

[22] H. Abramowicz, K. Charchula and A. Levy, Phys. Lett. **B 269**, 458 (1991).

[23] M. Glück, E Reya and A. Vogt, Phys. Rev. **D 46**, 1973 (1992).

[24] S. Frixione et al., Nucl. Phys. **b412**, 225 (1994).

[25] S. Frixione, P. Nason, G. Ridolfi, Preprint hep-ph/9506226, 1995.

[26] M. Cacciari and M. Greco, Phys. Rev. **D 55**, 7134 (1997).

[27] M. Cacciari et al., Phys. Rev. **D 55**, 2736 (1997).

[28] J. Bennewies, B. A. Kniehl and G. Kramer, Z. Phys. **C 76**, 677 (1997).

[29] M. L. Mangano, P. Nason and G. Ridolfi, Nucl. Phys. **B 373**, 295 (1993).

[30] M. L. Mangano, P. Nason and G. Ridolfi, Nucl. Phys. **B 405**, 507 (1993).

[31] M. Cacciari and M. Greco, Z. Phys. **C 69**, 459 (1993).

[32] M. Cacciari, Preprint hep-ph/9708282, 1997. To appear in proceedings of the Ringberg Workshop "New Trends in HERA Physics".

[33] S. Stonjek, *Measurement of $D^{*\pm}$ Cross Sections in Photon Proton Collisions at HERA*. Ph.D. Thesis, Hamburg University, Hamburg, Germany, Report DESY-THESIS-2001-043, DESY, 2001.

[34] J. Breitweg et al. ZEUS Coll.. (1999). Also in preprint DESY-98-085, DESY. Contribution to the 7th international workshop on deep inelastic scattering and QCD, Zeuten, Germany.

[35] *web address*, available on `http://www-zeus.desy.de/physics/lumi/lumi00/day.html`.

[36] ZEUS Coll., U. Holm (ed.), *The ZEUS Detector*. Status Report (unpublished), DESY (1993), available on `http://www-zeus.desy.de/bluebook/bluebook.html`.

[37] ZEUS Coll., *A Microvertex Detector for ZEUS* (unpublished), 1997, available on `http://www-zeus.desy.de/ZEUS_ONLY/zeus_notes/ZEUS_NOTES/ZEUS-97-006.ps`. ZEUS-97-006, DESY-PRC 97/01.

[38] N. Harnew et al., Nucl. Inst. Meth. **A 279**, 290 (1989);
B. Foster et al., Nucl. Phys. Proc. Suppl. **B 32**, 181 (1993);
B. Foster et al., Nucl. Inst. Meth. **A 338**, 254 (1994).

[39] R. Hall-Wilton et al., *The CTD Tracking Resolution* (unpublished). ZEUS-99-024, internal ZEUS-note, 1999.

[40] M. Derrick et al., Nucl. Inst. Meth. **A 309**, 77 (1991);
A. Andresen et al., Nucl. Inst. Meth. **A 309**, 101 (1991);
A. Caldwell et al., Nucl. Inst. Meth. **A 321**, 356 (1992);
A. Bernstein et al., Nucl. Inst. Meth. **A 336**, 23 (1993).

[41] K. Piotrzkowski, *Diffractive Photoproduction of Vector Mesons at High* $|t|$ (unpublished). ZEUS-97-016, internal ZEUS-note, 1997.

[42] J. Andruszków et al., Acta Phys. Pol. **B 32**, 2025 (2001).

[43] *web address*, available on
`http://www-zeus.desy.de/components/offline/offline.html`.

[44] J.C. Collins, D.E. Soper and G. Sterman, Preprint hep-ph/0409313, 2004.

[45] H. Plotow-Besh, Int. J. Mod. Phys. **A 10**, 2901 (1995).

[46] N. Brook et al., *Proc.of Workshop on Physics at HERA, Hamburg, Germany, October 29-30.* (1991).

[47] G. Corcella et al., Preprint hep-ph/0011363, 2000.

[48] V.M. Budnev et al., Phys. Rep. **15C**, 181 (1974).

[49] T. Sjöstrand et al., Comp. Phys. Comm. **135**, 238 (2001);
T. Sjöstrand, L. Lönnbad, S Mrenna, P. Skands, Preprint hep-ph/0308153, 2003.

[50] C.F. von Weizsäcker, Z. Phys. **88**, 612 (1934). In German.

[51] E.J. Williams, Phys. Rev. **45**, 729 (1934).

[52] T. Sjöstrand, Comp. Phys. Comm. **39**, 347 (1986).

[53] M. Mangano, P. Nason, G. Ridolfi, Nucl. Phys. **B 373**, 295 (1992).

[54] C. Peterson et al., Phys. Rev. **D 27**, 105 (1983).

[55] T. Haas, *Generating Monte Carlo Events with MOZART* (unpublished). ZEUS-92-021, 1992;
Available on `http://www-zeus.desy.de/bluebook/ch17/section2_4_6.html`.

[56] R. Brun et al., GEANT3, Technical Report CERN-DD/EE/84-1, CERN, 1987;
CERN application Software Group (S. Giani et al.), *GEANT: Detector description and simulation tool* (unpublished). CERN Program Library Long Writeup W5013, 1994.

[57] Els de Wolf (editor) et al., *ZGANA, ZEUS trigger simulation library*, available on
`http://www-zeus.desy.de/components/offline/offline.html`.

[58] S.M. Fisher and P. Palazzi, *ADAMO Programmers Manual – Version 3.2.* CERN ECP and RAL, available on
`http://adamo.web.cern.ch/Adamo/programmers_manual/TOC_of_adamo.html`.

[59] S. Dusini, A. Fox-Murphy, I. Grabowska-Bold, C. Gwenlan, J. Sztuk et al. ZEUS Coll., *ORANGE USER MANUAL*, available on `http://www-zeus.desy.de/ZEUS_ONLY/analysis/orange/index.html`.

[60] F. Jacquet and A. Blondel, *Proc. Study of an ep Facility in Europe.* DESY 79-48 (1979).

[61] G.M. Briskin, *Diffractive Dissociation in ep Deep Inelastic Scattering.* Ph.D. Thesis, Tel Aviv University, 1998. (Unpublished).

[62] N. Tuning, *ZUFOs: Hadronic Final State Reconstruction with Calorimeter, Tracking and Backsplash Correction* (unpublished). ZEUS-Note-01-021, 2001.

[63] G.F. Hartner, *VCTRAK(3.07/04): Offline Output Information* (unpublished). ZEUS-97-064, internal ZEUS-note, 1997.

[64] G. F. Hartner, *VCTRAK Briefing: Program and Math* (unpublished). ZEUS-98-058, internal ZEUS-note, 1998.

[65] Particle Data Group, S. Eidelman et al., Phys. Lett. **D 592**, 1 (2004).

[66] L. Gladilin, Preprint hep-ex/9912064, 1999.

[67] C. Coldewey, L.K. Gladilin, R. Graciani, Y. Eisenberg, D. Hochman, U. Karshon, I.A. Korzhavina, *Study of D^* Photoproduction in ep Collisions at HERA* (unpublished). ZEUS-96-124, 1996.

[68] L. Adamczyk et al, *Luminosity Measurement in the ZEUS Experiment* (unpublished). ZEUS-01-004, internal ZEUS note, 2001.

[69] K.H. Klimek, *Cross Section Measurement of Vector Meson Quasi-Photoproduction at High Four-Momentum Transfer Using the ZEUS Detector at the HERA Collider.* Ph.D. Thesis, Institute of Nuclear Physics, Cracow, Poland, Report DESY-THESIS-2001-053, DESY, 2001.

[70] K. Piotrzkowski, L. Suszycki, *BREMGE Monte Carlo Generator of High Energy Electron-Proton and Electron-Nucleus Bremsstrahlung Events* (unpublished). ZEUS-92-034, Proceedings of the Workshop on Physics at HERA, 1992.

[71] ZEUS Coll., *Measurement of Inclusive $D_s^{\pm}$ and $D^{*\pm}$ Cross Sections in Photoproduction at HERA.* Contributed paper 115 to EPS99, Tampere, Finland, 1999.

[72] ZEUS Coll., S. Chekanov et al., Preprint DESY-03-093 (hep-ex/0307043), 2003. Subm. to Eur. Phys. J. C;
ZEUS Coll., S. Chekanov et al., Phys. Lett. **B 539**, 197 (2002);
ZEUS Coll., Preprint DESY-03-214, DESY, 2003. Subm. to Phys. Rev. D.

[73] P. Nason, C. Oleari, Nucl. Phys. **565**, 245 (2000).

[74] ZEUS Coll., S. Chekanov et al., Eur. Phys. J. **C 44**, 351 (2005).

[75] CTEQ Coll., H.L. Lai et al., Eur. Phys. J. **C 12**, 375 (2000).

[76] P. Aurenche, J.P. Guillet and M. Fontannaz, Z. Phys. **C 64**, 621 (1994).

[77] ZEUS Coll., S. Chekanov et al., Nucl. Phys. **B 729**, 492 (2005).

[78] ZEUS Coll., J. Breitweg et al., Eur. Phys. J. **C 6**, 67 (1999).

[79] ZEUS Coll., *Measurement of D^* Photoproduction at HERA*. Abstract 786, Paper contribution to XXXth Int Conference on High Energy Physics ICHEP2002, Amsterdam, The Netherlands, 2002.

[80] H1 Coll., *Photoproduction of D^* Mesons at HERA*. Abstract 5-0162, Paper contribution to 32nd International Conference on High Energy Physics ICHEP2004, Beijing, China, 2004, available on `http://www-h1.desy.de/h1/www/publications/conf/conflist.html`.

[81] G. Flucke, *Photoproduction of D^* Mesons and D^* Mesons Associated with Jets at HERA*. Ph.D. Thesis, Hamburg University, Hamburg, Germany, Report DESY-THESIS-2005-06, 2005.